School of
Chemical Engineering & Advanced Materials
at Newcastle University

Development of non-noble catalysts for hydrogen and oxygen evolution in alkaline polymer electrolyte membrane electrolysis

a thesis submitted by

Luke Watkins

for the
degree of
Doctor of Philosophy, Ph.D.

September 2013

Abstract

Hydrogen is seen as the 'energy carrier of the future' due to the element's relative abundance, the formation of water as opposed to the green house gases when utilised as a fuel in fuel cells, and the ability to be produced by electrolysers powered from renewable energy sources such as wind, water and sunlight. The development of hydrogen production through electrolysis is hindered by the high costs associated with the technology, specifically the ion exchange membranes and electrocatalysts that are employed in the membrane electrode assemblies used in polymer electrolyte electrolysers.

This research focused on the development of non-noble catalysts suitable for hydrogen and oxygen evolution in alkaline electrolysis. Synthesis of NiO was achieved through thermal decomposition, chemical bath deposition and solution growth techniques. A mixed metal oxide, $NiCo_2O_4$, was synthesized through thermal decomposition of metal nitrate salts. Cyclic voltammetry and steady state electrochemical experiments on the electrodes were conducted in an electrochemical half cell electrolyser. A thin film of pure NiO was formed onto a titanium substrate through chemical bath deposition followed by thermal decomposition. The performance of the electrode at 1.73 V, relative to the mass of the catalyst loading, produced 0.25 A cm^{-2} mg^{-1} in 1 M NaOH at 25°C (IrO_2 produced 0.44 A cm^{-2} mg^{-1} in the same electrolyser). The electrode's performance is attributed to the nanoporous structure of the catalyst film (20 – 200 nm pore diameters), which was formed from the chemical bath deposition method used to prepare the catalyst films. Unfortunately this procedure has a limited film thicknesses so higher loadings could not be achieved.

Higher loadings of other non-noble electrocatalysts were made possible with addition of a PVDF binder to the catalyst film. Physical analysis through XRD was performed on the most promising catalysts for the oxygen evolution reaction to confirm their composition. A blend of α-$Ni(OH)_2$ and $4Ni(OH)_2$•NiOOH•xH_2O formed through the chemical bath deposition technique produced higher current densities (104 mA cm^{-2} at 0.8 V vs. Hg/HgO) than another non-noble metal catalyst, $NiCo_2O_4$ (97 mA cm^{-2})

in 1 M NaOH at 25°C. An alkaline polymer electrolyser free from noble metals was developed with a membrane electrode assembly that utilised a partially fluorinated membrane, a PVBC/PVC ionomer in the catalyst layers, 1.0 mg $NiMoO_4$ cm^{-2} in the cathode and 0.7 mg $NiCo_2O_4$ cm^{-2} in the anode. It produced 0.4 A cm^{-2} in 1 M KOH at 25° at a potential of 1.9 V.

Acknowledgements

A big thank you to Keith Scott who allowed me the opportunity to undertake this project, where I had the pleasure of meeting and working with so many people whom I also owe many thanks for their invaluable support.

In my lab environment I've been lucky enough to work with Moodie, Aris and Asier amongst many others. Another big part of my research was based in the environment of C500. A tremendous amount of advice, encouragement, food and drink have been exchanged in this arena intermittently between all the fantastic arguing about culture, politics, football and religion.

Thanks to the lads in the workshop for all the sweets and in particular Jimmy for his help and patience with polymer electrolyser cell fabrication and modifications. My work would also not have been possible without Will and John and their extraordinary glass blowing talent and formation of the glass half cell electrolyser. Thanks also goes to Maggie for her tremendous XRD support and advice.

Thanks to the hoard of other representatives across the university who allowed me to work for them so I could acquire much needed funds for a more sustainable life. Also thanks to my parents for their invaluable support and patience throughout my tenure.

Special mention goes to Newcastle University Water Polo Club, who provided some much needed top end support and motivation at the penultimate stages of my project.

Finally, thank you to Freudenberg FCCT for providing me with gas diffusion layer materials and the University of Surrey's research group led by John Varcoe for their anion exchange membranes.

Contents

List of figures

List of tables

Nomenclature

AAEM	alkaline anion exchange membrane
CBD	chemical bath deposition
CV	cyclic voltammetry
DI Water	deionised water
EIS	Electrochemical impendence spectroscopy
FWHM	full width at half maximum
GDL	gas diffusion layer
HER	hydrogen evolution reaction
IPCC	intergovernmental panel on climate change
MEA	membrane electrode assembly
NiCo2O4 (280)	$NiCo_2O_4$ catalyst synthesised with a final calcination temperature of 280°C
NiCo2O4 (300)	$NiCo_2O_4$ catalyst synthesised with a final calcination temperature of 300°C
NiO (400)	NiO produced through thermal decomposition of nickel nitrate at 400°C
NiO (450)	NiO produced through thermal decomposition of nickel nitrate at 450°C
NiO (CBD)	NiO nanopowder synthesised from chemical bath deposition particulates
NiO (CBD film)	NiO catalyst film deposited onto the electrodes in the chemical bath
NiO (commercial)	NiO nanoparticles supplied from Sigma Aldrich
NiO (urea)	NiO synthesized through co-precipitation with urea
α-Ni(OH)2 / 4Ni(OH)2•NiOOH•xH2O	nickel hydroxides synthesized through chemical bath deposition without thermal treatment
NMP	n-methyl-2-pyrrolidone
OER	oxygen evolution reaction
PEM	polymer electrolyte membrane
PVBC	polyvinylbenzyl chloride
PVC	polyvinyl chloride
PVDF	polyvinylidene difluoride
rpm	revolutions per minute
THF	Tetrahydrofuran
XRD	x-ray diffraction

Index of Symbols

Symbol	Meaning	Usual Units
j_{pa}	anodic peak current	A cm^{-2}
E_{pa}	anodic peak potential	V
j_{pc}	cathodic peak current	A cm^{-2}
E_{pc}	cathodic peak potential	V
ΔE	difference in peak potentials	V
j	current density	A cm^{-2}
E_0	equilibrium potential	V
E_{O_2}	onset potential for oxygen evolution	V
i_0	exchange current	A
j_0	exchange current density	A cm^{-2}
B	full width at half-height of peaks (XRD)	2θ (degrees)
Z''	imaginary impedance	Ω
m%	molar percent	
η	overpotential	V
η_a	overpotential at the anode	V
η_c	overpotential at the cathode	V
υ	scan rate	V s^{-1}
$E^{\circ}_{O_2/H_2O}$	standard potential for O_2 evolution	V
Z'	real impedance	Ω
A	surface area	cm^{-2}
T	temperature	°C
D	average particle size (XRD)	nm
M	molar concentration	mol l^{-1}
$[Ox]$	concentration of oxidised species	
$[Red]$	concentration of reduced species	

1 Introduction and literature review

1.1 A global energy crisis

Assuming that no new government policies are adopted, the International Energy Agency predicts that the world primary energy demand will increase by approximately one third from 2012 to 2035, with China and India accounting for 50% of the growth [1]. The cause of this can be attributed to a number of factors including an unsustainable overpopulation coupled with inefficient energy production and use.

Worryingly, at the beginning of the 21st century, fossil fuels, which include coal, natural gas and oil, provided more than 85% of the total energy used around the world. Figure 1-1 shows the sources of energy in the UK in 2011, with fossil fuels remaining the dominant fuel.

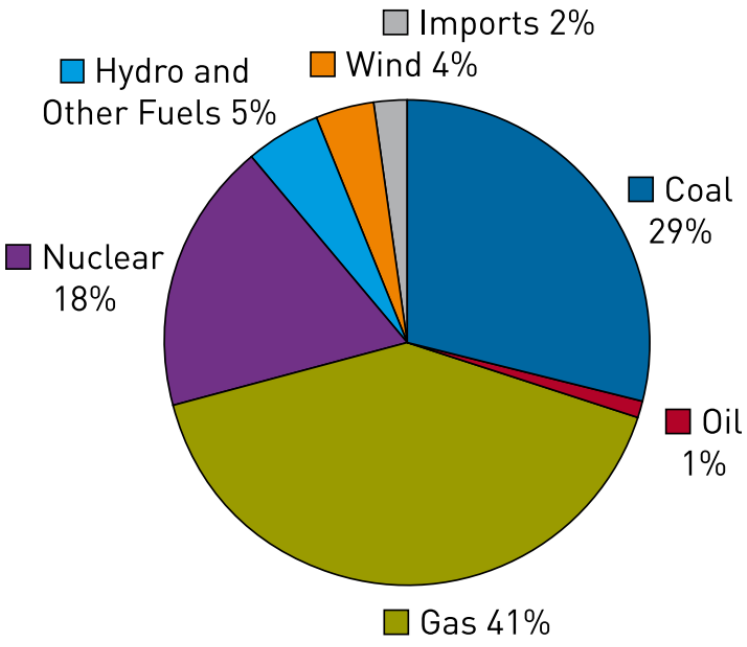

Figure 1-1 Share of total primary energy supply in the UK in 2011 from the Department of Energy & Climate Change [2]

Figure 1-2 shows that, according to the Energy Information Administration, the world marketed energy use of fossil fuels is a trend that is set to continue well into the future.

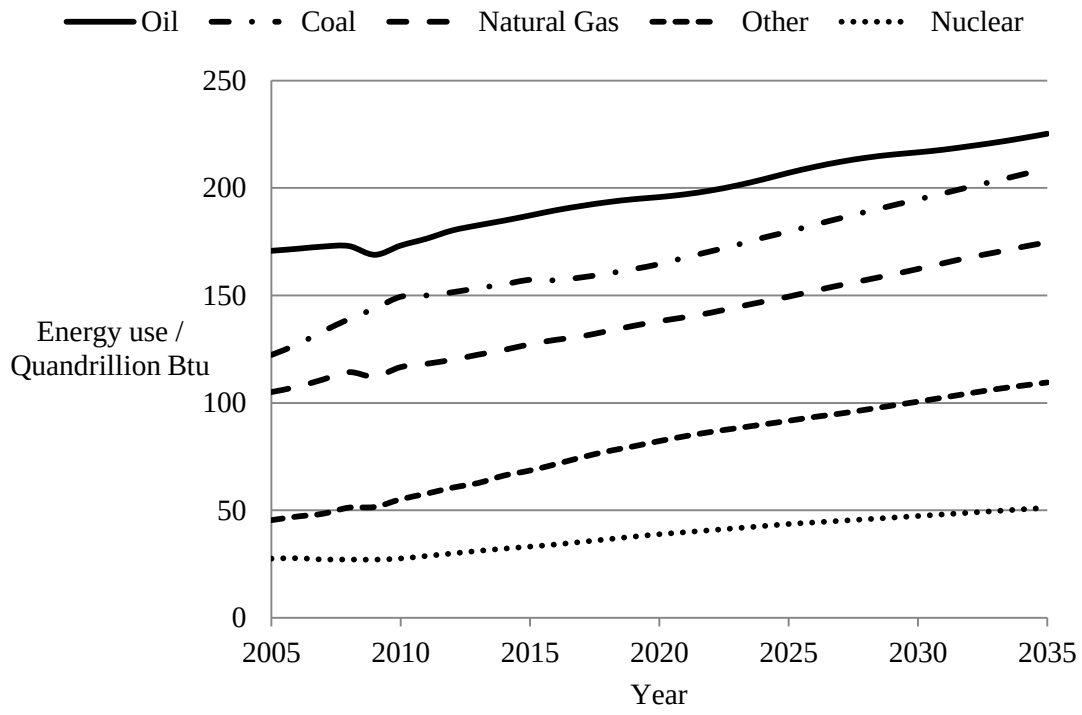

Figure 1-2 Total World Energy Consumption by Fuel Type, 2005-2035 [3]

The rapid increase of fossil fuel use can be partly attributed to recently industrialised countries such and India and China. Their demand for energy is expected to increase even further. Fossil fuels are sourced predominantly from oil, whose market is subject to large and unpredictable fluctuations in price, which in turn manipulate other energy prices and subsequently the world's economy as a whole. The Organization of the Petroleum Exporting Countries (OPEC) is an intergovernmental organization dedicated to stability and shared control of oil. Fossil fuels, especially crude oil, show uneven distribution across the world as depicted in Figure 1-3.

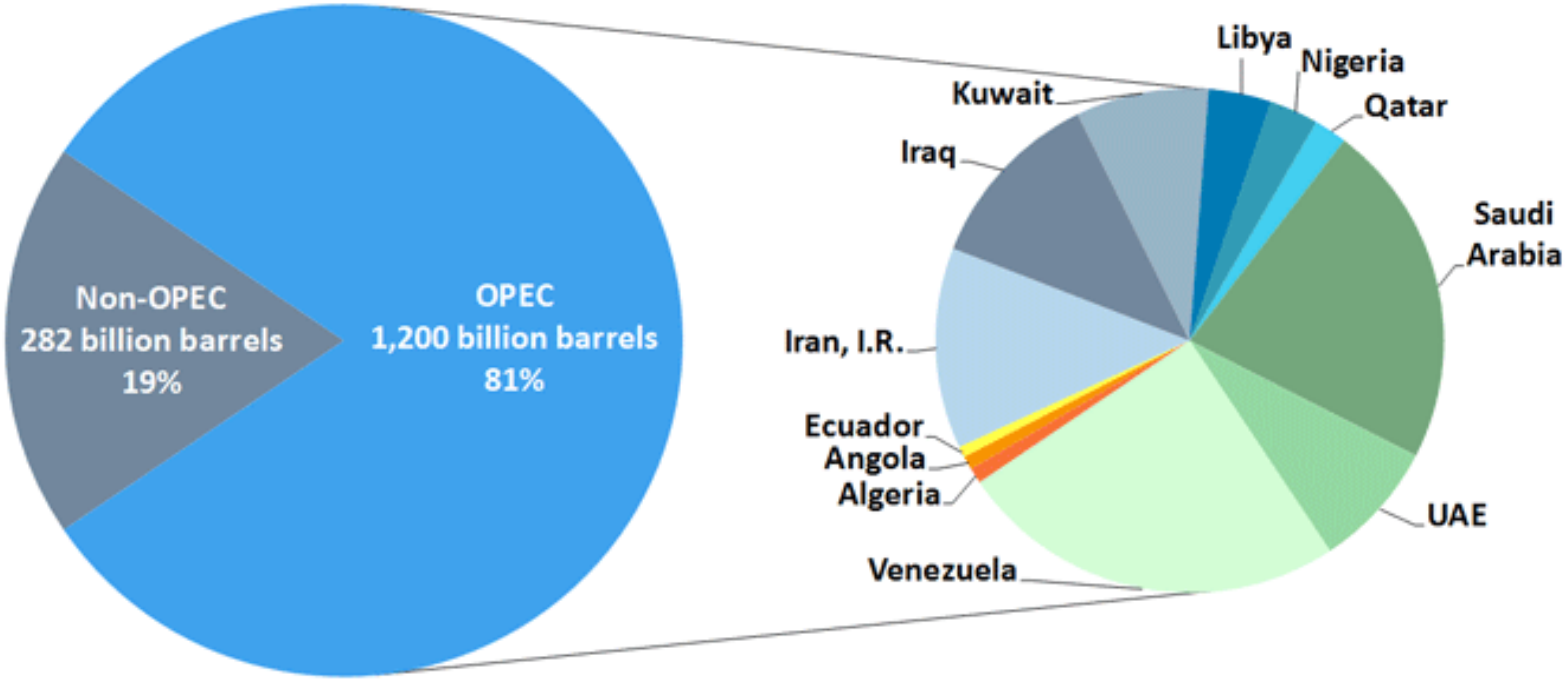

OPEC proven crude oil reserves, end 2011
(billion barrels, OPEC Share)

Venezuela	297.6	24.8%	Iraq	141.4	11.8%	Libya	48.0	4.0%	Algeria	12.2	1.0%
Saudi Arabia	265.4	22.1%	Kuwait	101.5	8.5%	Nigeria	37.2	3.1%	Angola	10.5	0.9%
Iran, I.R.	154.6	12.9%	United Arab Emirates	97.8	8.2%	Qatar	25.4	2.1%	Ecuador	8.2	0.7%

Figure 1-3 OPEC Share of the World Crude Oil Reserves 2011 [4]

Along with the industrial sector, the transportation sector is heavily responsible for air pollution and many alternative fuels are being researched and tested for future use in vehicles. These fuels include ethanol, propane, natural gas and biodiesel. Pollution arising from these sources, caused from combustion, has increasingly caused global environmental issues and escalated fears for human health.

In 2007 the UN's Intergovernmental Panel on Climate Change (IPCC) report [5] declared that the increase of atmospheric greenhouse gas concentrations (including carbon dioxide, nitrous oxide and methane) has caused a global temperature increase of 0.56 to 0.92°C over the last 100 years. This has resulted in a sea level rise of approximately 17 cm due to the melting of ice and thermal expansion of sea water. The report speaks with high confidence that the global warming effect has been caused by humans dramatically increasing the atmospheric concentrations of greenhouse gasses through use of fossil fuels. Furthermore, the IPPC report predicts that before the end of the 21st century, worldwide temperatures will increase another 1.1 to 6.4°C and the sea level will rise with another 18 to 59 cm (with respect to 1990).

This, along with the unstable fossil fuel market and an increasing awareness of the possible anthropogenic effects on climate change, has increased the political drive to reduce greenhouse gas emissions and stimulate the growth of clean technologies for a more sustainable future. A sustainable future requires nations to be independent from trans-boundary supplies as relying on imports of oil is becoming more unpredictable. Localised power sourced from renewable energy technologies will help to improve the security of a nation's supply of energy.

In 1997, the Kyoto Protocol was initiated and obligated its signatories to reduce their emissions by 5% (with respect to 1990) by 2012. Furthermore in March 2007, the EU Transport Policy committed its members to targeting a 20% substitution of fossil fuels with alternative fuels by 2020 [6]. In order for these targets to be reached, clean and renewable technologies, including solar, hydro and wind power, must be pursued. For instance, solar radiation is an ideal source of energy since it is the

earth's primary input of energy and it is available in such a large quantity. From Figure 1-2 it can be calculated that the world's energy consumption in 2012 was approximately 5.7×10^{20} J. More than 5.5×10^{24} J of energy reaches our planet from the Sun every year [7] so the amount of solar energy reaching the earth in just one hour is in the same order as the total world energy consumption in one year.

1.2 Hydrogen energy

The primary uses of hydrogen include oil refining and ammonia production; however, it can also be used to store intermittent renewable energy sources such as solar and wind energy and therefore it is often referred to as the 'energy carrier of the future'. Hydrogen appears to be the most promising source of alternative fuel as it has a higher amount of energy per unit weight than any hydrocarbon fuel as shown in Figure 1-4.

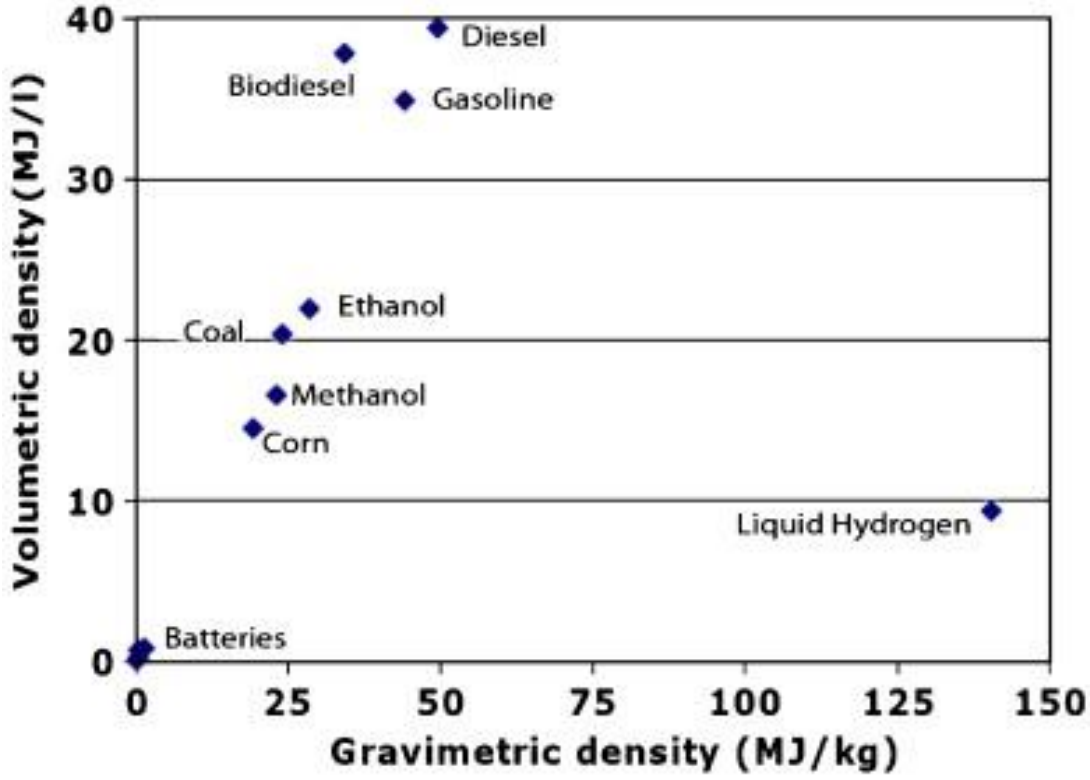

Figure 1-4 Caloric energy density of lithium ion batteries and liquid fuels [8]

Hydrogen can be utilised as a fuel in fuel cell, which are electrochemical devices that convert chemical energy to electrical energy [9]. Fuel cells have main applications in vehicles, stationary power and portable electronics, although the distribution of hydrogen fuel is problematic as the energy infrastructure is geared towards fossils.

1.2.1 Hydrogen infrastructure

While the current infrastructure is not designed for a swift transition to hydrogen energy, recent developments have given electrolysis a key role in the Hydrogen Roadmap programme for the UK [10]. This government and cross-industry programme aims to make hydrogen powered travel in the UK a reality by developing the hydrogen infrastructure and fuel cell electric vehicles.

Elsewhere in Europe, a key policy on energy generation from renewable sources was published by the German government in September 2010, six months before the Fukushima nuclear accident, with supporting legislation being passed in 2011. It declares that by 2050 the proportion of renewable electricity in Germany is expected to reach at least 80% [11]. This requires restructuring of the energy infrastructure, which is inconceivable without the storage of energy in the form of hydrogen. The policy has resulted in expansion of renewable energy in Germany, particularly wind power. The share of renewable energy in Germany's gross electricity consumption almost doubled between 1999 (5.4%) and 2005 (10.1%), and more than doubled again by 2012 to around 23%. An approach that follows on from the initiatives in Germany and Great Britain, amongst others, is taking place in France. The French Hydrogen Infrastructure Programme, or Mobilité Hydrogène France, has launched a national study to produce an economically competitive, and supported deployment plan, for a public and private hydrogen refuelling infrastructure in France between 2015 and 2030 [12].

These consortiums are being formed in parallel to a draft European Directive to promote the development of alternative fuels such as hydrogen, which is currently being considered by the European Parliament and the European Council [13]. Formations of these programmes are vital in guiding the deployment of hydrogen as they allow relationships to be developed and manufacturers to enter the market with their products and they show that there is strong political drive for a successful hydrogen market in the future. The EU has specific Hydrogen production cost targets of €16.60/kg in 2010, reducing to €9.90/kg (£8.49/kg) in 2015 and €5.50/kg in 2025. Furthermore the efficiency targets are 65% by 2010 and 70% by 2020.

Outside of Europe, the United States Energy Department has launched H2USA, which focuses on advancing the hydrogen infrastructure to support more transportation energy options for US consumers, including hydrogen fuelled vehicles. It brings together car manufacturers, government agencies, gas suppliers, and the hydrogen and fuel cell industries to coordinate research and identify cost-effective solutions to deploy infrastructure that can deliver affordable, clean hydrogen fuel in the United States [14]. Assistant Secretary for Energy Efficiency and Renewable Energy, David Danielson, said:

"Fuel cell technologies are an important part of an all-of-the-above approach to diversify America's transportation sector, reduce our dependence on foreign oil and increase our competitiveness in the global market. By bringing together key stakeholders from across the U.S. fuel cell and hydrogen industry, the H2USA partnership will help advance affordable fuel cell electric vehicles that save consumers money and give drivers more options." [15]

Through H2USA, industry and government partners will focus on identifying actions to encourage early adoption of hydrogen fuel cell electric vehicles, conduct coordinated technical and market analysis, and evaluate alternative fuelling infrastructure that can enable cost reductions and economies of scale.

For example, infrastructure being developed for alternative fuels for fuel cell applications, including tri-generation that produce heat, power and hydrogen from natural gas, biogas, or electrolysis may also provide low cost hydrogen for transport. In addition, increased fuel cell deployment for combined heat and power, back-up power systems can help pave the way for mainstream hydrogen transport infrastructure. These political, economic and environmental drivers for a hydrogen infrastructure mean that the emerging market for hydrogen has huge potential and implications across the globe.

1.2.2 Strategy for powering electrolysers

To ensure appropriate use of hydrogen as a clean-fuel energy carrier, the strategy for powering electrolysers for hydrogen production will be from renewable energy and this has already been demonstrated in various projects. For example, the Hydrogen Office project has been developed by the Hydrogen Office Ltd, a non-profit organisation whose primary aim is to support the accelerated development of the Renewable, Hydrogen and Fuel cell sector in Scotland by raising the visibility of the technology. Based in Fife, the Hydrogen Office project is seeking to develop a cluster of renewable energy storage and fuel cell activities that will see the area lead the transition from carbon based fuels to new low, or zero, carbon based fuels of the future [16].

The Hydrogen Office building is powered by a renewable hydrogen and fuel cell energy system. A wind turbine at a local school generates electricity which is used to power all lighting and computers as needed in the Hydrogen Office building. Surplus wind electricity is used to produce hydrogen from water through electrolysis. This hydrogen is stored in a tank for later use. When there is insufficient wind to supply the Hydrogen Office, the hydrogen is used in a fuel cell. The fuel cell generates electrical power to supply electricity to the Hydrogen Office Building. The connections between these processes are shown in Figure 1-5.

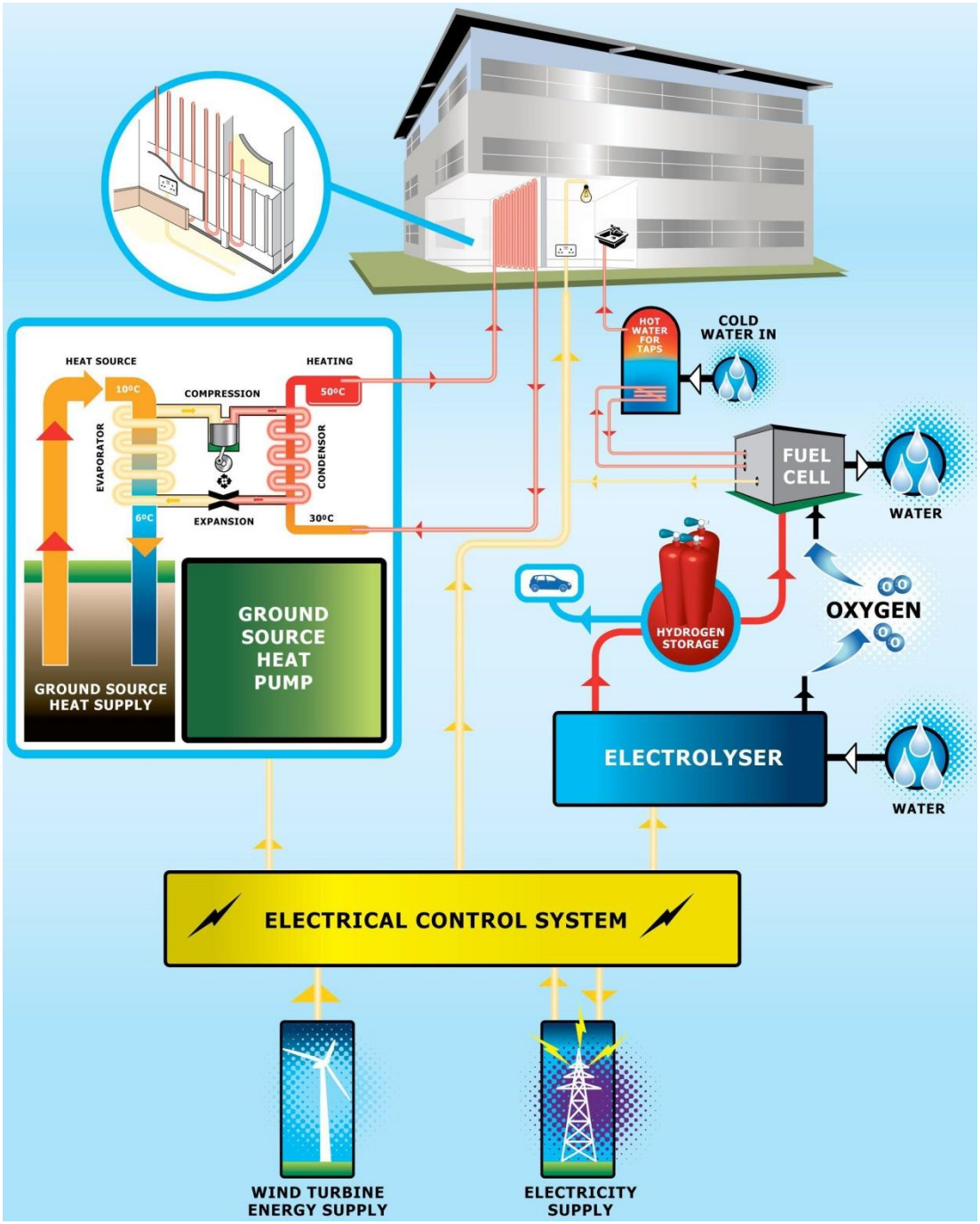

Figure 1-5 The Hydrogen Office project energy system [16]

The only by-products of the fuel cell are heat and water, thereby providing a unique working environment for businesses to set up where true clean, non-polluting and green building is a reality. This strategy for powering electrolysers through renewable energy is important if the technology is to strive as a clean fuel that will successfully assist in meeting the environmental targets discussed in section 1.1.

1.3 Hydrogen production

Hydrogen is the most abundant element in the universe; however on Earth it exists in only very small quantities in the atmosphere, less than 1 part per million. Hydrogen can be produced, or rather isolated, from natural compounds via a number of industrial methods including directly through photoelectrolysis [17], from dry biomass or coal through gasification [18], or algae photosynthesis [19]. However the current production of hydrogen is dominated by steam reformation of fossil fuels, oils or natural gas (hydrocarbons) [20]. This is not environmentally friendly as the process forms carbon dioxide as shown in Equation 1-1 and Equation 1-2.

$$CH_4 + H_2O \leftrightarrow CO + 3H_2$$ **Equation 1-1**

$$CO + H_2O \leftrightarrow CO_2 + H_2$$ **Equation 1-2**

The current energy infrastructure is dominated by fossil fuels and it is not designed for a swift implementation of hydrogen energy. Many technological and scientific challenges from the production, storage, transportation, distribution and use of hydrogen in fuel cells, need to be overcome in order for development of the infrastructure and operation of a hydrogen economy to become successful. This research focuses on the production of hydrogen from electrolysers, which is a proven technology and is perhaps the most promising method for producing hydrogen for the hydrogen economy of the future.

1.4 Water electrolysis

The electrolysis of water is seen as one of the easiest methods for producing hydrogen, offering the advantage of simplicity. An electrolysis cell requires no moving parts, can be designed as a portable unit, and produces hydrogen gas with purity greater than 99.9%. By contrast, other technologies such as steam reformation require external units to purify the gas from contaminants.

The electrochemical process of electrolysis is concerned with the transfer of charge, by movement of ions in liquid, solid or gaseous phases through which electrochemical transformation of species is achieved. When electrical energy is passed between two electrodes, through water, hydrogen and oxygen are produced by electrolytic decomposition according to Equation 1-3.

$$electric\ energy + H_2O \rightarrow H_2 + \frac{1}{2}O_2 \qquad \textbf{Equation 1-3}$$

The history of water electrolysis begins in the year 1800, when Nicholson and Carlisle [21] electrolytically split water and evolved gases using platinum electrodes. Over 100 years later, there were more than 400 industrial electrolysers in operation.

To minimise gas infrastructure costs, electrolysers can be located conveniently close to points of demand, or at large sites feeding into gas distribution infrastructures involving ships, tankers and/or pipelines [22]. Producing hydrogen so close to its point of use gives the option of producing it on demand, without the requirement for storage as a compressed gas or liquid. Extensive global markets also exist for hydrogen and oxygen outside of the energy sectors. The market for oxygen is slightly less than that for hydrogen; it is mainly dedicated to metal processing (approximately 90%), with the remainder being used for applications in the medical, military and space industry sectors. Approximately half of the hydrogen produced is used for

ammonia production, a third is used by the petrochemicals industry, and the remainder is for applications including methanol production, fat hydrogenation, generator cooling, weather balloons and rockets [22].

Like fuel cells, electrolyser technology is also well proven in industries where reliability and efficiency are paramount, and where alternative technology options are limited or more expensive, for instance:

- providing O_2 life support in space stations and submarines
- providing H_2 for industrial applications in developing countries, where hydrocarbon and electricity infrastructures are weak
- providing H_2 and O_2 in laboratory environments to eliminate the need to purchase relatively expensive bottled gas

As discussed in section 1.2.2, when powered by renewable sources of energy, electrolysis offers an efficient way of producing hydrogen with very little or no environmental impact. Even so, less than 5% of hydrogen produced is by this method due to the technology being far more expensive than the alternative hydrogen production technologies. Cost is the principal factor inhibiting the advance of electrolysers beyond the specialist applications they serve today. Decreases in unit cost are essential if electrolyser technology is to reach its future potential and until such cost breakthroughs are accomplished, the delivery of low carbon hydrogen in bulk will be inhibited. Although small electrolysers are sold by several companies as a cheaper and more convenient alternative to buying in bottled gas, competition within the hydrogen market appears limited. Even so, it appears that reliability, safety and convenience are the paramount sales features for electrolysers [22].

Due to the increasing demand for clean technologies, it can be envisaged that future economies will exploit electrolysis to produce low-carbon hydrogen for fuel cells and other uses. The carbon footprint of electrolysers is principally a function of their input electricity. Electrolysers can be combined with a renewable energy source such as solar power, hydroelectric or wind generators so that the hydrogen fuel produced

has a low carbon footprint. As an example, Aiken Electric Cooperative is developing houses which will use fuel cells in conjunction with a solar power system. The excess solar energy is typically converted into hydrogen, through electrolysis, and stored. This is fed back into the home energy system through a fuel cell when solar sources are low.

1.4.1 Categories of electrolyser

Typically, in all electrolysers there is a microporous diaphragm in the cell that separates the anolyte and catholyte. It acts as an ion exchange membrane, to complete the circuit in the cell, and also as a gas diffusion barrier, to prevent mixing of the resulting hydrogen and oxygen gases. Pure water is a poor electrical conductor so ions are usually employed in the form of an electrolyte. The type of electrolyte dictates the operating parameters and design materials of the electrolyser. There are three principal types of electrolyser, which refer to its type of electrolyte. The alkaline and acid electrolysers are well proven devices with thousands of units in operation, while the solid-oxide electrolyser is as yet unproven.

1.4.2 Solid oxide electrolyser

The operation of a solid oxide electrolyser relies on a solid ceramic electrolyte (such as zirconi) which at temperatures of 800-1000°C, transfers oxide ions (O^{2-}). Ceria based solid oxide electrolysers allow for operating temperatures of 500-600°C [23]. High fabrication costs and high temperatures are the two main factors that are retarding solid oxide electrolysers large scale production. By operating at these elevated temperatures, the heat input meets some of the energetic requirement for electrolysis and so less electricity is required per m^3 of H_2 generated when compared with the other electrolyser technologies. However, it does require a source of high temperature heat and to date prototype units have not achieved useful operational

lives. Also, substantial engineering problems exist regarding the gas sealing and thermal cycling. Accordingly, it is premature to make comparisons of solid oxide electrolysers with alkaline and proton exchange membrane electrolysers.

1.4.3 Acid electrolyser

Acid electrolysers are based on the transport of protons thus are known as proton exchange membrane (PEM) electrolysers. They are widely used due to their higher energy efficiencies than their alkaline electrolyser counterparts. More recently, electrolysis is preferred in alkaline environments because the corrosion is more easily controlled and cheaper construction materials can be used than in acidic based electrolysers. Alkaline electrolysers obviate the need for expensive platinum-based catalysts, which helps to lower its unit cost than that of a PEM electrolyser.

1.4.4 Alkaline electrolyser

Alkaline electrolysers operate at relatively low current densities of < 0.4 A/cm^2 and conversion efficiencies range from 60 - 90%. Without auxiliary purification equipment, gas purities are typically 99.8% and 99.2% for H_2 and O_2 respectively. Several large alkaline electrolysers of >100 MW have been applied, e.g. in Egypt and Congo to utilise hydropower and generate renewable hydrogen. A modern alkaline electrolyser will consume about 4 kWh of electricity per m^3 of H_2 generated at standard temperature and pressure (at an electrical energy conversion efficiency of approximately 90%) and deliver gas at up to 30 bar without auxiliary compression. However significant post-electrolysis electricity consumption is incurred for gas compression to deliver H_2 and O_2 at the pressures required by industry and for storage on-board hydrogen vehicles (350-700 bar) [24].

Traditionally the alkaline electrolyte consists of an aqueous solution of potassium hydroxide (KOH) or sodium hydroxide (NaOH) which supply the hydroxide ions that help facilitate the transport of electrons around the circuit. The basic components of an alkaline electrolyser are shown in Figure 1-6.

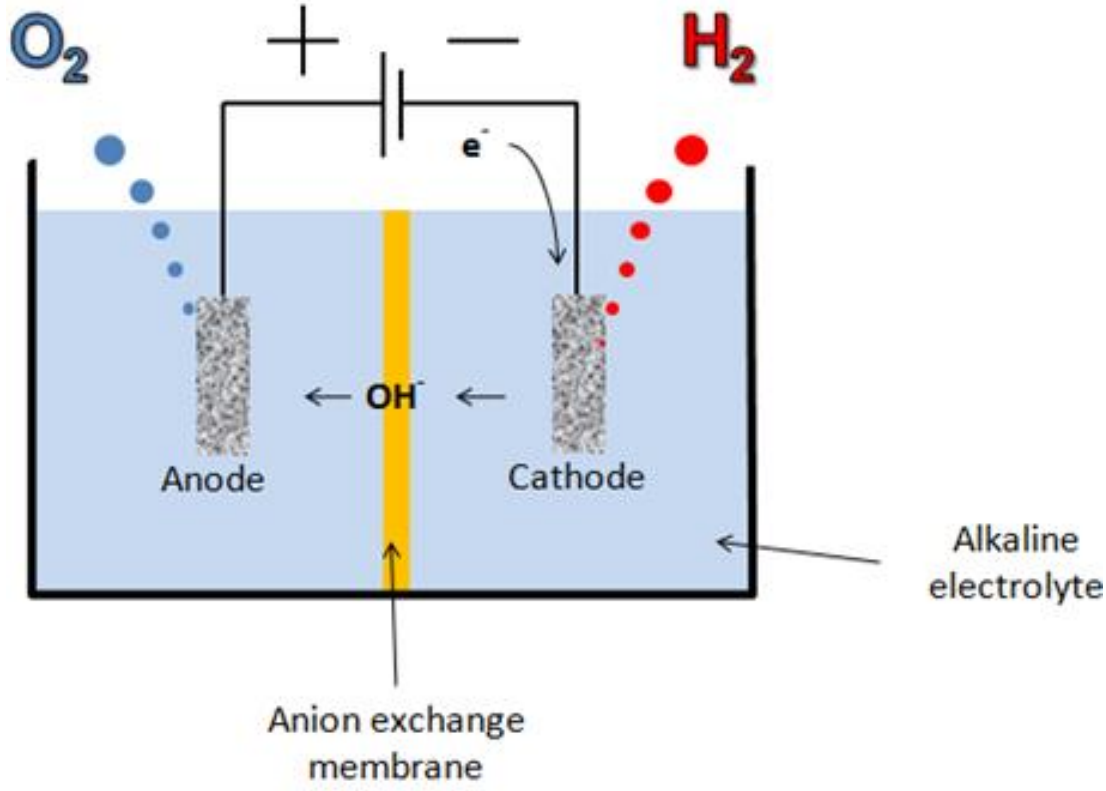

Figure 1-6 Basic components and operation of an alkaline electrolyser

At the anode oxidation occurs through the liberation of electrons:

$$2OH^- \rightarrow \frac{1}{2}O_2 + H_2O + 2e^- \qquad \textbf{Equation 1-4}$$

At the cathode reduction occurs through the uptake of electrons:

$$2e^- + 2H_2O \rightarrow H_2 + 2OH^- \qquad \textbf{Equation 1-5}$$

The overall net reaction is the decomposition of water (see Equation 1-3). The standard potential, E_0, for this electrolytic decomposition of water at 25°C is 1.229 V. In reality, to cause a given current density to flow through the electrode, actual cell potentials applied are higher than this theoretical potential and are composed of several parts:

- the electrolytic decomposition potential
- electrical and ionic resistances in the circuit
- electrode activation losses

Electrical resistances in the circuit restrict the flow of electrons in various connections and materials in the cell and thus the ionic transfer within the electrolyte solution. This is also known as Ohmic loss, or Ohmic resistance. Mass transport issues such as the availability of electrode surfaces due to partial coverage by gas bubbles formed, also contribute towards resistances. Bubble evolution on electrodes forces current to take a longer path around the bubble and also flow through constricted bubble-bubble contact areas thus the conductivity is decreased [25].

Electrode activation losses arise from reaction resistances due to the overpotentials required to overcome the activation energies of the electrochemical reactions occurring on the surfaces of the cathode and anode. This directly causes an increase in the overall potential of the cell. These intrinsic energy barriers of the reactions determine the kinetics of the electrochemical reactions [26] and are dependent on the surface activities of the electrodes employed.

The strategies in any effort to improve the energy efficiency of water electrolysis and thus the performance of the system must involve the minimisation of these resistances and reduction of the overpotential. The overpotential is the deviation of the electrode potential from its theoretical value required to cause a given current density to flow through the electrode [27]. The overpotential is a qualitative characteristic of electrode activity and namely low overpotential means high activity

and high overpotential means low activity. The overpotential can be calculated from the experimental potentials described in section 2.3.3.

1.4.5 Thermodynamics

Thermodynamics provides the framework for describing reaction equilibrium and thermal effects in electrochemical reactors. It also gives the basis for the definition of the driving forces for transport phenomena in electrolytes and leads to the description of the properties of the electrolyte solutions [28]. For low temperature H_2/O_2 electrochemical reactors, with an alleged maximum temperature of 100°C, various assumptions about the water splitting reaction are made.

- Hydrogen and oxygen behave as ideal gases
- Water is an incompressible fluid
- The gas and liquid phases are separate

According to the law of thermodynamics, chemical energy is being created therefore a minimum energy must be input to drive the process. For water to decompose, according to Equation 1-3, the voltage across the two electrodes must be greater than that corresponding to the free energy of formation (decomposition) of water plus the overpotential.

Based on the assumptions made earlier, the change in enthalpy (ΔH), entropy (ΔS), and Gibbs free energy (ΔG) of the water splitting reaction can be calculated, with reference to pure hydrogen (H_2), oxygen (O_2) and water (H_2O) at standard conditions (25°C and 1 bar). The total change in enthalpy for splitting water is the enthalpy difference between the products (H_2 and O_2) and the reactants (H_2). The same applies for the total change in entropy. The change in Gibbs free energy, ΔG, is expressed in Equation 1-6.

$$\Delta G = \Delta H - T\Delta S$$ **Equation 1-6**

This is the amount of work associated with the reaction. A reaction with a negative ΔG is spontaneous and can do work by releasing energy. A reaction with a positive ΔG is non-spontaneous and work must be done for the reaction to proceed. ΔG is related to E according to Equation 1-15.

$$\Delta G° = -nFE°$$ **Equation 1-7**

ΔG is also related to K according to Equation 1-8.

$$\Delta G° = -RT\ ln(K)$$ **Equation 1-8**

A fuel cell operates at a positive voltage potential because the reactions release net free energy (ΔG < 0). Electrolysis of water is non-spontaneous and operates at a negative voltage potential because the reactions require the addition of free energy (ΔG > 0). The standard Gibbs energy for water splitting is ΔG° = 237 kJ per mol of H_2. For an electrochemical process, operating at constant pressure and temperature, the maximum possible useful work (i.e., the reversible work) is equal to the change in Gibbs energy, ΔG. Faraday's law relates the electrical energy (emf) needed to split water to the chemical conversion rate in molar quantities. The emf for a reversible electrochemical process, or the reversible cell voltage, U_{rev}, is expressed by Equation 1-9.

$$U_{rev} = \frac{\Delta G}{zF}$$ **Equation 1-9**

The total amount of energy needed in water electrolysis is equivalent to the change in enthalpy ΔH. From Equation 1-6 it is seen that ΔG includes the thermal irreversibility TΔS, which for a reversible process is equal to the heat demand. The standard enthalpy, ΔH°, for splitting water is 286 kJ per mol H_2. The total energy demand ΔH is related to the thermoneutral cell voltage by Equation 1-10.

$$U_{tn} = \frac{\Delta H}{nF}$$ **Equation 1-10**

At standard conditions, U_{rev} = 1.229 V and U_{tn} = 1.482 V, but these will change with temperature and pressure. In the applicable temperature range U_{rev} decreases slightly with increasing temperature (e.g. at a temperature of 80°C and a pressure of 1 bar $U_{rev@80°C,\ 1\ bar}$ = 1.184 V), while U_{tn} remains almost constant ($U_{tn@80°C,\ 1\ bar}$ = 1.473 V). Increasing pressure increases U_{rev} slightly ($U_{rev@25°C,\ 30\ bar}$ = 1.295 V), while U_{tn} remains constant.

The heat of water's formation (also known as the higher heating value), ΔH_f, is -1.481 V. This is the minimum electric potential required for water electrolysis at standard state [29] [30]. The free energy of formation (also known as the lower heating value), ΔG_f, is 1.23 V. This is the maximum operating electric potential of a fuel cell at a standard state. The difference in potential is explained with Equation 1-11 and Equation 1-12.

$$\Delta G\left(-237.192\frac{kJ}{mol}\right) = \Delta H\left(-285.840\frac{kJ}{mol}\right) - T\Delta S\left(48.648\frac{kJ}{mol.K}\right)$$ **Equation 1-11**

$$H_{2(g)} + \frac{1}{2} O_{2(g)} \rightarrow H_2O_{(l)}$$ **Equation 1-12**

The equation includes the energy values for liquid water at 298 K (room temperature) according to Equation 1-12. The TΔS term is favourable for water electrolysis and may be contributed from the reaction environment. However, at room temperature, it is kinetically faster to obtain this energy from electrical energy rather than from the reaction environment's heat energy. Therefore, practical rates of water electrolysis require ΔH_f rather than ΔG_f. The -0.253 V of the TΔS term occurs on the HER at high pH and on the oxygen evolution reaction (described further in section 1.6.1) at low pH. Equation 1-13 considers the heat of water formation, ΔH_f, rather than the free energy of formation, ΔG_f, for the hydrogen evolution reaction (described further in section 1.6.2) in an alkaline system.

$$E^{\circ}_{H_2} = 1.228\,V - 0.0592.pH - 1.481\,V - 0.0295.log[pH_2]$$ **Equation 1-13**

In terms of electrical energy a voltage of greater than 1.23 V is necessary. However this figure is theoretical and in practice a working voltage of around 1.5 V is applied to the electrodes. This extra voltage is known as the overvoltage and represents excess energy used or loss of efficiency.

Efficiency is principally a function of the membrane and the performance of the electrocatalyst. This becomes crucial under high current operations which are necessary for industrial applications. Advanced electrolysers strive towards a reduced operational voltage, which reduces the cost of electrical power and therefore the operational cost of the electrolyser. However, ohmic resistance in the electrolyte increases with increasing current due to increasing gas bubbling. An increase in current density also leads to increased overpotentials at the anodes and cathodes [28].

1.4.6 Carbonation in alkaline systems

The corrosion activity of alkaline electrolytes towards catalysts is much less that their acidic counterparts. Despite the advantages that an alkaline electrolyte can offer, problems encountered are due to the liquid alkaline electrolyte being responsible for carbonation of a system that is sensitive to CO_2.

In an alkaline environment CO_2 can react with the OH^- ions to form carbonates and bicarbonate (CO_3^{2-}/ HCO_3^-).

$$CO_2 + 2OH^- \rightarrow (CO_3)^{2-} + H_2O \qquad \textbf{Equation 1-14}$$

Upon formation there is precipitation of large carbonate crystals (commonly Na_2CO_3 or K_2CO_3 depending on the electrolyte used) which can lead to potential blockages of the electrolyte pathways and electrode pores.

$$CO_2 + KOH \rightarrow K_2CO_3 + H_2O \qquad \textbf{Equation 1-15}$$

The crystals can mechanically disrupt and destroy active layers, thereby impairing the performance of the cell. Not only are the pores restricted but there are a reduced number of hydroxyl ions available which reduces the ionic conductivity of the electrolyte solution [9]. This can increase the electrical resistances and thus the overpotential of the system. A system with higher overpotential has increased costs associated with the energy consumption required to operate the electrolyser.

1.5 Polymer electrolyte membrane

Improvement in the energy efficiency of water electrolysis and thus the performance of the system must involve the minimisation of the resistances within the system. Successful operation of any electrolyser requires an intimate contact between the electrode, electrocatalyst and electrolyte [31] where the reactions take place. Modern electrolysers adopt 'zero-gap' cell geometry, where the anode and cathode are pressed against the membrane. This electrolyser differs from a bulk electrolyser primarily because it employs the solid polymer electrolyte which utilises the concept that the ion-exchange membrane is used as the electrolyte as well as the membrane.

1.5.1 Alkaline anion exchange membranes

Solid polymer electrolytes are employed in industrial electrolysers because they obviate the issues associated with the liquid electrolyte, but retain the advantages of an alkaline environment. Many developments have been made in the past with alkaline anion exchange membranes (AAEMs) being employed as a solid polymer.

The solid polymer electrolyte technology is derived from General Electric's fuel cell work of the 1960s, which provided the solid polymer electrolyte based H_2/O_2 fuel cells in the Gemini space-flight program during that decade. Ionic conductivity is provided by the mobility of the hydrated ions within the solid polymer electrolyte membrane. The membrane allows for pure deionised water to be circulated through cell and this not only eliminates the need for a corrosive electrolyte but also enables for a more compact electrolyser design. The technology has potential for a broad application if the use of noble metal catalysts and other high cost components can be minimized.

General Electric's membrane is made from a perfluorinated polymer to which sulphonate groups are chemically attached. The membrane's ion exchange and

hydrogen ion conduction properties stem from this feature. Later developments by DuPont produced a material called Nafion, a fluorinated copolymer that set the benchmark for conductivity and performance. It can be utilised in fuel cells and electrolyser systems, although the cost of this material is very expensive (approximately £1200/m^2).

A suitable membrane's main priority is low gas permeability so to avoid crossover of hydrogen and oxygen. It must also exhibit low ionic resistance and it requires a polymer that shows good alkaline and temperature stability in the long and short term. The research group of Varcoe have made developments with ETFE, which is partially fluorinated [32].

Submersing the polymer in a hydroxide solution (e.g. NaOH or KOH) converts the head groups to OH^-. An outstanding issue and research priority of AAEMs is to find a chemically stable head group. Previous work on AAEMs suggest that anion exchange membranes are not stable in this hydroxide form at temperatures above 60°C due to the Hofmann mechanism and nucleophilic substitution mechanisms that result in degradation of the head groups [33].

Small amounts of highly dispersed catalysts are deposited against both sides of the membrane to form the cathode and anode. This feature enhances the triple interface of the catalyst, electrolyte and electrode where the intrinsic electrochemical reactions take place. Improving this triple interface is one of the research challenges of hydrogen production through electrolysis and the aim is to reduce this overpotential as much as possible.

1.5.2 Membrane electrode assembly

The triple interface is primarily encompassed by the membrane electrode assembly of an electrolyser cell. The membrane electrode assembly primarily ensures an

uninterrupted electrical contact between the current collector and electrodes. Optimal performance and a reduced overpotential is achieved by ensuring intrinsic connection between the electrode, electrolyte and catalyst interfaces in order to decrease the internal ohmic drop. Physical contact between the electrodes and the separator requires the electrodes to consist of a porous electrocatalytic material thus ensuring the triple contact between the electrode separator and the electrolyte. This connection, or immediate contact, is dependent on the materials and how they are assembled in the electrolyser.

A gas diffusion layer (GDL) in the membrane electrode assembly provides a conductive and porous structure, which ensures diffusion of reactants and products to and from the entire electrode area. This also allows the water to be in contact with the entire surface area of the membrane. For water electrolysis the GDL should have a hydrophilic property to supply water to the oxygen electrode [34]. Gases are the reaction products and need to be able to get away from the MEA, so electrolysers need a balanced ratio. Carbon cloth is usually adopted as the GDL and was introduced to help reduce the noble metal loadings within electrochemical cells. However, carbon materials tend to oxidise at high potentials on the oxygen evolution side (according to Equation 1-16) during electrolysis, so its use on the anode should be avoided.

$$C + 2H_2O \rightarrow CO_2 + 4H^+ + 4e^- \qquad \textbf{Equation 1-16}$$

$$E^0 = 0.118\ V\ vs.SHE\ at\ 25°C$$

1.6 Electrocatalysts

Catalysts are applied in chemistry to aid the reaction rate of chemical reactions which would otherwise happen very slowly. Catalysts in electrochemistry are more important for facilitating the ionic transport and resulting electrochemical reaction. Trassati [35] identifies the main prerequisites for electrode materials as:

- High surface area
- High electrical conduction
- Good electrocatalytic properties
- Long-term mechanical and chemical stability at the support/active layer and at the active layer/solution interface
- Minimized gas bubble problems
- Availability and low cost

Electrode materials exhibiting these prerequisites are based on metals and their compounds from the transition metals area of the periodic table, which is highlighted in Figure 1-7.

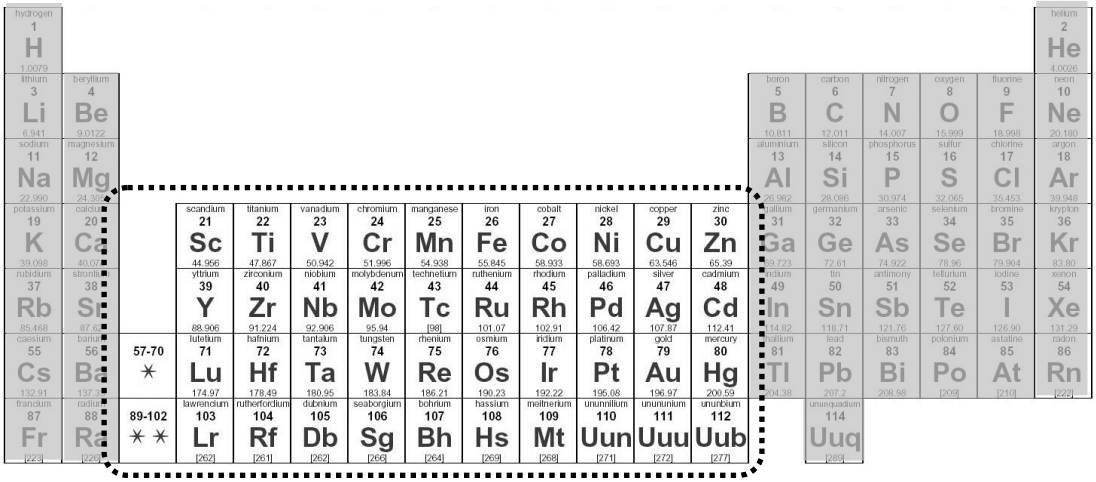

Figure 1-7 Periodic table of elements highlighting the transition metals

The transition metals can be split into two main groups, precious or noble metals, and non-noble metals. Presently the most superior catalysts are based on the noble

metals such as platinum, ruthenium and iridium. These elements and their oxides include perovskite, spinel and rutile type structures. Unfortunately noble metals are far less in abundance than non-noble metals and consequently their market prices are far higher. The drastic difference in market prices is shown below (average of 2011 prices):

- Platinum £1131 per ounce
- Iridium £660 per ounce
- An ounce of nickel and cobalt for less than £1

Furthermore, market trends show the cost of noble metals is set to remain high. The market price of iridium over the last 7 years is shown in Figure 1-8.

Figure 1-8 Increase in global market price for iridium in the 21st century [36]

Peter Duncan, Johnson Matthey's general manager for market research, commented on the price rise and told Reuters news agency that the upward trend is:

"not speculative, there is real industrial buying driving it. One sector that is a considerable driver of iridium demand is the chloro-alkaline industry, accounting for about 20'000 ounces."

Iridium is used as a catalyst coating on electrodes in the chloro-alkaline industry and also plays a vital role in the manufacture of backlit screens in modern technology. Similar market trends exist for the other noble metal catalysts based on platinum and ruthenium.

Progress has been made to reduce the loadings of noble metals on electrodes in electrolysers and fuel cells, whilst still maintaining high performances. However the cost of these materials means that, economically speaking, a complete substitution of the materials with non-noble metals is a greater long term solution for the technology. Noble metals can be substituted with many other transition metals which are far more abundant, cheaper and can fulfil the requirements listed by Trassati previously.

Production and development of these materials as electrocatalysts for the anode (oxygen evolution reaction) and cathode (hydrogen evolution reaction) in an electrolyser is essential for reducing the operating potentials and making the technology more affordable.

1.6.1 Oxygen evolution reaction

The oxygen evolution reaction (OER) that takes place on the anode is slower than the hydrogen evolution reaction (HER) that takes place on the cathode and is the major source of energy loss in an alkaline electrolyser, due to its high activation overvoltage. The OER is complicated by the overall transfer of four electrons as opposed to a single electron transfer for each hydrogen molecule. Due to the slower

kinetics of the OER compared to HER, the vast majority of work in this project is centred on catalysts facilitating the OER.

The kinetics of an electrode can be expressed by the Tafel approximation (Equation 1-17), which demonstrates the characteristic rise in current density with electrode potential.

$$j = j_0 e(-\alpha f \eta) \qquad \textbf{Equation 1-17}$$

Where $j_0$is the exchange current density (described further in section 2.2.6), α is the activity coefficient, η is the overpotential at the anode (described further in section 2.3.3) and:

$$f = \frac{nF}{RT} \qquad \textbf{Equation 1-18}$$

Where n is the number of electrons transferred in Equation 1-4 or Equation 1-5, F is the Faraday's constant, R is the gas constant and T is the temperature.

The model applies to both OER and HER and a fundamental requirement for water electrolysis is for a high value of exchange current density to minimise overpotentials. This is a characteristic of the electrocatalyst that should also provide a large surface area for the current density to be distributed.

It is accepted that during electrolysis the OER occurs on conductive anodes where thin catalyst oxide films are present. The oxide growth is a parallel electrochemical process that accompanies oxygen evolution on a metals surface at the anode [37].

The most electrochemically active oxygen evolution anode materials are RuO_2 and IrO_2 since these oxides exhibit the lowest overpotentials for the reaction at practical current densities [37]. However RuO_2 has a shorter lifetime due to the easy

conversion of RuO_2 to RuO_4 at high potentials, which shows poor activity for oxygen evolution [38] [39]. A recent study by Leng et al. reported a current density of 399 mA cm^{-2} at a potential of 1.8 V in a polymer electrolyte electrolyser with a 1 M KOH electrolyte at 50°C and a Tokuyama membrane [40].

For non-noble, nickel and its oxides have become the anodes of choice for water electrolysis due to its high abundance, relatively low cost market value and it is highly corrosion resistant in alkaline systems. It appears to be the most suitable electrode material for oxygen evolution in commercial water electrolysers.

Nickel spontaneously forms a film of hydrous α-$Ni(OH)_2$ when it is submerged in aqueous alkaline solution [41] and four polymorphs are observed over the lifetime of the nickel electrode during oxygen evolution, α-$Ni(OH)_2$, β-$Ni(OH)_2$, γ-NiOOH and β-NiOOH.

Hydrous α-$Ni(OH)_2$ is unstable and tends to dehydrate to form a closely packed β-$Ni(OH)_2$ structure. Oxidation of β-$Ni(OH)_2$ leads to another closely packed structure, β-NiOOH. Direct oxidation of α-$Ni(OH)_2$ or prolonged oxidation of β-NiOOH on the other hand forms γ-NiOOH, which is the most stable state under oxidation at 'high potential' operation. These changes are summarised in the Bode scheme [42], displayed in Figure 1-9.

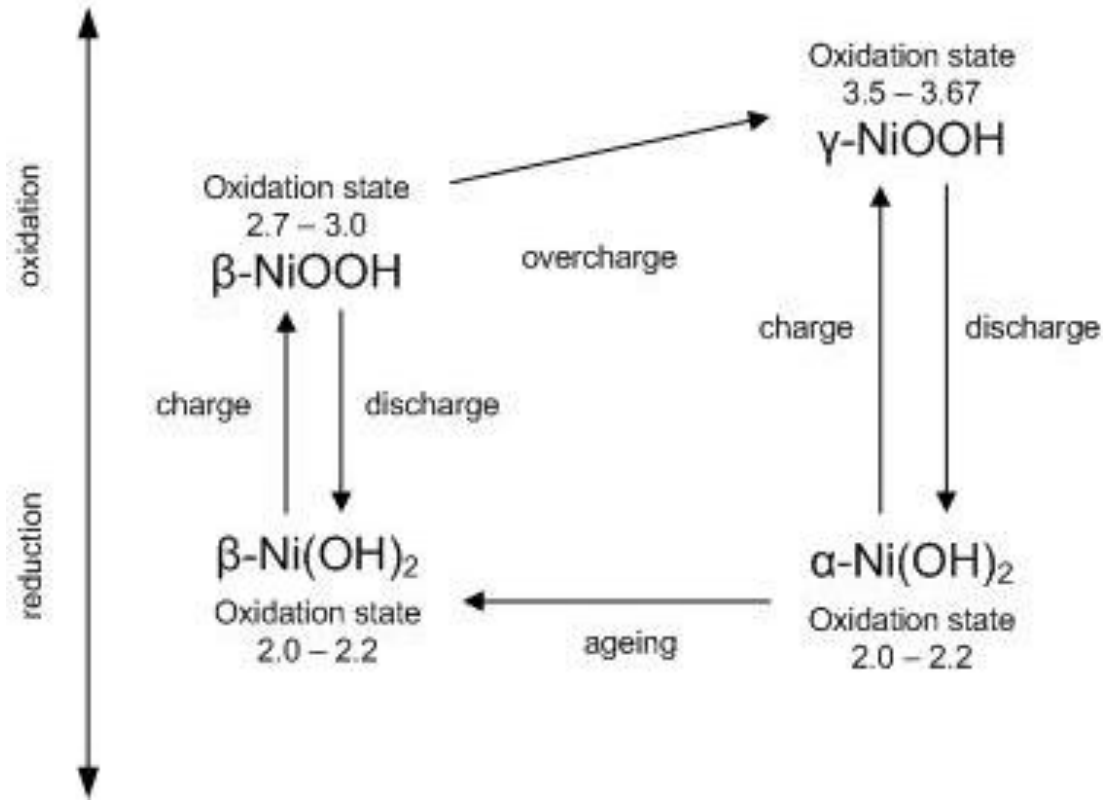

Figure 1-9 Bode scheme for $Ni(OH)_2$ / NiOOH redox transformations in alkaline systems [43]

The Bode scheme is well accepted as the route of transformation that nickel hydroxide can take when it experiences reduction and oxidation in an alkaline environment. Various nickel based compounds can be deposited onto electrode surfaces. For oxygen evolution, NiO, a anti-ferromagnetic oxide semiconductor, has received particular interest [44]. Cobalt and it oxides also exhibit promising OER catalyst properties [45] and there is evidence to suggest that combining metal oxides together can provide added benefits. Tseung et al. showed early identification of the potential for $NiCo_2O_4$ being used as a catalyst for OER [46]. Later work by Kinoshita [37] identified it as an efficient catalyst for OER.

Li et al. report a Ni-Fe electrocatalyst, report a current density of 1 A cm^{-2} in an alkaline polymer electrolyser (ITM Power membrane) with a 4 M NaOH electrolyte at 60°C at a potential of 2.12 V [47]. However they also report a current density of 1.89 A cm^{-2} in the same cell with 1M NaOH electrolyte at 80°C with a nickel microdisc at 0.8 V vs. Hg/HgO. The microelectrode has a very small geometric

surface area of 2 x 10^{-5} cm^{-2} (0.00002 cm^{-2}) which allows for iR free tests to take place, although the large current densities make comparisons with larger electrode systems more difficult. Furthermore they demonstrate no results for pure water being utilised in the electrolyser. One of the advantages of a polymer electrolyte is the ability to circulate pure water that, although reduces conductivity in the cell, eliminates the hazardous nature of the corrosive electrolyte.

Recent advances in non-noble metal catalysts include research completed by Wu et al. [48]. They deposited $Cu_{2.7}Co_{2.3}O_4$ on the anode with a loading of 3 mg cm^{-2} (however they utilised the noble metal platinum on the cathode 1 mg cm^{-2} on the cathode). They reported a current density of 1 A cm^{-2} in a polymer electrolyte electrolyser with a 1 M KOH electrolyte at 25°C. This performance was reduced to 84 mA when H_2O was introduced into the system at 25°C.

1.6.2 Hydrogen evolution reaction

A decrease in overpotential at the cathode can be accomplished by suitable electrocatalyst selection. Suitable materials are those that present high intrinsic electrocatalytic activity for the involved reactions, or exhibit high effective surface area. Additionally they must present satisfactory stability and low cost through containing non-noble metals.

For hydrogen evolution the noble metal platinum is preferred, though its cost makes its widespread implementation uneconomical [37]. Walsh describes materials suitable for electrodes including nickel and nickel molybdate [49]. Nickel molybdate is known to be the best non precious catalyst for hydrogen evolution [31]. Panek and Budiok electrodeposited nickel and molybdenum particles onto steel substrates [50]. They performed electrochemical studies with a 5 M KOH electrolyte at room temperature, which decreased the overpotential for a current density of 100 mA cm^{-2} by nearly 170 – 260 mV, when compared to nickel electrodes in the same system.

They attribute the performance increase to an increase in real surface area as well as the synergetic effect of molybdenum with the nickel matrix. Other recent research has been made on nickel molybdate in an alkaline electrolyser for the HER by Tasic [51] where the catalyst is electrodeposited onto nickel electrodes.

1.7 Catalyst synthesis and deposition

It is well known that the synthesis method has an effect on the physical and catalytic properties of electrocatalyst materials [52]. Electrocatalysts can be synthesised through a variety of methods, though the following are known for their simplicity and low costs:

- Thermal decomposition
- Chemical bath deposition
- Co-Precipitation

Each method involves the metal based oxides to be in the form of a liquid precursor, which undergoes transformation into a resulting metal oxide solid. Many factors influence the final crystal structure of the catalyst and thus the electrochemical behaviour. These factors include the concentration of initial precursors, stoichiometric ratio of any mixed oxides, pH, temperatures, time of reactions and the presence of any gases which the oxides would be exposed to.

1.7.1 Thermal decomposition

Thermal decomposition is a process where precursors of a metal salt are reduced to metal oxide catalysts at high temperatures. Heat treatment of a nickel salt will eventually lead to decomposition and the formation of NiO nanoparticles. The particle size and crystal structure is related to:

- Type of nickel salt used
- Heating rate
- Final, or maximum calcination temperature
- The length of time for heat treatment

- Oxygen flow rate

Chen investigated the thermal decomposition of nickel nitrate and nickel sulphate salts into NiO and discovered that the particle sizes from the nitrate salts (40 Å) were significantly smaller [53]. Work by Straszko [54] shows that the thermal decomposition of nickel sulphate salt in air leads to NiO at about 787°C. Another paper reports the SO_3 molecule is released at 840°C [53]. It is well known that higher thermal treatment leads to larger particle sizes so NiO synthesis through thermal decomposition of nickel sulphate should be avoided. It is known that nickel nitrate is thermally decomposed to NiO at temperatures of 400°C [55]. Due to the fundamental characteristic of an electrocatalyst requiring provision of a large surface area for the current density to be distributed it can be suggested that nickel nitrate is more appropriate for the preparation of a NiO catalyst. Brockner [55] and Elmasry [56] have investigated the stages of thermal decomposition that accompany the heat treatment of nickel nitrate salts and this is shown in Figure 1-10.

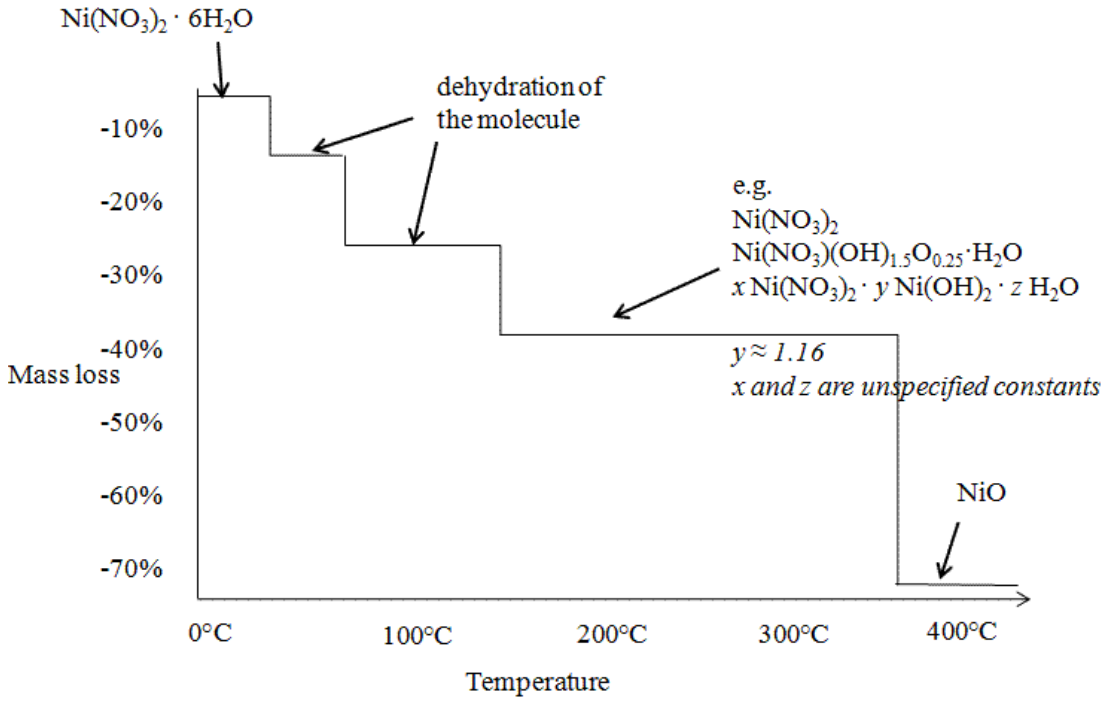

Figure 1-10 Mass loss with thermal decomposition of nickel nitrate salts

The intermediates which are formed depend upon the heating rate and the airflow rate. The literature reports that whilst heating under airflow the decomposition occurs

at lower temperatures and that one hour is a sufficient period of time for thermal treatment [56] [57] [58].

1.7.2 Solution growth with urea

Work reported by Pejova [59] shows that NiO with average particle sizes of 13 nm can be formed by a simple solution growth method. The NiO film's growth is based on thermal treatment of an aqueous solution containing Ni^{2+} ions and urea. The reaction mechanism is based on urea decomposing to CO_2 and NH_3 by heating to temperatures of around 90-100°C. The overall chemical reaction is expressed as:

$$3Ni^{2+} + 2NH_2CONH_2 + 10H_2O = 3Ni(OH)_2 \cdot 2H_2O + 4NH_4^+ + 2CO_2 + 2H^+$$

The thin films of $3Ni(OH)_2 \cdot 2H_2O$ have a terminal thickness of 0.9 µm, which is thermally decomposed to NiO by subjecting it to 400°C for 1 hour under air flow.

1.7.3 Chemical bath deposition

A porous film of NiO can be prepared by chemical bath deposition (CBD) as reported by Huang [60]. Films of this type are utilised as anodes in lithium-ion batteries [61] or as electrochemical pseudo capacitors [62], where charging capabilities of the catalyst layer is important. CBD is a process that enables the formation and deposition of thin films directly onto the surface of a substrate from a precursor solution. The technique is favourable because it benefits from low cost, operational simplicity and low temperature operating conditions. Xia reported a comparison of the preparation of NiO through the sol-gel and CBD methods and the resulting electrochemical activity between 0.2 and 0.65 V (vs. Hg/HgO) [63]. The conclusion was:

"The CV and EIS measurements revealed that the CBD NiO thin film had higher reactivity and reaction kinetics due to its highly porous structure"

The porous nature of this film and activity at low potentials makes this a promising structure to investigate further for the OER in alkaline electroysers.

The CBD procedure for NiO utilises ammonia and potassium persulphate, to reduce the nickel salts to metal oxides. No film formation is observed without potassium persulphate in a previous study by Han [64]. When nickel sulphate is used as a precursor it forms smaller particle sizes [< 20 nm] [65] than when nickel nitrate salts are used [24 nm] [66].

The growth mechanism of the deposited film has been investigated by Han [64] who found a relationship between the stirrer speed and the film's growth rate and final film thickness. Figure 1-11 shows the film growth curve after addition of ammonia (aqueous). The growth rate at its quickest when there is no stirrer speed and that the final film thickness decreased with increasing stirring speed.

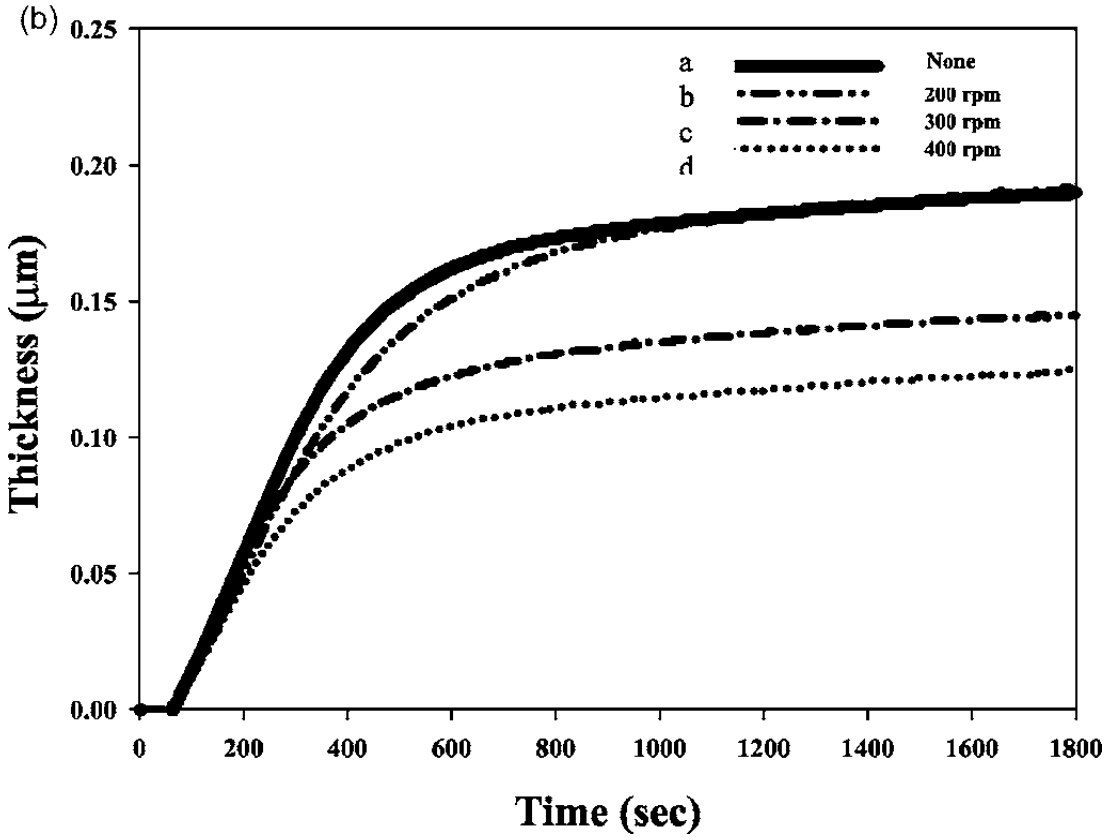

Figure 1-11 Growth rate of NiO films with different stirring speeds [64]

This result could be interpreted by a competition between heterogeneous film growth on the substrate and homogenous growth, and aggregation leading to particle formation. The resulting thickness is determined by the relative rate of these reactions. The linear growth rate at the start of film formation is relatively independent of stirrer rpm thus formation of nanoparticles on the substrate does not appear to be controlled by reactant mass transport.

According to Elimelech [67] an increased stirrer rpm may enhance the aggregation of nanoparticles in the solution through an orthokinetic mechanism. It is also possible that increased terminal thickness with decreasing stirrer rpm may indicate an entrapment of these homogeneously created particles. The final film thickness appears to be around 0.2 μm after 30 minutes.

1.7.4 Mixed metal oxides

Binary Ni-Co oxides have been successfully prepared by Hu et al. [68] through a dip coat followed by thermal decomposition that involved a final decomposition temperature of 400°C. They found that varying the nickel concentration would lead to an assortment of compounds.

Wu et al. investigated the effects of various stoichiometric ratios of cobalt to nickel, through electrodeposition [69]. Their preparation involved glycol additive to aid control of the viscosity. Varying this ratio alters the final crystal structure and Co^{3+} / Co^{2+} and Ni^{2+} / Ni^{3+} ratios, which results in altered OER results. Dechialvo and Chialvo prepared nickel cobalt oxide electrodes of different ratios by thermally decomposing mixtures of their nickel and cobalt nitrate salts directly onto nickel substrates using the dip coat technique [70]. With an overpotential of 0.32 V their maximum current density values were with spinels at a cobalt to nickel ratio of 2.

A study by Haenen et al. discovered that preparation parameters such as final thermal decomposition temperature, duration of the heat treatment and the catalyst loading determine the morphology of the oxide layer and so also influence the performance of the catalyst [71]. They prepared $NiCo_2O_4$ through thermal decomposition of nickel and cobalt nitrate salts at various temperatures between 250 and 600°C. They concluded that lowering the temperature of the final treatment leads to an increase in the electrochemical activity of the catalyst in 5 M KOH at 25°C. However they also concluded that at a heat treatment temperature of 250°C there was insufficient decomposition and consequently the mechanical stability was not satisfactory, since the electrodes tended to shed the $NiCo_2O_4$ oxide layer. The stability of their electrodes prepared at the temperatures of 300°C and above was considered good.

1.7.5 Co-Precipitation

The electrocatalyst nickel molybdate has been identified as the best non-precious metal catalyst for the HER in section 1.6.2. Many studies have already been done on the HER activity of the electrocatalyst after being prepared by electrodeposition onto metal substrates. Co-precipitation of electrocatalysts has already been achieved successfully by Klissurski [72].

Kaddouri [73] presents a method of preparing the nickel molybdate precursor $NiMoO_4.mH_2O.nNH_3$ through a conventional precipitation method using nickel nitrate, ammonium hepta-molybdate [$(NH_4)_6Mo_7O_{24}\cdot 4H_2O$] and ammonium hydroxide. Their method is based on previous work by Mazzocchia [74] who showed that the precursor obtained by co-precipitation depends upon the pH, temperature and ratio of nickel to molybdate particles. Table 1-1 summarises the conditions required for different precursors.

Table 1-1 Formula and precipitation conditions of $NiMoO_4$ ammonia precursors

pH	Temperature		Precursor obtained
	precipitation (°C)	filtration (°C)	
< 5.4	25	25	A a)
5.6	65		E b)
6	85	85	S c)
7.5	90	90	V d)

a) $A(blue) = (NH_4)_4H_6NiMo_6O_{24}.mH_2O.nNH_3$

b) $E = S + A\ (S = stoichiometric)$

c) $S(yellow) = NiMoO_4.mH_2O.nNH_3 (m = \frac{1}{3}; n = \frac{5}{3})$

d) $V(green) = S + Ni(OH)_2 (m = \frac{3}{4}; n = \frac{3}{4})$

The precursor S(yellow) can then be thermally treated at 550°C to form α-$NiMoO_4$.

1.7.6 Catalyst ink deposition

Catalyst nanopowders can be deposited onto substrates through a well established technique that uses a catalyst ink composed of the catalyst, binder and solvent. The binder enables the catalyst to 'stick' to the electrodes surface and maintains the catalyst film's stability in gas evolution conditions. It is important for the binder to be dissolved into the solvent with a known ratio of the catalyst nanopowder. This ratio will dictate the properties of the deposited film in terms of stability and electrochemical activity. If too little binder is used, the film could become mechanically unstable.

Due to their chemical nature, binding polymers are not conductive or electrochemically active so excess quantities increase ohmic resistances by reducing the active surface area of the electrode. Ionomer materials can be introduced which are conductive and assist to enhance performances of catalyst layers. A suitable solvent is one where the binder can be dissolved and the catalyst molecules are sufficiently dispersed. Thus the choice of binder and dispersion solvent will eventually determine the morphological properties and performance of the electrode. The substrate is held at an elevated temperature so that the solvent can evaporate, leaving behind a film containing the catalyst and binder. A homogenous dispersion ensures a high utilization of catalyst with improved surface area.

In 2006, Varcoe and Slade et al. [32] [75] reported making MEAs for AEMFCs by depositing polyvinyl benzyl chloride (PVBC) onto electrodes. Their MEAs containing this PVBC interface showed a substantial increase in the peak power density in a H_2/O_2 AEMFC at 50°C (from 1.6 to 55 mW cm^{-2}).

1.8 Research project aim and objectives

The aim of this research project is to eliminate the dependence on noble metal catalysts by developing and evaluating an anion exchange membrane electrolyser with inexpensive transition metal based catalysts. This will be achieved by undertaking certain objectives:

- Identification of non-noble metal catalysts suitable for use in alkaline electrolysis for hydrogen and oxygen evolution
- Synthesise nano-sized non-noble metal based catalysts
- Determine conditions for depositing catalysts onto the substrate materials to ensure mechanical and chemical stability of the catalyst films during gas evolution in the half cell electrolyser
- Investigation into various deposition methods of nano-sized catalysts onto suitable electrode substrates, using a range of catalyst loadings to identify behaviour of the catalyst films of various thicknesses.
- Investigation of the electrochemical activity (A cm^{-2}) of electrodes containing non-noble catalyst films in an alkaline electrolyte half cell, within operating potentials of 0.2 – 0.8 V vs. Hg/HgO, and at a range of catalyst loadings (mg cm^{-2}), through cyclic voltammetry and steady state techniques
- Reduce the ohmic resistances (Ω) and maximise the current density (A cm^{-2}) in the alkaline polymer electrolyser by investigating configurations of the membrane electrode assembly
- Use the research project's most promising non-noble catalysts for the OER and HER in an alkaline polymer electrolyser and examine the cell's performance and electrocatalyst behaviour

The thesis is divided into 5 chapters:

Chapter 1 introduces the global energy problem and an overview of hydrogen energy. A literature review of past and more recent alkaline technology is given. Suitable electrocatalysts for this research project are identified along with incorporation of the research requirements and priorities regarding development of materials in alkaline electrolysis. This leads into the aim and objectives of the research project.

Chapter 2 describes the electrochemical methods that were applied to the half cell, and polymer electrolyser, to assesses the electrocatalysts. Details are given on the various synthesis and deposition methods used for preparation of the non-noble catalyst films. Details of the construction and preparation of the half cell electrolyser and the polymer electrolyser are given.

Chapter 3 centres on the investigation of the electrochemical activity of the catalysts in the half cell for the oxygen evolution reaction.

Chapter 4 centres on further investigation of the most promising catalysts from chapter 3 in an alkaline polymer electrolyser. Various configurations of membrane electrode assembly are investigated so behaviours of the catalysts can be assessed with circulation of both pure water and an alkaline electrolyte.

Chapter 5 summarises the main conclusions of each chapter and gives recommendations for future work

2 Methodology

2.1 Introduction

This chapter gives details of the materials and methods used to achieve the aim and objectives of the research project. Electrocatalysts identified for development from the literature review include nickel based oxides and $NiCo_2O_4$ for the OER and $NiMoO_4$ for the HER. The chapter beings with an explanation of the electrochemical characterisation methods that are used to test these electrocatalysts. This is followed by details of the construction, arrangement and preparation of the glass half cell electrolyser, which was used for application of these electrochemical methods.

Methods are given on the synthesis of NiO through thermal decomposition, solution growth and chemical bath deposition techniques. The thermal decomposition method is also applied for the synthesis of $NiCo_2O_4$ along with co-precipitation for $NiMoO_4$. The techniques used to deposit these catalysts onto substrate materials are described.

The catalysts that showed the most promising results from half cell studies were tested further within an anion exchange membrane polymer electrolyser cell (also known as the polymer electrolyser cell). Details of the design and construction of the polymer electrolyser cell are given. Assembly of the polymer electrolyser cell is principally concerned with the selection and preparation of the materials in the membrane electrode assembly, which will be described in detail.

2.2 Electrochemical characterisation

An elementary requirement of any study in electrode kinetics is to obtain reliable information on the current density at an electrode surface, j, as a function of the electrode potential, E. Of the many variables involved in electrochemical kinetics, the electrode potential assumes a special importance as it affects not only the rate of reaction, but the number and types of electrode reactions as well as the nature of product [49].

Cyclic voltammetry (CV) is an electrochemical technique which measures the current density of an electrode to a linearly increasing and decreasing electrode potential. It involves sweeping the potential in a positive direction (also referred to as a positive-going potential sweep) at a constant scan rate, υ, until a predetermined value of current or potential is reached. Then the scan is immediately reversed towards more negative values (also referred to as a negative going potential sweep) until the original value of potential is reached. In some cases, this scan has a repeated number of cycles to determine changes in the current-potential curve produced with scanning.

Figure 2-1 shows a polarization curve (also known as a voltammogram) with the characteristic shape of the current responses governed by mass transport and diffusion processes. The visual representation of CV can help us to examine the electrochemical performance (specific activity) of electrodes.

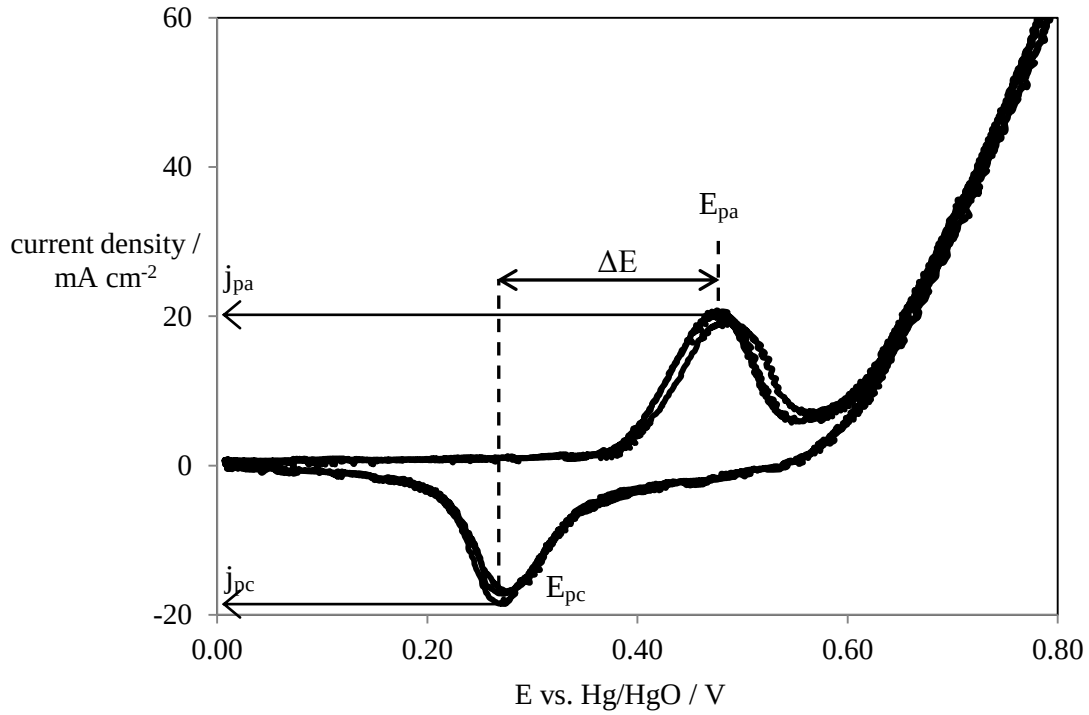

Figure 2-1 Example of a polarisation curve: Electrolysis with a nickel foam anode, a platinised titanium mesh cathode, an electrolyte of 1 M NaOH at a temperature of 25°C, and with a scan rate of 7 mV s^{-1}

When an electrochemically active compound is present, an anodic current peak at the potential E_{pa}, is detected with the peak current j_{pa}. When the potential is swept back during the reverse scan a further current peak, E_{pc}, may be observed with a cathodic peak current j_{pc}. Such peaks are usually observed for electrodes which are active for the oxygen evolution reaction. The difference in potential between where the peak currents are observed is given in Equation 2-1 as:

$$\Delta E = E_{p,a} - E_{p,c} \qquad \textbf{Equation 2-1}$$

The significance of the value of ΔE is related to the reversibility of the electrode reactions. If ΔE = 0 then the system is completely reversible and larger values of ΔE signify non-reversibility.

In this project CV is used for comparison of different electrodes through the evaluation of their electrocatalytic activity from the following main parameters:

- the onset potential of oxygen evolution
- the current density at a given potential
- Tafel slope values
- exchange current density

2.2.1 Reproducibility

If data is to be collected from cyclic voltammetry it is important that the voltammograms are reproducible so that analysis can be performed with greater accuracy. This was assessed by repeating CVs through positive-going and negative-going potential sweeps. For oxygen evolution this was performed in the potential window between 0.2 V and 0.8 V vs. Hg/HgO, at a scan rate of approximately 30 mV s^{-1}, until the voltammogram has stabilised.

2.2.2 Onset potential

The onset of oxygen evolution, E_{O_2}, is associated with the minimum potential required for the beginning of the process of production of oxygen molecules. Reducing this potential reduces the energy required for electrolysers to function, thus reducing the energy costs associated with hydrogen energy production. In other words a lower overpotential relates to better efficiency of the system through Equation 2-2.

$$Voltage\ efficiency\ \% = \left(1 - \left[\frac{E_{O_2}(V) - 1.229\ V}{1.229\ V}\right]\right) \times 100 \qquad \textbf{Equation 2-2}$$

Comparing the onset potential of particular catalysts is one way of identifying their superiority with regard to catalyst selection. A reproducible method of identifying the onset is required for legitimate catalyst comparisons. Exact potentials are hard to reproduce as the onset current of the process is very sensitive to the experimental conditions such as scan rate, temperature, the electrode material [76] and the start potential and accuracy of the potentiostat. Literature presents various methods for determining onset potential values. In 2000, Dang described the definition of onset as ambiguous and defined his onset through a mathematical interpretation [77].

> *"We chose to define the potential as the intersection point of two tangents drawn to the linear parts of the curve."*

Also in 2002, an alternative interpretation of onset comes from Roth: [78]

> *"The onset potential was defined as the potential at which 5% of the current value at 0.7 V was reached."*

However, at potentials below the onset potential, there is a current response that is greater than zero, i.e. I > 0 mA cm^{-2}. This varies on a number of factors, including interference from the potentiostat that fluctuates according to the current output range selected on the potentiostat, or a current response that arises from double layer charging as shown in Figure 2-1. These fluctuations mean the definitions described by Dang and Roth become unreliable.

The solution is to identify onset potential through slow or steady state linear sweep scan rates (υ < 1 mV s^{-1}) that make the nonfaradic double layer charging currents negligible. It was found that the most consistent and accurate way to identify onset potential was though the application of two graphical analysis methods. The first method is similar to that described by Zhang in 2002 [79]:

"The onset potential may be defined as the potential where an inflection is observed in the charge–discharge curve."

The onset potential is taken as the potential where there is a change in the gradient of the current response line. An example of this is shown in Figure 2-2, which shows the current response of an electrode with the same operating conditions that are applied to all electrodes experimented in the glass half cell electrolyser (electrolyte of 1 M NaOH at a temperature of 25°C; scan rate of 0.5 mV s^{-1}).

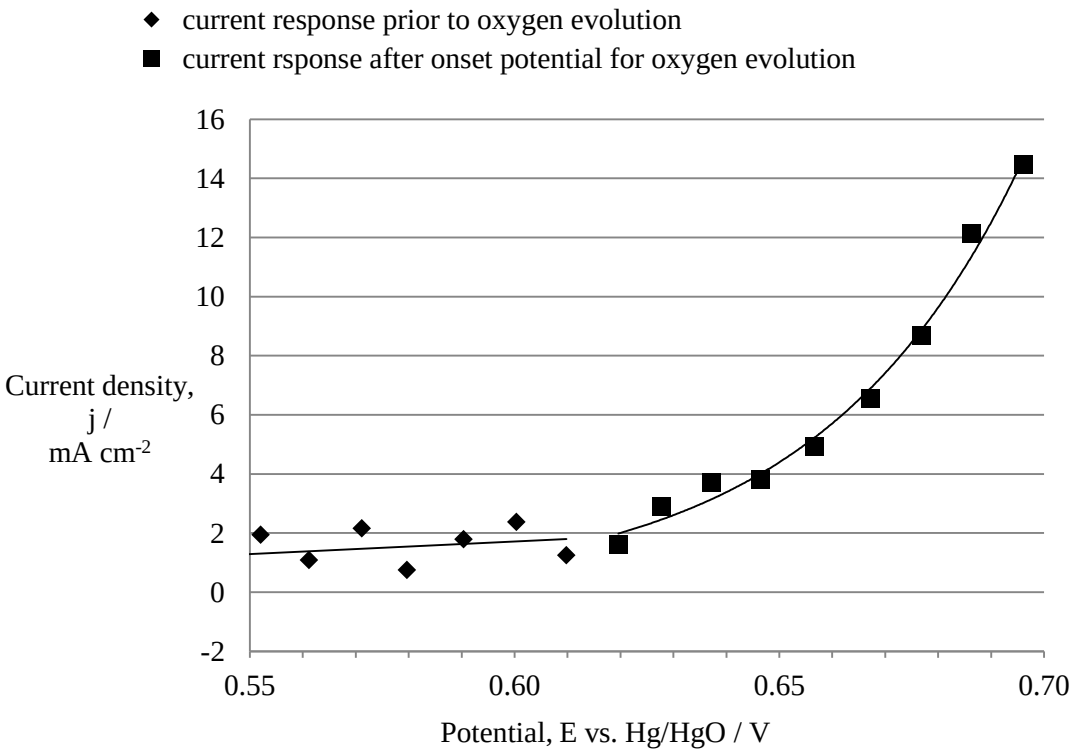

Figure 2-2 Current response encompassing the onset potential of oxygen evolution

The current response is initially linear, with fluctuations of ± 1 mA cm^{-2}, up to around 0.62 V vs. Hg/HgO. At potentials greater than 0.62 V vs. Hg/HgO there is evidence of a more exponential relationship between potential and the resulting current density, as oxygen evolution occurs. Due to the accuracy of the potentiostat and the way the linear relationship seamlessly blends into an exponential relationship, certain data points can be considered as part of both relationships which gives the interpretation of the onset potential an accuracy of ± 0.01 V.

The second graphical method comes from a plot of the log values of current density against the potential ($\log j \ vs. E$) as shown in Figure 2-3.

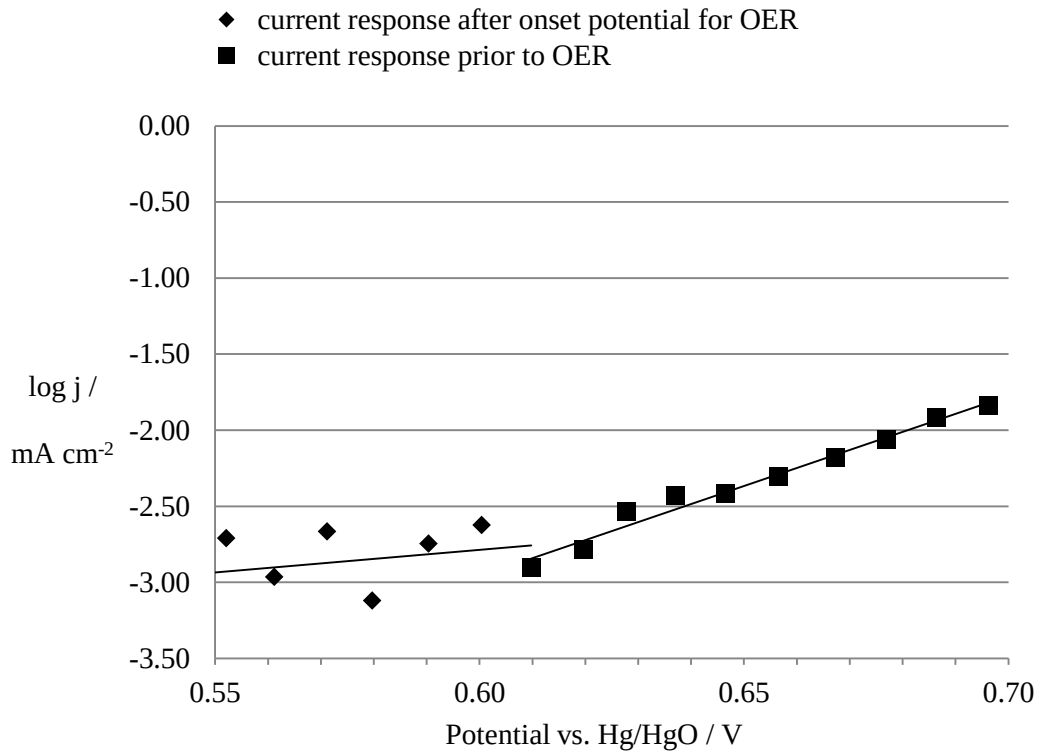

Figure 2-3 Identification of onset potential through Potential vs. log j charts

Two linear relationships exist, and the intersection of these relationships gives the onset potential for oxygen evolution. Like the previous method, certain data points can be considered as part of both relationships, which gives the interpretation of the onset potential an accuracy of ± 0.01 V. The actual onset is given as an average of these two graphical interpretations of the current response.

2.2.3 Current density at given potentials

Electrolysers usually operate at potentials of (1.7 V – 2.2 V) where practical current densities are achieved (> 0.2 A cm^{-2}). Assuming than no other reactions are taking place (e.g. metal dissolution) the Faraday law directly relates the current to the

amount of hydrogen (or oxygen) produced. To evaluate the electrocatalytic activity of catalysts, one can fix the current density (i.e. the hydrogen production rate) and compare the resulting overpotentials required to reach the given current density value.

Therefore this experimental method gives an indication of the amount of energy (overpotential) that should be invested to produce a specified amount of hydrogen (or oxygen). An arbitrary value of 0.800 V vs. Hg/HgO (1.726 V) was chosen as the potential for which current density values would be measured in the glass half cell electrolyser and this represents an efficiency of approximately 60%.

2.2.4 Steady state

Steady state experiments start at a potential where no electrode processes occur and the potential is scanned at a constant scan rate to 0.8 V vs. Hg/HgO. The potential scan rate is the rate of an electrical perturbation to the system in which the potential is altered linearly with time at a certain scan (or sweep) rate. A slow cycle is performed (~ 0.5 mV s^{-1}) so that nonfaradic double layer charging currents are negligible. This is repeated at least twice to ensure stability. Onset potential for the OER can be found from this plot as well as calculated Tafel slopes and current densities.

2.2.5 Tafel plots

The Tafel slope is indicative of the electrode reaction mechanism and sensitive to the catalyst films surface structure [80]. Tafel plots are collected from steady state CV scans run at < 0.5 mVs^{-1}. The potential (E), or overpotential (η), is plotted versus the $\log_{10}$ of the current density (j) [26].

$$E \; or \; \eta \; (mV) \; vs. log_{10} \; j \; (A \; cm^{-2})$$

The overpotential is based on the equilibrium potential:

$$\eta = E_0 - E \; (mV) \qquad \textbf{Equation 2-3}$$

The Tafel slope is taken when the relationship shows a linear response and the R squared values are greater than 0.995. The slope is measured in mV dec^{-1} (1/slope).

2.2.6 Exchange current density

The equilibrium potential represents the potential where there is no net current flowing through the electrode. It is dynamic one with the electrode reaction proceeding at equal rates both in the forward and in the reverse direction. This results in a zero net reaction rate and a zero net current. The exchange current density, j_0, of a reaction is the current density flowing equally in both directions in equilibrium. It is equivalent to the rate of an electrode reaction. Thus a large exchange current density indicates a fast reaction while a small exchange current density indicates a slow reaction [26]. With increases in temperature you get faster kinetics and bigger j_0 values, which were found by taking the exponential value of the intercept of the Tafel plot with the $log_{10} j$ axis.

2.2.7 Electrochemical impedance spectroscopy

Electrochemical impedance spectroscopy (EIS) is a method of measuring the material parameter, R_{Ω}, which is the Ohmic resistance of the electrolyser cell. Ohm's law states that:

$$voltage = current \times resistance \quad \textbf{Equation 2-4}$$

Rearranged for resistance:

$$resistance = {}^{voltage}/_{current} \quad \textbf{Equation 2-5}$$

The resistance is equivalent to the impedance of the electrolyser cell when the phase angle, θ, equals 0. Therefore Equation 2-5 becomes equivalent to:

$$Z(ohms) \rightarrow Z' = \frac{V}{I} \quad \textbf{Equation 2-6}$$

$$Z = Z' + jZ'' \quad \textbf{Equation 2-7}$$

Where Z' is the real impedance and Z'' is the imaginary impedance.

An important advantage of EIS is the possibility of using very small amplitude signals without significantly disturbing the properties being measured as it is non-intrusive. To make an EIS measurement, a small amplitude signal, usually a voltage between 5 to 50 mV is applied to a specimen over a range of frequencies from

200’000 Hz to 20’000 Hz. The EIS instrument records the Z' and Z'' components of the system in dB, which is converted to Z (ohms) according to Equation 2-8:

$$Z(ohms) = \left(10^{(dB/20)}\right)^{-1} \qquad \textbf{Equation 2-8}$$

2.2.8 Electrochemical measurements

The electrolyser is a non-spontaneous cell, which means that the direction of energy transformation is from electrical to chemical. The source and control of this electrical energy was from an EG&G Princeton Scanning Potentiostat, model 362. The potential and current measurements were recorded digitally via a Sycopel Scientific ltd. PCI-100 mk4 data logger interfaced to a personal computer. This equipment facilitated the performance of cyclic voltammetry and steady state measurements and is depicted in Figure 2-4.

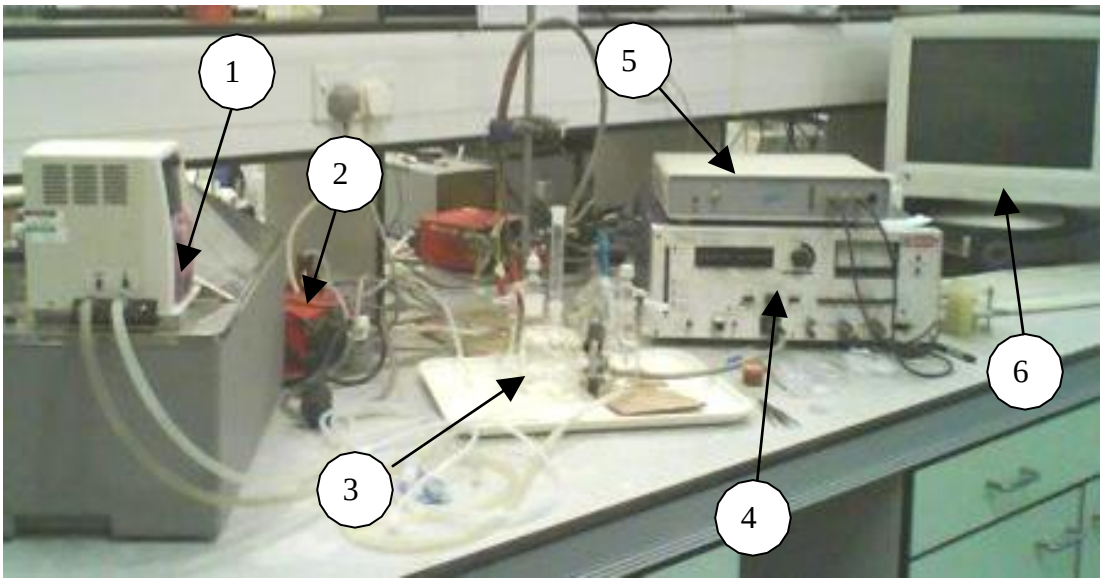

Figure 2-4 Equipment utilised for electrochemical measurements

1 - Water bath for temperature control

2 - Peristaltic pump for fuel supply for the anion exchange membrane electrolyser

3 - Electrolyser (the glass half cell electrolyser is shown in Figure 2-5 and the anion exchange membrane polymer electrolyser is shown in Figure 2-13

4 - Princeton Applied Research Scanning Potentiostat - Model 362

5 - Sycopel Scientific PCI-100 Potentiostat Computer Interface

6 - Computer

Low scan rates are given with an accuracy of 0.45 mV s^{-1} (+/- 0.05 mV s^{-1}) whilst higher scan rates are given to an accuracy of 28 mV s^{-1} (+/- 2 mV s^{-1}).

2.3 Construction and arrangement of the glass half cell electrolyser

Initial electrochemical studies of catalysts were performed in a three-electrode glass half cell electrolyser that enabled control of certain factors that influence the efficiency and performance of electrolysis. The glass half cell electrolyser comprises of two compartments, one with a working and reference electrode and another with a counter electrode that are under atmospheric pressure. These compartments are separated by an ion exchange membrane so that the hydrogen and oxygen gases produced do not mix. A photograph of the glass half cell electrolyser used in the experiments in Chapter 3 is depicted in Figure 2-5.

Figure 2-5 Glass half cell electrolyser with three electrodes; 1 working electrode, 2 reference electrode, 3 counter electrode

2.3.1 Ion exchange membrane

For the purpose of the glass half cell electrolyser experiments Nafion-117 was used due to its high availability, extensive durability and Na^+ conducting properties. It has been successfully utilised in alkaline water electrolysers in previous studies by Yeo [81] and Pomonarev [82]. Pretreatment of Nafion-117 ensures it is in Na^+ conducting form. In this procedure the Nafion membranes were submerged in 97%+ 1 M NaOH

(Sigma Aldrich) solution for 1 hour, whilst changing for fresh solution every 20 minutes.

Figure 2-6 shows that a change in the concentration of the electrolyte, and hence a change in the concentration of OH^- ions, influences the conductivity and transport of electrons through the solution.

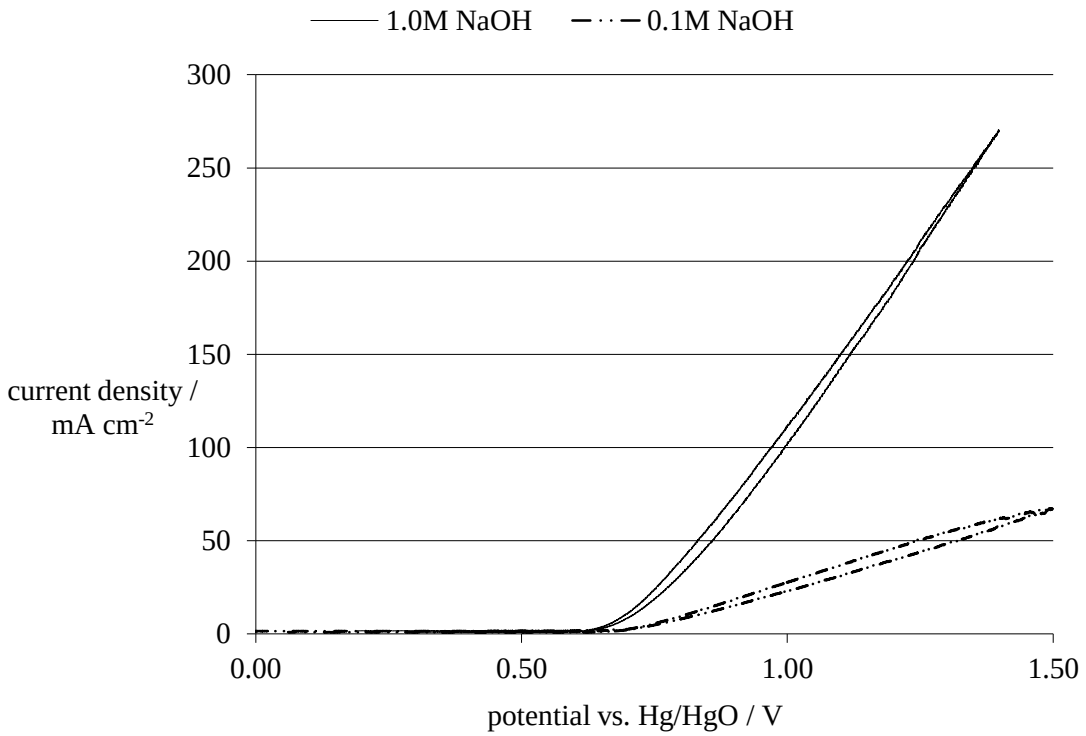

Figure 2-6 Effect of electrolyte concentration on the Ohmic resistance during electrolysis with a nickel foam anode at temperature 25°C and a scan rate of 0.5 mV s^{-1}

For consistency the electrolyte was kept as 1 M NaOH for all glass half cell electrolyser experiments. This was freshly prepared before each experiment with 98%+ purity NaOH pellets (Sigma Aldrich) dissolved in ultra pure DI water (≥ 18 MΩ resistance) to form a total volume of electrolyte of 100 ml. This gives a small ratio of electrode area to a solution volume. Passage of charge occurs through an alkaline electrolyte solution and experiments need to be carried out without significant changes of the concentrations of the reactant (and the products) in the bulk solution. Also due to the high concentration of hydroxide there will be minimal formation of carbonates which would affect results.

The temperature of the electrolyte has a significant effect on the performance, with higher temperatures increasing the kinetic activity of the electrodes. The temperature was controlled by a water bath, which circulates heated water to the jacket of the electrolyser with an accuracy of +/- 0.1°C.

2.3.2 Working electrode

The electrode of interest is the working electrode. Its potential is measured with respect to the reference electrode (see section 2.3.3) that has a well established, and reproducible, potential that is independent of the current density.

The reverse of the working electrode (that faces the opposite direction from the counter electrode), and the edges, are coated with an inert acetoxy silicone sealant (RS Components – Silcoset 158) which eliminates any activity from these surfaces, thus the exposed geometric surface area is 1 cm^2. Unless otherwise stated, all working electrodes within this three electrode system were made to this consistent geometry.

For this research project titanium was used for the working electrode due to its high durability and excellent conductive properties, yet it also exhibits minimal activity for the oxygen evolution reaction. This way, catalyst films which are to be deposited onto the substrate can be compared without interference from any background activity relating to the substrate. The activity of a titanium electrode towards the OER is shown in Appendix Section F and it shows < 1 mA cm^{-2} at a potential of 0.8 V vs. Hg/HgO (1.726 V vs. RHE). This low activity agrees with previous work done by Sanghi and Visvanathan [83]. The cause of this low activity can be attributed to the formation of a TiO_2 layer, which is an electrically insulating oxide.

Due to TiO_2 being a poor conductor of electricity the performance of any catalyst deposited onto the titanium would be drastically reduced and accurate

electrochemical studies of catalysts cannot be performed. It is necessary to prevent this coating from being formed and this can be achieved through etching the existing oxide layer off from the surface (through the pretreatment process described in section 2.3.5) followed by electrodeposition of an alternative metal that is more electrochemically stable.

In previous studies, Boggio eliminated the problems of the formation of a layer of TiO_2 by depositing a thin interlayer of RuO_2, obtained by thermal decomposition of $RuCl_3$, between the support and the active Co_3O_4 layer [84]. The RuO_2 prevented the formation of an insulating layer or TiO_2; however, RuO_2 is catalytically active and influenced the results of the experiments. A more suitable material would be gold, which shows very low activity for OER and HER, and is therefore chosen for this purpose.

Gold is a noble metal; however, its application in this research project was to provide an electrically conductive support so that non-noble metal catalysts could be tested without background interference from the substrate that the electrolyte was also in contact with. More importantly the high chemical stability of gold in alkaline solutions also made this a suitable choice of support.

Gold plated titanium electrodes were prepared from an electroplating bath containing gold(III) ions (in the form of anionic complexes $[AuCl]_4$) in hydrochloric acid solution. Titanium foils were pretreated through etching by submerging in a solution of HCl (10%) for 30 minutes at boiling temperature, which ensured thorough removal of the existing TiO_2 oxide layer. The gold electroplating bath was kept under ambient conditions and consisted of platinised titanium mesh as the positive anode and the etched titanium foil as the negative working cathode. Stirring reduced the potential required for a given current density and enabled it to be kept ≤ 0.9 V.

The resulting electrochemical performance of the gold plated titanium substrate, compared to a basic nickel electrode is shown in Figure 2-7. The voltammogram for gold plated titanium substrate shows a current response of 0.8 mA cm^{-2} at a potential

of 0.8 V vs. Hg/HgO. This is < 2% of the current density produced by a basic nickel electrode (42 mA cm^{-2}) in the same operating conditions. Even at 60°C, the maximum temperature induced on the half cell in this research project, the current produced is only 1.7 mA cm^{-2}.

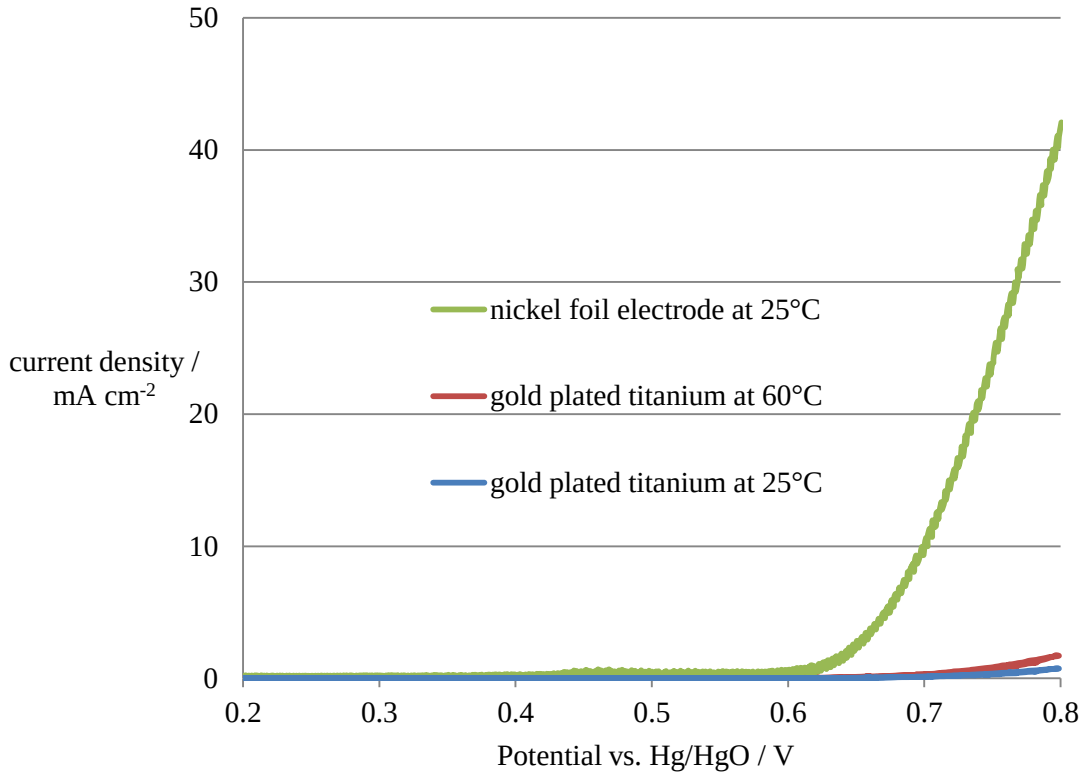

Figure 2-7 Comparison of the steady state current response of uncatalysed gold plated electrodes and a basic nickel electrode in the glass half cell electrolyser, with an electrolyte of 1 M NaOH and a scan rate of 0.5 mV s^{-1}

Due to these modifications any background effects of uncatalysed electrodes on the OER results in the glass cell electrolyser were assumed to be negligible.

After catalyst films were deposited on to the foil electrode they were spot welded to a length of titanium wire, 0.77 mm in diameter, which was encased in a glass rod. Exposed ends of the titanium were are also gold plated to eliminate the build up of a TiO_2 layer that over time would increase the resistance of the working electrode and lead to inconsistent results.

In the case of thermal decomposition and chemical bath deposition, the resulting catalyst films were bonded to the titanium electrode support in such a way that formation of TiO_2 does not occur. Therefore working electrodes prepared in section 3.4 and 3.6 consisted of the titanium support material only.

2.3.3 Reference electrode

In general, mercury/mercury oxide (Hg/HgO) reference electrodes are used in systems of high alkalinity [85]. The half-cell standard reduction potential for the Hg/HgO reference electrode in alkaline electrolyte agrees with the value of $E^{\circ}_{HgO,Hg} = 0.098$ V vs. SHE. The half-cell reduction potential for alkaline hydrogen evolution is expressed as the value of $E^{\circ}_{H_2O,H_2}$ = -0.828 V vs. SHE. Thus the potential of the reference electrode in NaOH at 25°C is 0.926 V vs. SHE and is independent of the concentration [43]. The equilibrium oxygen electrode potential, E°_{O2}, is 1.229 V vs. SHE. Thus E°_{O2} is 0.303 V vs. Hg/HgO. Potentials are corrected for electrolysis at higher temperatures.

In research literature regarding the OER it is common to express potential in terms of overpotential, η. In the case of this half cell, overpotential is related to the measured potential as:

$$\eta = E_{measured} + E_c^{\theta'}(Hg, HgO) - E^{\circ}_{O2}(SHE)$$

$$\eta = E_{measured} + 0.926 - 1.229$$

$$\eta = E_{measured} - 0.303\ V$$

The reference electrode works by sensing the solution potential at its open tip. A Luggin held the reference electrode and the small tip of the Luggin capillary, positioned near the working electrode, was open to the sodium hydroxide electrolyte. The capillary was used to bring the potential measuring point in close proximity to a working electrode under investigation. It consisted of a curved tube with a large opening to accommodate the reference electrode and a much smaller opening, only large enough to ensure diffusional movement of the electrolyte. The opening was positioned underneath the electrode so that gas evolved from operation of the cell, would not interfere with the tip. This device minimized any iR drop in the electrolyte associated with the passage of current in an electrochemical cell. Experimental data is not iR corrected.

2.3.4 Counter electrode

The counter electrode must not adversely affect the kinetics at the working electrode by altering the electrolyte composition. For water electrolysis, oxidation at the working electrode can be balanced by reduction at the counter electrode. It is imperative that the counter electrode size and reaction are such that the counter electrode reaction rate does not restrict the rate at the working electrode. To achieve this, a counter electrode with a relatively large surface area (to that of the working electrode) was employed. For all experiments regarding the oxygen evolution reaction a platinised titanium mesh, cut to a size of 2 cm x 3 cm, was used as the counter electrode for hydrogen evolution. For experiments regarding the hydrogen evolution reaction a piece of nickel foam, cut to 1.5 cm x 3 cm, was used as the counter electrode.

The counter electrodes were separated from the working electrode by a Nafion®-117 ion exchange membrane. It is an industry standard membrane primarily associated with proton conducting systems, and performances of other membranes are usually compared to it [86], however it can be used in alkaline systems due to its Na^+ conducting properties.

2.3.5 Pretreatment of titanium substrate electrodes

The objective of applying electrocatalyst coatings was to provide new properties to the base metal. Adhesion and stability of the catalyst layers depends on the condition of the substrate being plated and is a result of the pretreatment of the surface prior to the coating. Typical contaminants, including oils, dirt and fingerprints, can affect the functional properties of a substrate and thus the adhesion of any coating. Pretreatment consists of critical process steps used in the removal of these undesirable contaminants that might interfere with the inter-atomic adhesion. Figure 2-8 shows the process steps adopted in this research to prepare the surface of titanium for catalyst deposition.

Figure 2-8 Procedures for the pretreatment of titanium surfaces prior to catalyst deposition

Degreasing and cleaning

Prior to catalyst deposition the substrate was cleaned to remove any impurities that might adversely affect the performance of the electrolysis cell. A cleaner surface prior to catalyst deposition enhances the adherence of the catalytic layer and consequently the expected life time of the structured catalyst. Degreasing with solvents, such as acetone or isopropanol, removed oils that are usually immiscible with water. This process was enhanced through use of an ultrasonic bath to remove insoluble particles. Cleaning the substrate by submerging in boiling DI water helped to clear the pores from further contaminations. Rinsing with fresh DI water took place between each step to minimise any superfluous transfer of chemicals.

Etching

The next step encompassed the removal the oxide layer (previously discussed in section 2.3.2) by etching the surface of the electrode. If the oxide layer is not removed then it acts as an electrically insulating layer between the substrate and the catalyst, inherently reducing the activity of the electrode. Furthermore etching can increase the surface roughness of base metals, which can in turn lead to greater adhesion of any coatings and increase the active surface area.

Catalyst deposition

Some catalysts in the research project were deposited directly onto the electrodes due to the inherent nature of the catalyst synthesis method employed. Thermal decomposition and chemical bath deposition allowed for a precursor solution to be in contact with the electrode's surface and this resulted in a film of catalyst which was bonded to the electrode. In this case it was not necessary for the surface of the titanium to be coated in a stable layer of gold prior to catalyst deposition.

Other catalysts synthesized as nanopowder were deposited through formulation of an ink that contained a chemical binder (further details in section 2.4.6) that enabled the catalyst to adhere to the electrode. The binder is not electrochemically active so excessive amounts can severely degrade the performance of the electrode.

The method employed to control the catalyst loading was through measuring the change in mass of the electrode prior to, and after, the deposition process with a microbalance that had an accuracy of ± 0.1 mg.

2.4 Electrocatalyst synthesis and deposition on half cell electrodes

2.4.1 NiO synthesized by thermal decomposition

The thermal decomposition method described in section 1.7.1 was utilised to prepare electrodes with a catalyst film of NiO. Electrodes were pretreated according to the method in section 2.3.5, then immediately coated in an aqueous nickel salt and subjected to high temperatures. The change in the composition of the compound followed Figure 1-10. The remaining NiO was thermally attached to the electrode, allowing for strong mechanical stability and conductivity, therefore no binder was required. The process steps are summarised in the flow chart in Figure 2-9.

Attempts were made to thermally decompose a film of $Ni(NO_3)_2$ on the surface of 1 cm^2 gold foils. However practical challenges meant that electrochemical results were difficult to reproduce, due to an uneven distribution of the precursor nickel nitrate solution on the surface of the foils. The non-homogenous distribution of solution can be attributed to the fluid properties associated with the film, such as surface tension from hydrogen bonding. It was discovered that the most suitable form of substrate, for a solution of nickel nitrate to be thermally decomposed upon, was titanium mesh. This was most likely due to the solution's hydrogen bonding properties that enabled the film to embrace the strands of mesh whilst being heated with a hot air gun. The mesh used had a geometric surface area of 2.96 cm^2 and current densities were calculated from this area.

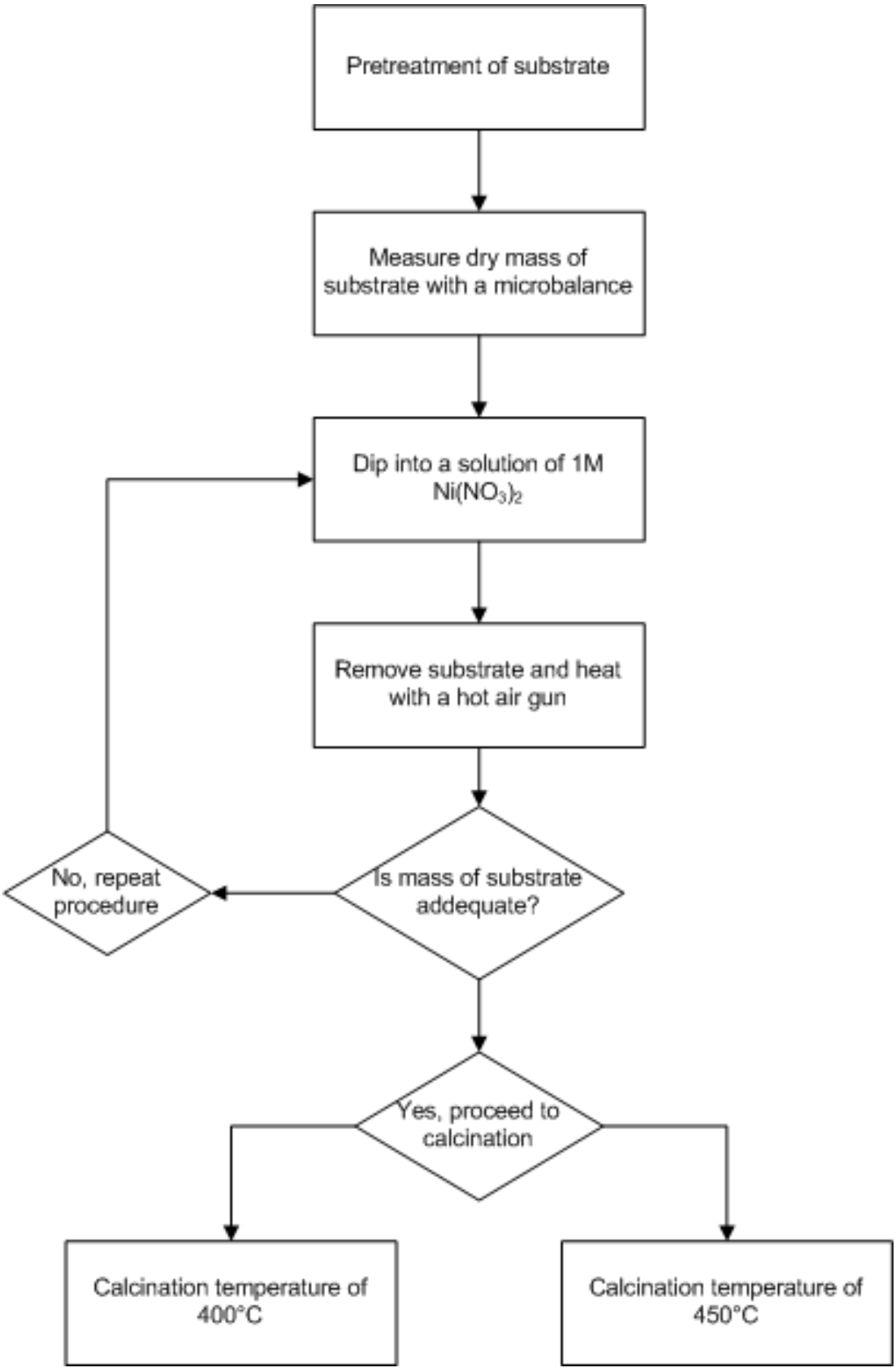

Figure 2-9 Procedure for the thermal decomposition of nickel nitrate salts onto a titanium electrode

Pretreatment of the titanium mesh electrodes was according to Figure 2-8. A solution of 1 M $Ni(NO_3)_2$ was prepared from nickel nitrate hexahydrate $\geq 97\%\ Ni(NO_3)_2.6H_2O$ (Sigma Aldrich) and DI water. The titanium mesh was dipped into this solution so that the surface was wetted with a hydrous film containing the nickel salts.

Upon heating with a hot air gun the dehydration stage described in Figure 1-10 took place. Removal of all the intermediates and final formation of NiO was achieved by heat treating in a furnace for 1 hour. An observation was made between the heat treatment temperature of electrodes and the resulting OER activity of the NiO, by conducting final heat treatment at temperatures of 400°C and 450°C. A lower temperature was not chosen as thermal decomposition would not be entirely complete. Various catalyst loadings were investigated and higher loadings were achieved by repeating the dip coat process as shown in Figure 2-8.

2.4.2 NiO synthesized by solution growth

The synthesis of NiO through a solution growth method, followed by thermal decomposition, followed the similar procedure to that adopted by Pejova [59] which was discussed in section 1.7.2. The NiO (urea) particles were prepared by mixing 50 cm^3 1 M $Ni(NO_3)_2$, 20 cm^3 1 M urea and 30 cm^3 DI water in a jacketed glass beaker. The solution was heated to 100°C and after approximately 30 minutes the solution appeared cloudy and bulk precipitation occurred. After two hours the precipitate was separated by micro filtration, washed with DI water and thermally annealed in air at 400°C for one hour in a ceramic crucible.

Attempts were made for the deposition to take place on gold plated titanium electrodes, however the films showed non-homogenous film distribution and mechanical instability when removed from the bath, even when alternative operating parameters such as temperatures and stirrer speed were investigated.

2.4.3 NiO synthesized by chemical bath deposition

The procedure for the preparation of NiO catalyst onto titanium electrodes is depicted in Figure 2-10.

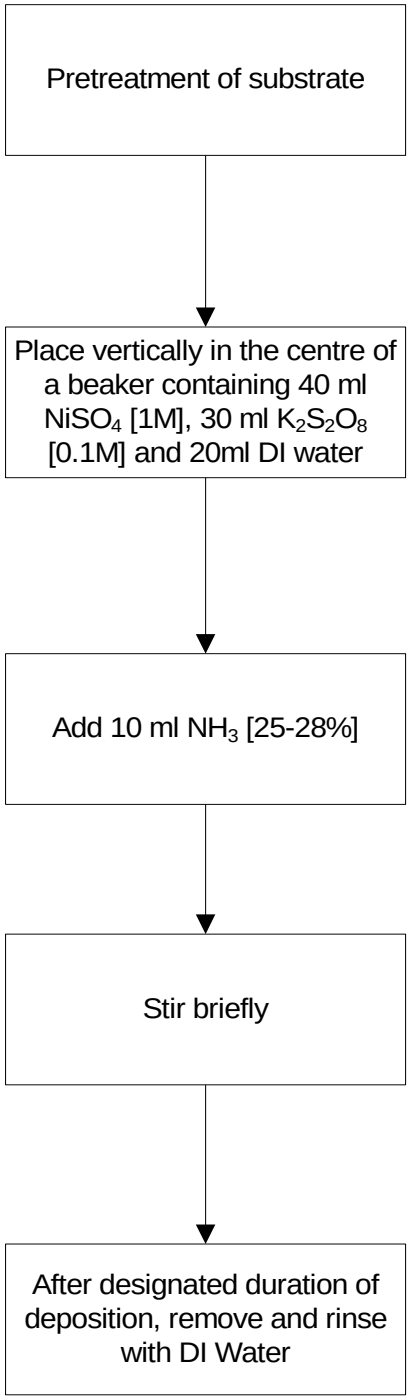

Figure 2-10. Process steps for chemical bath deposition

Titanium foil electrodes were cut to square pieces 1 cm by 1 cm and pretreated according to Figure 2-8 and then suspended vertically in a chemical bath. The chemical bath contained 40 ml of 1 M $NiSO_4$ (nickel sulphate), 30 ml of 0.25 M $K_2S_2O_8$ (potassium persulphate), 20 ml deionised water and 10 ml of 14 M NH_3 (aq.) [25-28% ammonia solution] maintained at 25°C in a jacketed glass beaker.

Persulphate is a strong oxidizing agent that is used to deposit oxides including PbO_2, MnO_2, Tl_2O_3, and NiO. The metal ions are oxidized by persulphate to higher oxidation states. However, the exact mechanism of oxide formation using persulphate is unclear according to the literature. Bukovec [87] suggests the electrochemical reaction:

$$S_2O_8^{2-} + 2e^- \rightarrow 2SO_4^{2-} \qquad \textbf{Equation 2-9}$$

Another possible mechanism is the hydrolysis of persulphate to form sulphate and hydrogen peroxide through the reaction:

$$S_2O_8^{2-} + 2H_2O \rightarrow 2SO_4^{2-} + H_2O_2 + 2H^+ \qquad \textbf{Equation 2-10}$$

Han [64] and Xia [62] believe the growth mechanism of NiO proceeds first through homogenous nucleation and precipitation of nickel hydroxide nanoparticles according to:

$$NO_3^- + H_2O + 2e^- \rightarrow NO_2^- + 2OH^- \qquad \textbf{Equation 2-11}$$

$$Ni^{2+} + 2OH^- \rightarrow Ni(OH)_2$$ **Equation 2-12**

These particles then react with the potassium persulphate at the substrate through a molecular level heterogeneous reaction as follows:

$$[Ni(H_2O)_{6-x}(NH_3)_x]^{2+} + 2OH^- \rightarrow Ni(OH)_2 + (6-x)H_2O + xNH_3$$ **Equation 2-13**

$$2Ni(OH)_2 + S_2O_8^{2-} \rightarrow 2NiO(OH) + 2SO_4^{2-} + 2H^+$$ **Equation 2-14**

Equation 2-14 is believed to be an important rate determining film growth step and helps explain why the presence of potassium persulphate is necessary for the formation of the NiO film. In this investigation electrodes were left in the bath for up to two hours to see if higher catalyst loadings could be achieved.

2.4.4 $NiCo_2O_4$ synthesized by thermal decomposition

$NiCo_2O_4$ was prepared with aqueous solutions of 1 M $Ni(NO_3)_2$ and 2 M $Co(NO_3)_2$ in the ratio of 1:2. Using a total volume of 3 ml the solutions were mixed and placed in a ceramic crucible in a tubular furnace that had air passing through. This was slowly heated to 95°C and held for 1 hour as overheating too rapidly caused the mixture to spit out of the crucible. Final decomposition took place at 280°C for 1 hour. A separate composition was decomposed at 300°C for 1 hour.

2.4.5 $NiMoO_4$ synthesized by co-precipitation

$NiMoO_4$ was synthesized as in a nanopowder form so that it could be deposited onto the carbon GDL by the airbrushing method. The objective was to form the precursor labelled S(yellow) in Table 1-1 as thermal treatment of the precursor $NiMoO_4.mH_2O.nNH_3$ at 550°C leads to the formation of $NiMoO_4$.

The procedure was replicated by utilising a 10 ml beaker containing 0.25 M ammonium hepta-molybdate which was heated to 85°C by a water jacket. The pH was slowly adjusted to 6 with pipette drops of 5 ammonia solution, whilst stirring continuously, in order to attain the required $[NH_3]/2[Mo]$ ratio. 0.25 M nickel nitrate was added drop wise to the beaker at a rate of 7 ml min^{-1}. The yellow precipitate $NiMoO_4.mH_2O.nNH_3$ was formed in the bath, which was filtered and thoroughly rinsed with hot DI water. This was thermally treated in a furnace under airflow at 550°C for 1 hour.

2.4.6 Preparation of catalyst layers in the half cell

Prior to electrochemical assessment of these catalyst powders, they were prepared into catalyst layers by depositing them onto the gold plated titanium electrodes that were discussed in section 2.3.2. By themselves, the catalyst particles would not adhere to the electrode substrate material so polyvinylidene fluoride (PVDF) is a polymer suitable for use as a binder. It has been successfully used in 3 M KOH solutions by Wang et al. [88] who prepared nickel foam electrodes with the catalyst $NiCo_2O_4$ and a PVDF binder for investigation into their capacitance. They utilised n-methyl-2-pyrrolidone (NMP) as a solvent which would dissolve the polymer and also disperse the catalyst particles.

Attempts were made by brushing catalyst inks onto electrode surfaces however it was found that this action agitated the surface of the film too much and a homogenous deposition could not be obtained. The adopted approach was through

use of pipette drops that allowed for a small volume of ink to be deposited on the titanium foil which was held at an elevated temperature of 80°C. With repeated drops the loading of catalyst could be controlled.

The optimum ratio of binder to catalyst was the minimum amount that enabled a mechanically stable film to remain on the electrode. This ratio was determined through preparation of catalyst inks with various ratios of binder to catalyst. Titanium and nickel electrodes were prepared with PVDF binding agents of 5, 12, 18 and 25 wt% of the catalyst mass. NiO (Sigma Aldrich) was employed as the catalyst in all electrodes with loadings between 0.5 and 1.5 mg cm^{-2}, which are commonly found in literature.

This was achieved by cyclic voltammetry in the glass half cell electrolyser between the potential of 0 and 1 V vs. Hg/HgO (between 0.926 and 1.926 V vs. SHE), at a scan rate of 20 mV s^{-1} for 30 minutes. The electrolyte used was 1 M NaOH and this was maintained at room temperature. As the proportion of binder to catalyst in the deposited catalyst film increased it was found that the mechanical behaviour of the catalyst film was altered and this is discussed below.

5% PVDF

At 5% PVDF the catalyst film was mechanically unstable enough to become detached upon immersion in the electrolyte solution.

12% PVDF

At 12% PVDF the catalyst films were mechanically stable enough to be immersed into electrolytic solution, however when a potential was applied, and upon the onset of oxygen evolution, the catalyst film was instantly lifted off the surface.

18% PVDF

At 18% PVDF the film was initially stable for oxygen evolution, however as the cycles continued the film gradually broke away. Figure 2-11 shows the gradual deterioration of electrodes prepared with 18% PVDF, removed from the cell after 5, 10, 15 and 20 minutes of cycling.

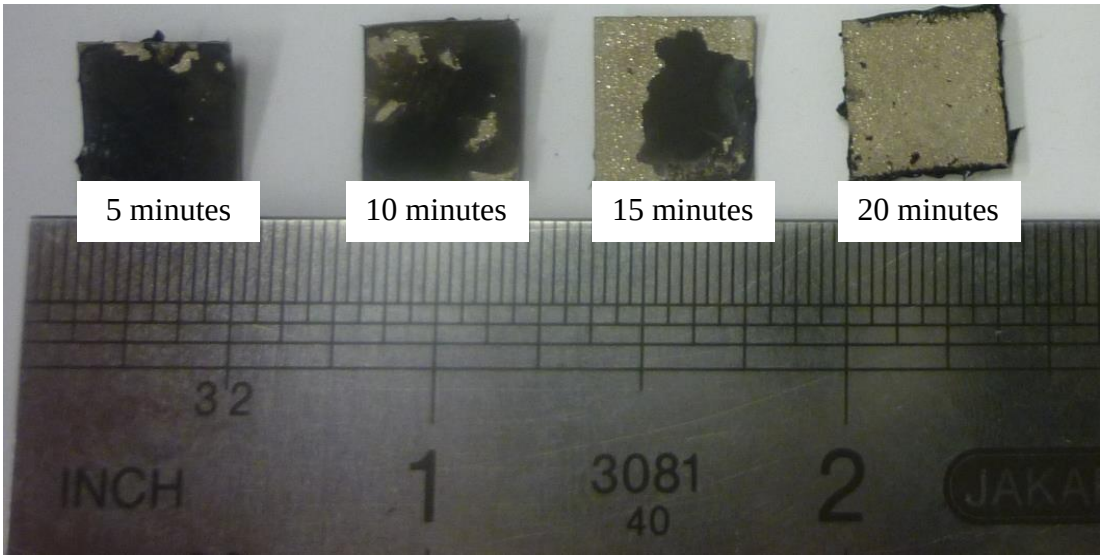

Figure 2-11 Effect of duration of oxygen evolution on the mechanical stability of catalyst films prepared with 18% PVDF binder; Potential held at 1 V vs. Hg/HgO in 1 M NaOH at room temperature

25% PVDF

At 25% PVDF the films surface appeared mechanically stable even after 30 minutes of cycling (see Figure 2-12). There was no visual difference in the behaviour of the stability of films when different binders were used or catalyst loadings greater than 1.5 mg cm^{-2} were employed.

Figure 2-12 Two electrodes prepared with 25% PVDF after 30 minutes of oxygen evolution; Potential held at 1 V vs. Hg/HgO in 1 M NaOH at room temperature

The results suggest that the stability of catalyst films is primarily due to the ratio of binder to catalyst employed. Thus all catalyst films, prepared by catalyst inks onto gold plated titanium electrodes for the half cell, included 25% PVDF binder.

2.5 Construction and arrangement of the anion exchange membrane polymer electrolyser cell

The anion exchange membrane polymer electrolyser (also known as the alkaline polymer electrolyser) cell set up is principally concerned with appropriate selection and preparation of the materials in the membrane electrode assembly. The main body of the electrolyser is constructed from a two pieces of titanium, one for the anode side and once for the cathode side. Titanium was selected as it allows for excellent electrical conductivity to the current collectors and it also acts as a strong support for the membrane electrode assembly. The two halves of the electrolyser are shown in Figure 2-13.

Figure 2-13 Photograph of the two halves of the unassembled polymer electrolyser cell

The ceramic plates and the insulated bolts mean that when the cell is pressed together (assembled) the electrical connection is only through the membrane electrode assembly. Figure 2-14 shows the main components for the MEA in the solid polymer electrolyser.

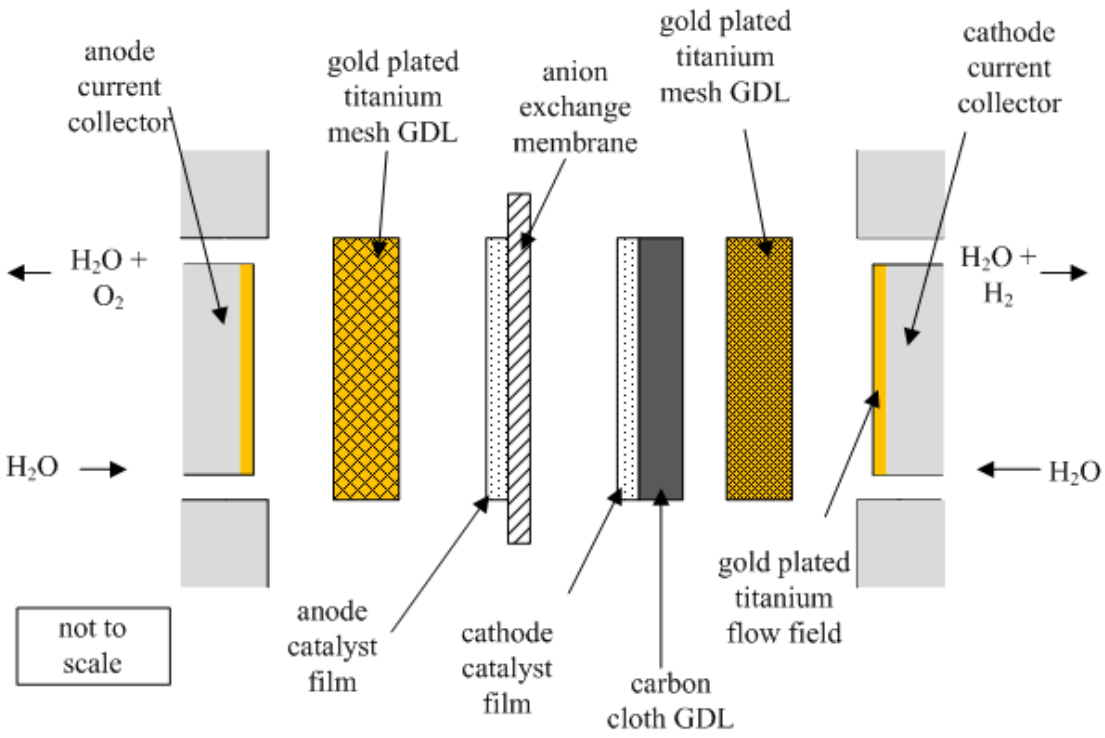

Figure 2-14 Cross sectional view of the main components of the MEA within the polymer electrolyser cell

A photograph of the flow field is shown in Figure 2-15. The three lower black holes represent the H_2O inlets that lead to the four vertical channels. At the top of the channels are three outlets which take away the product gas and remaining H_2O fuel.

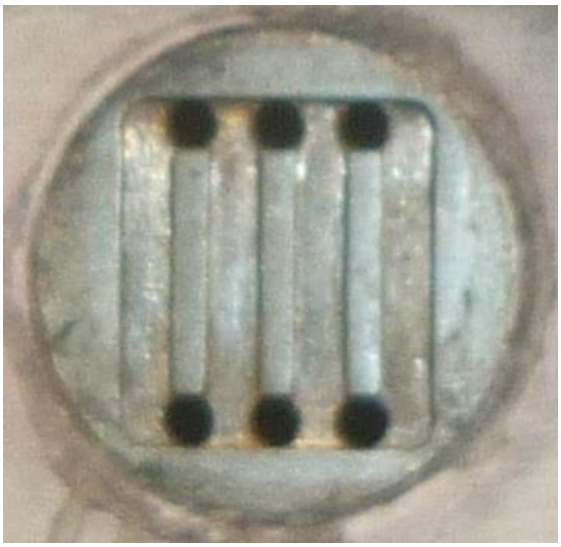

Figure 2-15 Flow field in the polymer electrolyser cell

These small vertical channels allowed for bubbles of the product gases to rise vertically up and out of the cell.

2.5.1 Preparation of the membrane electrode assembly

Carbon GDL was provided by Freudenberg Fuel Cell Components and utilised on the cathode side of the membrane electrode assembly. It provided the support for HER catalyst films and also allowed for diffusion of the product gasses away from the triple interface due to its high air permeability [89].

For the anode side gold plated titanium mesh was used as a GDL which provided both a strong electrode structure as well as the required continuous electrical contact between the current collector and the catalyst film. The reasons for the inclusion of gold within the set-up have been discussed in section 2.3.2.

The catalyst layers were applied directly to the GDL on the cathode side, or directly on the surface of the membrane itself by airbrushing freshly prepared catalyst inks. All spraying took place with pressurised and purified nitrogen gas. Further details on the composition of the inks is given in section 2.5.2. The substrates were held at 60°C to allow the solvent to evaporate. For all initial studies the cathode catalyst was fixed as a commercial platinum black, which was sprayed onto a Freudenberg GDL (H2315 C2) with a loading of 0.5 mg Pt cm^{-2}.

2.5.2 Ionomer

The half cell utilized PVDF as a binder that enabled the catalyst film to remain mechanically stable on the electrode surfaces. The mass used was 25% of the

catalyst's loading; however, this would not be suitable for use in the MEA of a polymer electrolyser due to the non-conductive properties of the PVDF.

To confirm this, an investigation was made to airbrush a catalyst film, containing NiO (commercial) and 25% PVDF binder, onto a membrane provided by Surrey University that has previously been utilised as a membrane in alkaline fuel cells [90]. Upon immersion of the membrane into a solution of electrolyte, for conversion to hydroxide form, the catalyst film would peel off the surface. The difference in the polymer electrolyte cell resistance with 25 wt% PVDF catalyst film included, and then removed, was in the region of 1.5 Ω.

The half cell contained 1 M NaOH electrolyte that increased conductivity in the catalyst layer as shown in Figure 2-6. In a solid polymer cell, an ionomer is required in the catalyst later to achieve the same effect. The ionomer of choice is PVBC (Poly vinyl benzyl chloride, sigma), which has been successfully used as an ionomer in previous alkaline water electrolyser and alkaline fuel cell studies. It requires amination before it can utilise its ion transport capabilities. Following a procedure for animation similar to work done by Varcoe et al [75] and Mamlouk et al [91] the catalyst film is submerged in undiluted NNN'N'-Tetramethyl-1,6-hexanediamene 99% (Acros Organics). Varcoe and Mamlouk selected this particular amination agent as it exhibits high thermal stability in alkaline solution [92]. Preparation of catalyst layers involved 35 wt% PVBC / PVC (ratio of 5:1) in the catalyst ink. The PVC was added to contribute to the adhesive properties required for the catalyst film to survive the harsh oxygen evolution conditions.

No hot pressing was performed, which is a similar to the practice of Varcoe et al [93]. This avoids damage of the membrane's quaternary ammonium groups at elevated temperatures that may affect the electrolyser performance due to a higher contact resistance between the membrane and electrodes. All spraying took place at 2 bar pressure with inert nitrogen gas atomising the catalyst ink out of the spray gun onto the substrate which was held at 60°C. Efficient spraying of the catalyst film onto the membrane was be achieved when the membrane was dehydrated.

Establishing the catalyst loadings was achieved in accordance with the procedure in the Appendix J.

3 Half cell results

3.1 Introduction

The aim of this chapter is to identify the most suitable non-noble catalysts for further assessment in the alkaline polymer electrolyser cell in Chapter 4. IrO_2 was chosen as a benchmark catalyst for performance for the oxygen evolution reaction. There is also a basic assessment of the activity of commercial NiO nanoparticles.

NiO was synthesized through thermal decomposition method (section 2.4.1), solution growth (section 2.4.2) and chemical bath deposition (section 2.4.3) methods described previously. Each of these methods involved thermally treating the NiO nanoparticles. The chemical bath deposition method is also responsible for the formation of a mix of nickel hydroxides, whose activity was investigated without any thermal treatment of the particles.

The binary transition metal catalyst $NiCo_2O_4$ is formed through thermal decomposition at temperatures of 280 and 300°C. The electrochemical characterization of these catalysts is given, with the studies conducted using the half cell described in section 2.3. Physical analysis through XRD was performed on the most promising catalysts to confirm their composition and particle size. The performance results of molybdenum and $NiMoO_4$ nanoparticles for the HER are given towards the end of this chapter.

3.2 Oxygen evolution reaction on IrO_2 catalyst

The noble metal catalyst, IrO_2 nanopowder, was used as a benchmark for investigations into electrocatalyst performance. Preparation of the IrO_2 catalyst layer on the electrodes surface was based on deposition of catalyst inks method described in section 2.4.6. A gold plated titanium electrode was prepared with a catalyst loading of 0.5 mg IrO_2 cm^{-2} (25% PVDF). For the counter electrode platinised titanium mesh was used. Cyclic voltammetry was performed on the electrode in the glass half cell electrolyser with 1 M NaOH electrolyte, prepared from 97% purity NaOH pellets (Sigma Aldrich) and pure DI water. Figure 3-1 shows the 7 cycles that were performed between 0.2 and 0.8 V vs. Hg/HgO before stability was achieved.

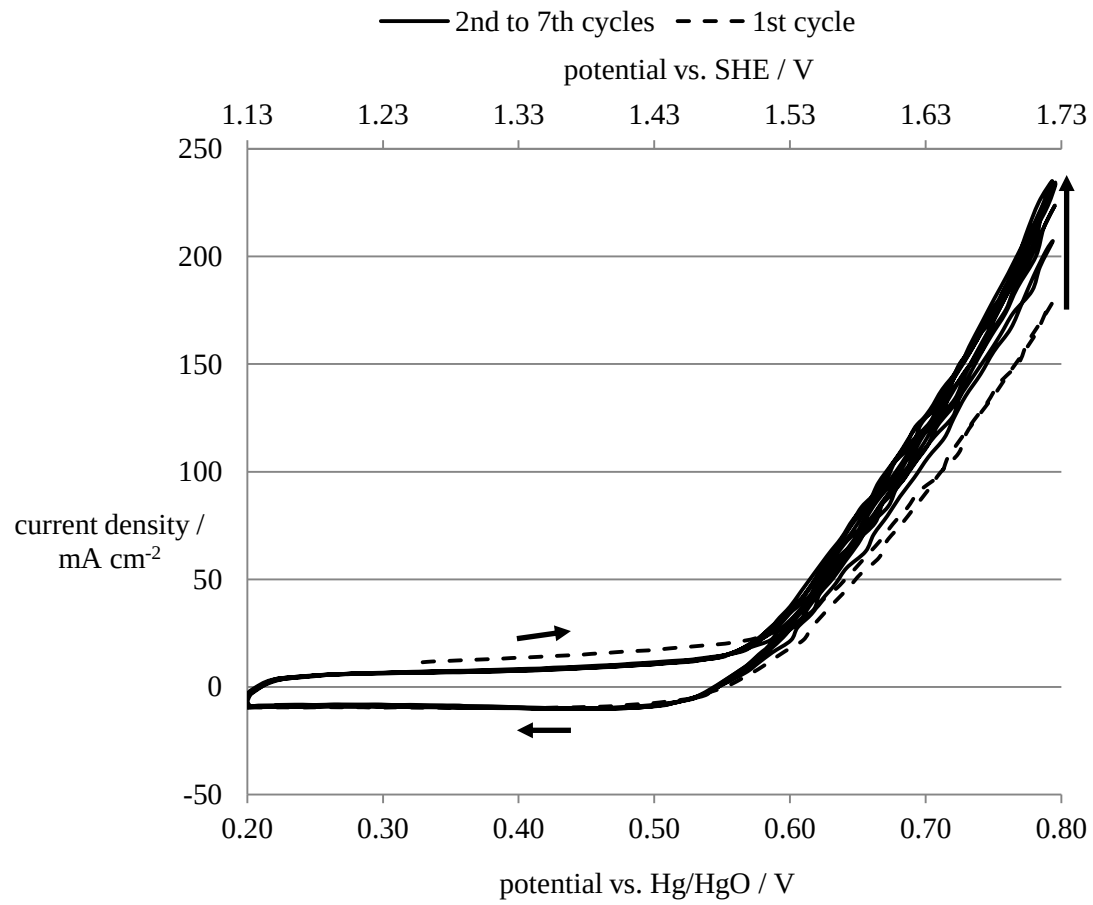

Figure 3-1 Voltammogram of an IrO_2 catalyst film deposited onto a gold plated titanium electrode, in an electrolyte of 1 M NaOH at a temperature of 25°C, and a scan rate of 30 mV s^{-1}

The small arrows indicate the direction of the scan that, in the positive going potential sweep between 0.20 and 0.55 V vs. Hg/HgO, shows evidence of a large double layer capacitance in the oxidation region before it curves upwards due to oxygen evolution. The double layer capacitance, or charging, of the IrO_2 catalyst layer is associated with diffusion of protons and reaction with the oxide within the coating according to the following mechanism [94]:

$$IrO_x(OH)_y + \delta H^+ + \delta e^- \leftrightarrow IrO_{x-\delta}(OH)_{y+\delta} \qquad \textbf{Equation 3-1}$$

The large arrow indicates that with progressive cycling, there was a minor shift in this curve towards lower overpotentials, due to an increase in electrocatalytic activity on the surface of the electrodes. Previous studies on this catalyst do not indicate this shift [95] [39] so it could be caused through desorption of impurities from the catalyst film's surface, which would lead an increase in active surface area available for ionic transfer to take place. These impurities could be sourced from materials used in the preparation of the electrode or from the electrolyte solution in the half cell.

Figure 3-2 shows the steady state current response of the IrO_2 electrode, between the same potential range as the linear sweeps and at a scan rate of 0.5 mV s^{-1}. Measurements were made at electrolyte temperatures of 25, 40 and 60°C.

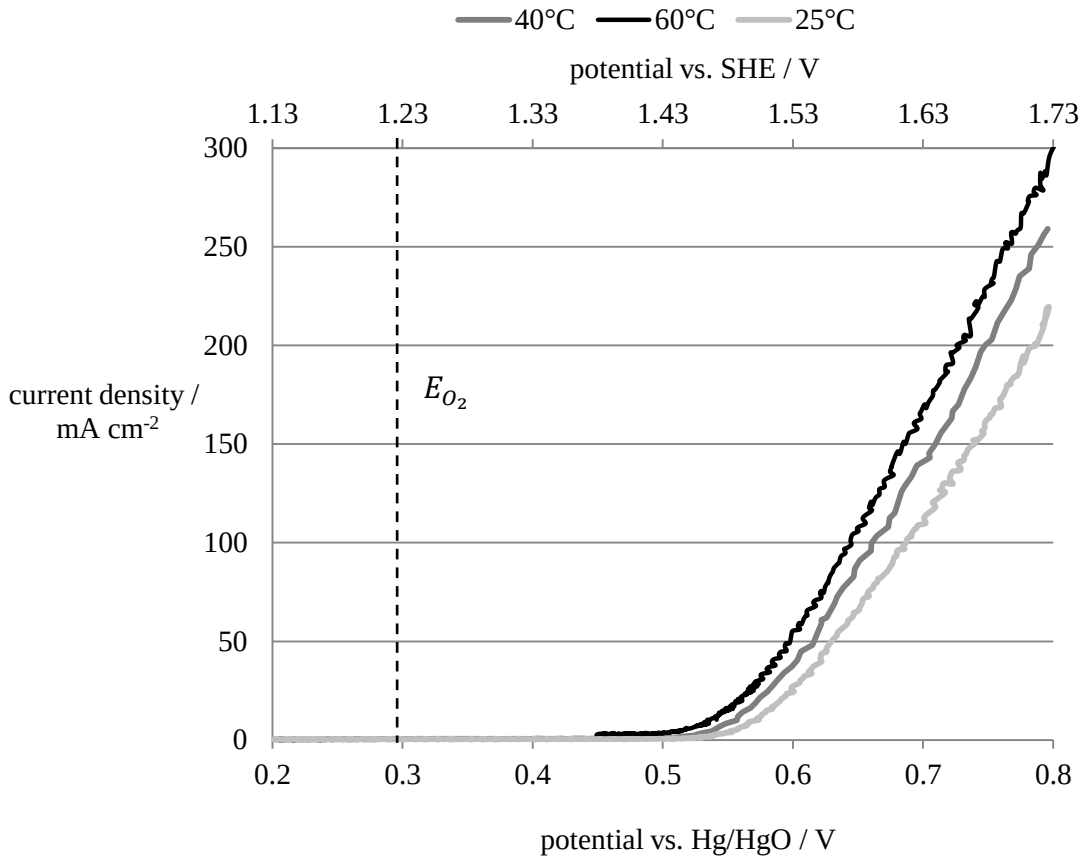

Figure 3-2 The anodic steady state current response of an IrO_2 catalyst film deposited onto a gold plated titanium electrode, in an electrolyte of 1 M NaOH at temperatures of 25, 40 and 60°C and with a scan rate of 0.5 mV s^{-1}

The dashed line indicates the theoretical onset potential (E_{O_2}) for oxygen evolution at 25°C thus, all potentials to the right of this line are considered as overpotentials. There was no obvious activity until the onset potential for oxygen evolution at 0.51 V vs. Hg/HgO. When the temperature of the electrolyte (1 M NaOH) was increased to 40 and 60°C, the curve in Figure 3-2 shifts towards lower overpotentials. This is due to an increase in conductivity of OH^-ions, which is a function of temperature and this reduced the ohmic resistance in the electrolyte. The resulting current densities produced at 0.8 V vs. Hg/HgO are 219, 256 and 300 mA cm^{-2} for 25, 40 and 60°C, respectively. There was no sign of transport hindrance up to 300 mA cm^{-2}.

The values obtained from the CV in Figure 3-2 can serve a benchmark in this investigation. As a comparison to other systems, performances reported in the literature include a previous study of IrO_2 as an anode catalyst in an alkaline polymer electrolyser by Leng et al [40]. They used 2.9 mg IrO_2 cm^{-2} on the anode and with pure water at 50°C they achieved 0.3 A cm^{-2} at a potential of 1.72 V, whereas Rasten [95] achieved 1 A cm^{-2} at 1.6 V.

For a Tafel plot, the log_{10}values of the current density, j, were plotted against the overpotential, μ, calculated from Equation 2-4, for 25, 40 and 60°C. For the IrO_2 catalyst this is shown in Figure 3-3.

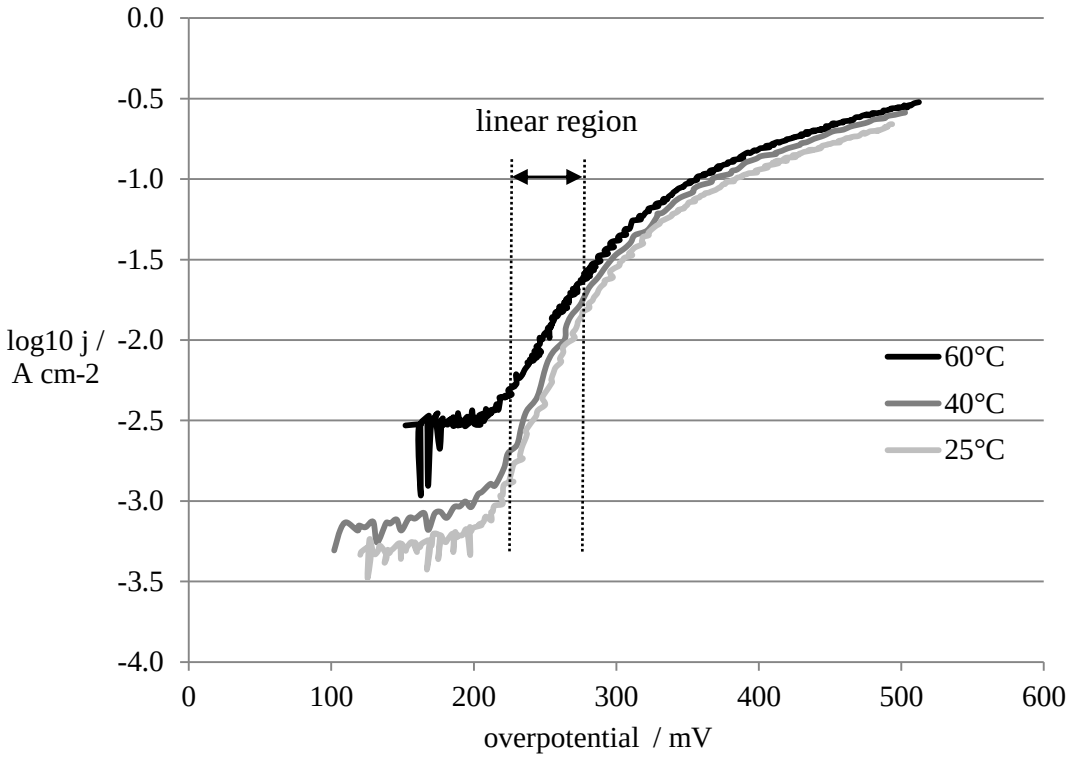

Figure 3-3 Tafel lines for IrO_2 electrode in an electrolyte of 1 M NaOH at temperatures of 25, 40 and 60°C

The Tafel plots show linearity between overpotentials of approximately 225 to 275 mV, which corresponds to slopes of 51, 53 and 69 mV dec^{-1} for 25, 40 and 60°C, respectively. At higher overpotentials there is a non-linear relationship as gradual uncompensated ohmic losses occur on the electrode's surface. These losses can be attributed to higher quantities of gas being formed, which results in more bubbles on

the surface of the electrode. The bubbles interfere with the reactions described in Equation 1-4 and Equation 1-5, which results in a reduction in mass transport and reduced rate of reactions. The linear relationship is only for one decade of current density, which, according to Rasten [95] is insufficient to determine real Tafel behaviour.

Other IrO_2 electrodes utilising the same electrolyte (1 M NaOH, 25°C) from published research report lower values. For example, Guerrini [96] reported slopes between 40 and 45 mV dec^{-1}. Since the value for the Tafel slope is sensitive to the structure of the electrode's surface, a cause for this lower Tafel value could be the temperature of the thermal treatment used on the IrO_2 during preparation of the catalyst. Higher thermal treatment is known to increase crystal growth and could also be connected to oxidation states of the catalyst. The increase in Tafel slopes values, with the increase in annealing temperature employed in the preparation of the catalyst, might be explained by the increasing stability of the metal-oxygen bond. This increasing stability could increase the activation energy, leading to a change in the charge transfer coefficient α, and thereby changing the Tafel slope values [95].

The exchange current densities, j_0, of the electrode were found by extrapolating the linear section of the Tafel plot to intercept the $log\ j$ axis. The j values at this intercept are equal to 5.1 x 10^{-3}, 1.0 x 10^{-3} and 0.7 x 10^{-3} A cm^{-2} for 25, 40 and 60°C respectively. As a comparison, Figure 3-4 shows the steady state current density responses of an electrode with the IrO_2 catalyst film and a nickel foil electrode with the same conditions applied.

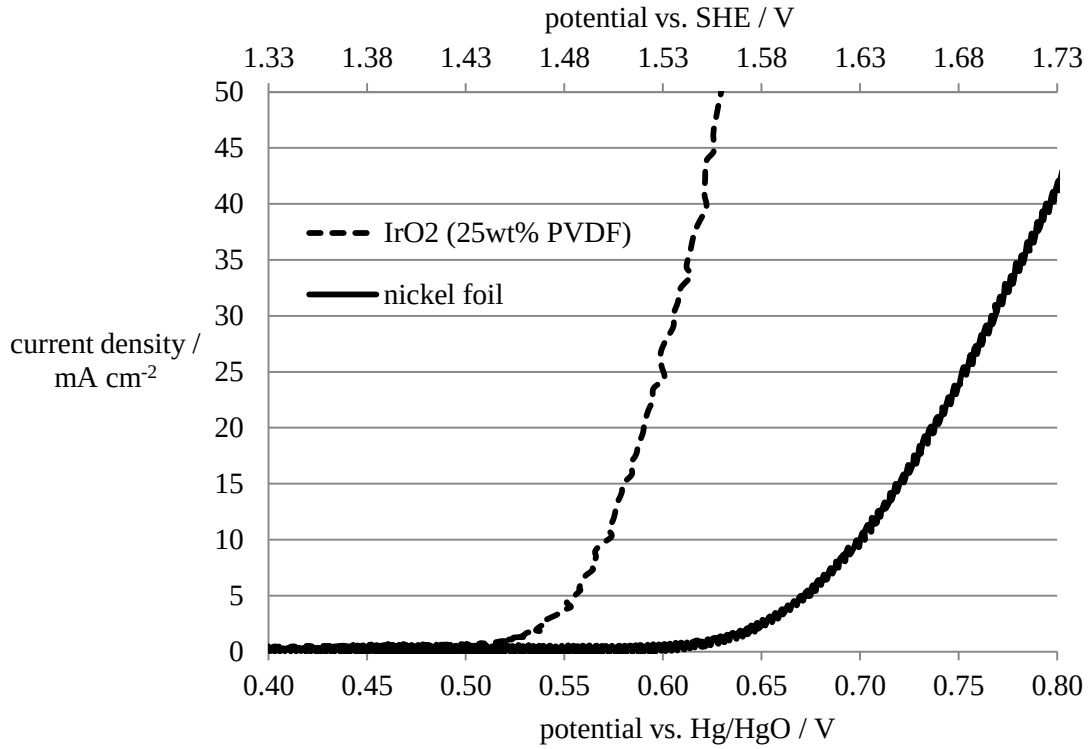

Figure 3-4 Voltammogram comparing the performance of an IrO_2 catalyst film deposited onto a gold plated titanium electrode with 25 wt% PVDF, and a nickel foil electrode in a glass half cell electrolyser, with an electrolyte of 1 M NaOH at a temperature of 25°C and a scan rate of 0.5 mV s^{-1}

For the nickel foil electrode, there was no noticeable activity until at the potential for the onset of the OER, which occurred at 0.63 V vs. Hg/HgO. This corresponds to an extra 220 mV of overpotential compared to the onset for OER of the IrO_2 electrode.

3.3 Oxygen evolution reaction on commercial NiO catalyst

NiO nanoparticles, with an average particle size of 50 nm (Sigma Aldrich), were prepared into a catalyst ink that contained 25 wt% of PVDF binder and the NMP solvent discussed in section 2.4.6. The ink was deposited onto square shaped gold plated titanium foils, with a surface area of 1 cm^2, on a hot plate at a temperature of 60°C that allowed the solvent to evaporate. To give a profile of how the loading of catalyst affected the performance of the electrolyser, 8 electrodes were prepared in this way with loadings between 0.3 and 3.6 mg NiO (commercial) cm^{-2}. Cyclic voltammetry was performed on each electrode in the glass half cell electrolyser with 1 M NaOH as the electrolyte, prepared from 97%+ purity NaOH pellets (provided by Sigma Aldrich). Figure 3-5 shows the polarisation scans of the electrode prepared with a loading of 1.2 mg cm^{-2}.

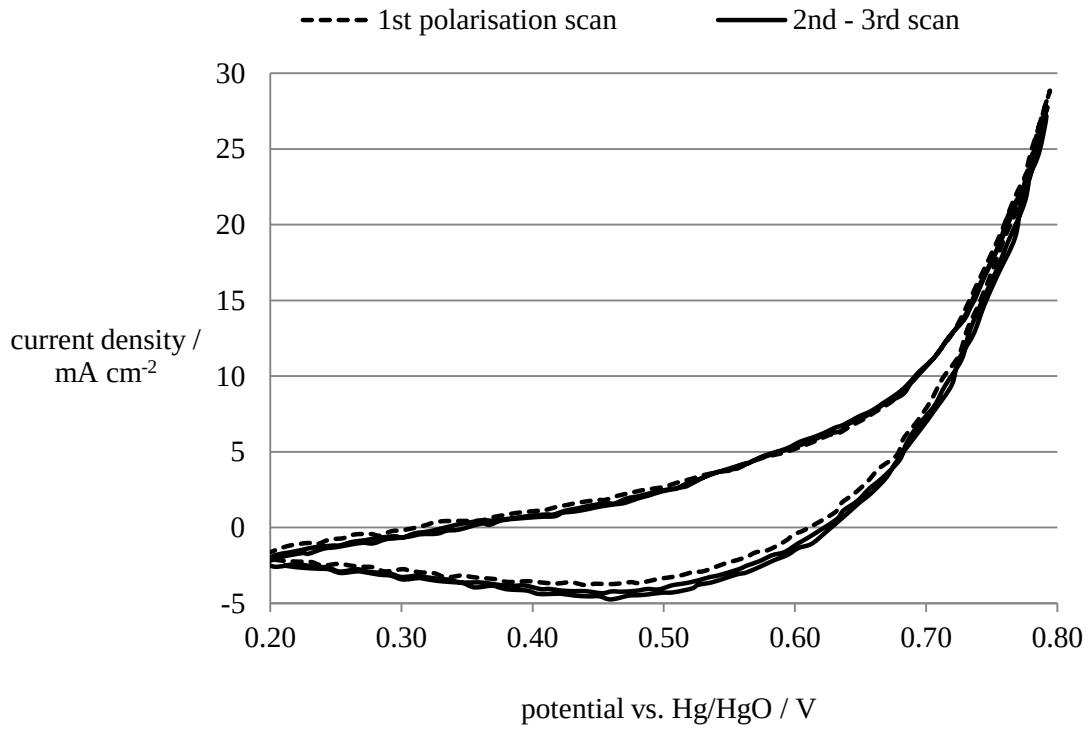

Figure 3-5 Polarisation curves for a NiO (commercial) catalyst film deposited onto a gold plated titanium electrode, with a catalyst loading of 1.2 mg cm^{-2} and 25% PVDF, in an electrolyte of 1 M NaOH at a temperature of 25°C, and a scan rate of 30 mV s^{-1}

The three cycles show good reproducibility over the potential range of 0.2 and 0.8 V vs. Hg/HgO. The activity in the oxidation and reduction regions can be attributed to Ni(II) / Ni(III) redox couple, the reactions of which are discussed later in section 3.6.

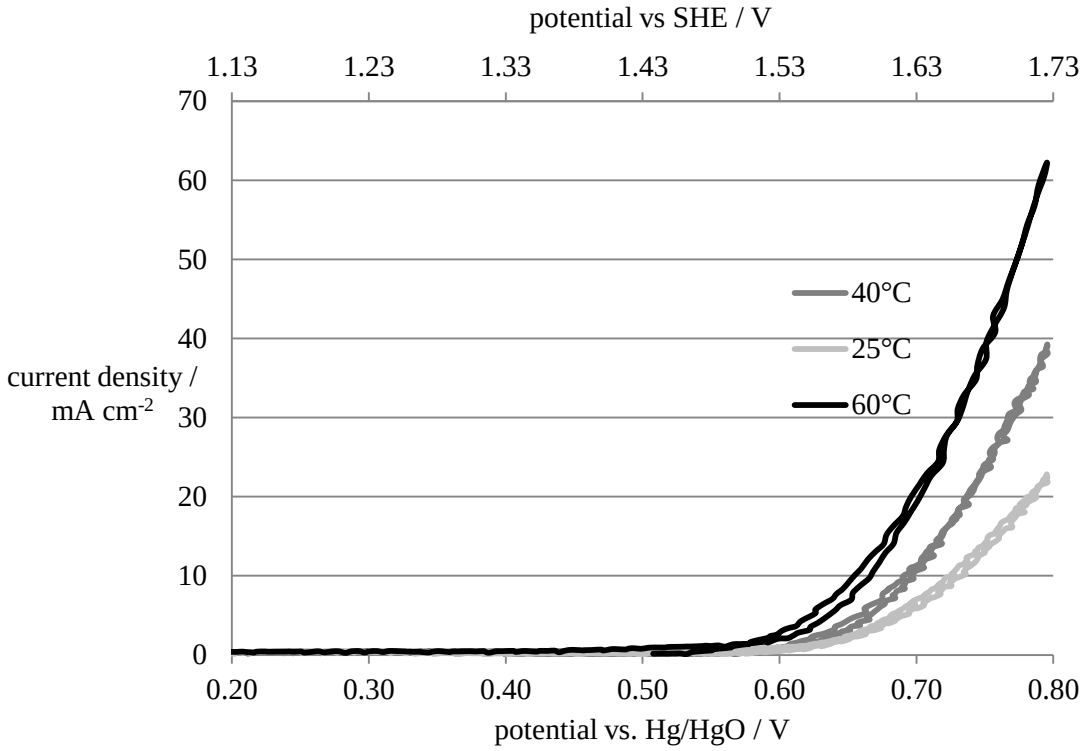

Figure 3-6 Voltammogram showing the temperature effect of the electrolyte (1 M NaOH) on the current response of an electrode with a loading of 1.2 mg cm^{-2} NiO (commercial) and at scan rates of 0.5 mV s^{-1}

The steady state current response density values were measured against steady state scans at 0.8 V vs. Hg/HgO and plotted against the catalyst loading as shown in Figure 3-7.

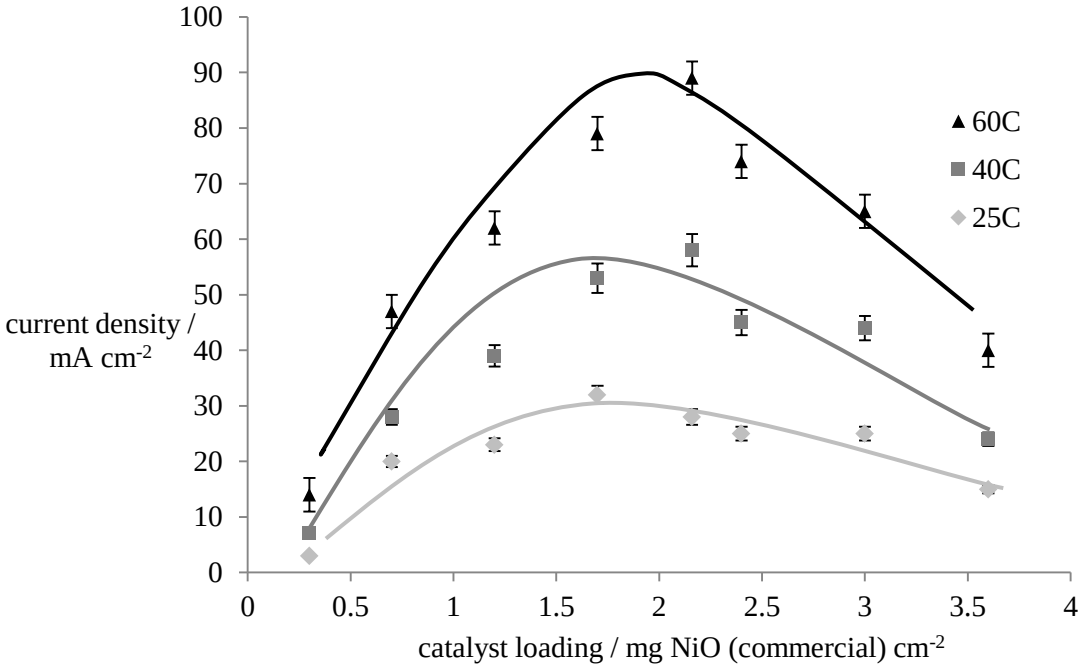

Figure 3-7 Effect of NiO (commercial) catalyst loading and temperature of the electrolyte (1 M NaOH) on the electrode's performance, taken at potentials of 0.8 V vs. Hg/HgO

It is clear that the current density values are affected by the loading of catalyst deposited onto the electrode. Changes in the loading altered the active surface area of the catalyst that is exposed to the electrolyte. The active surface area of the NiO (commercial) appears to be the primary factor affecting the current density values at a given temperature.

The three curves in Figure 3-7 represent best fit curves for the relationship between the loading of NiO (commercial) and the performance, in terms of current density, at the three different electrolyte temperatures of 25, 40 and 60°C. The curves show that the performance increased with catalyst loading, up to an optimum value of approximately 2.0 mg NiO (commercial) cm^{-2}, then decreased steadily in performance with higher loadings. Increasing the temperature of the electrolyte also has an effect on the current density. This is presumably because as the temperature of the electrolyte is increased the conductivity of the OH^- ions is also increased, making ionic, and thus mass, transfer easier.

The corresponding current density values, taken at 0.8 V vs. Hg/HgO, were 32, 58 and 90 mA cm^{-2} for 25, 40 and 60°C, respectively. It can be suggested that deviation from the best fit curves occurs through non-homogenous distribution of catalyst, due to the method of deposition utilised, and agglomeration of particles. It appears that current density values show less deviation from the best fit curves at low (<1.5 mg) and high (>2.5 mg) loadings than compared to the mid-range.

Figure 3-8 shows the variance in Tafel slope values of NiO (commercial) catalyst films compared with the IrO_2 benchmark catalyst tested previously in section 3.2.

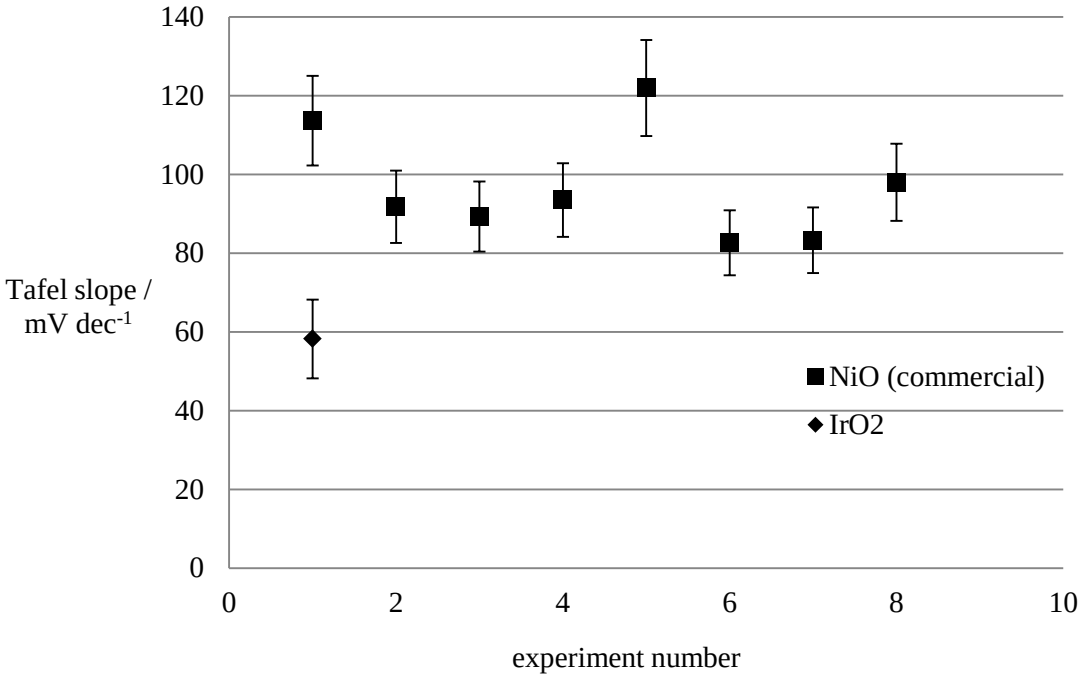

Figure 3-8 Tafel slopes of NiO (commercial) and IrO_2 electrodes

The chart indicates that the Tafel slopes for IrO_2 (48 - 68 mV dec^{-1}) and the commercial NiO (78 - 135 mV dec^{-1}) both span a broad range of values. The performance of NiO is dependent on the many factors discussed in section 1.7 including the crystal structure and particle sizes. These are determined primarily by the synthesis method, so investigation followed into various synthesis methods for NiO, in an attempt to reduce particle size and determine the resulting electrochemical behaviour.

3.4 Performances of NiO prepared by thermal decomposition

3.4.1 NiO prepared by thermal decomposition of nickel nitrate

Investigation was made into OER activity of titanium mesh electrodes coated with a NiO catalyst film. The titanium mesh electrodes were pretreated according to the procedures in 2.3.5 then prepared through the dip coat method, followed by thermal decomposition previously described in section 2.4.1.

Electrodes were prepared with various loadings to give a profile of the catalyst loading versus the performance (current density) of the electrodes. Figure 3-9 shows the relationship between the steady state current density of NiO electrodes prepared by thermal decomposition of nickel nitrate salts at temperatures of 400°C and 450°C.

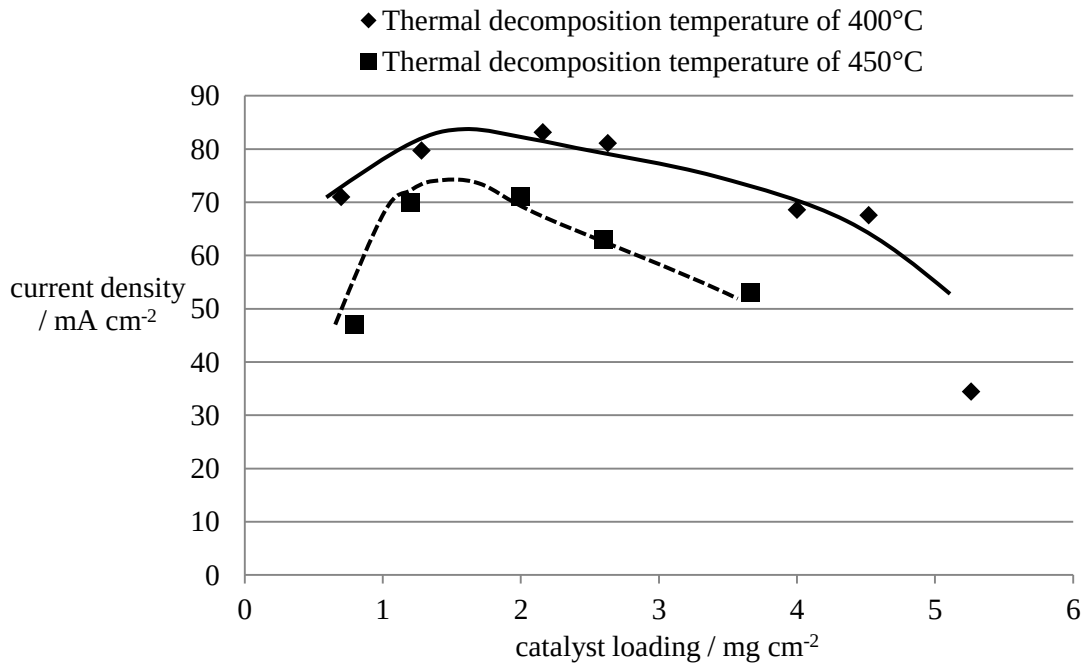

Figure 3-9 Effect of the final decomposition temperature on the current density of NiO (400) and NiO (450) catalyst films prepared by dip coat followed by thermal decomposition method; in an electrolyte of 1 M NaOH at a temperature of 25°C and a potential of 0.8 V vs. Hg/HgO

The curves represent the best fit relationship between the catalyst loading and the resulting steady state current density values taken at a potential of 0.8 V vs. Hg/HgO. They show that increasing the decomposition temperature of the nickel nitrate salt decreases the current density of the electrodes of NiO. Thermally decomposing $Ni(NO_3)_2$ at 400°C produced an optimum current density of approximately 82 mA cm^{-2} whilst thermally decomposing at 450°C produced approximately 74 mA cm^{-2}.

This increase in performance of almost 10% could be related to the particle size, which is governed by the final decomposition temperature. It is believed that the higher treatment temperatures lead to a more compact crystalline nickel oxide, through agglomeration of crystals and thus larger particle sizes. This decreases the active area of the catalyst with respect to their mass. An alternative method of thermal decomposition of nickel nitrate salts mixed with urea 1.7.2 will now be discussed.

3.4.2 NiO prepared by solution growth with urea followed by thermal decomposition

Particles of NiO (urea) were synthesized according to the procedure in section 2.4.2. Gold plated titanium electrodes were prepared with various loadings of a NiO (urea) catalyst film containing a binder of 25 wt% PVDF. Cyclic voltammetry was performed by cycling electrodes in the glass half cell electrolyser, between 0.2 and 0.8 V vs. Hg/HgO in a 1 M NaOH electrolyte at 25°C, until stable voltammograms were established. Figure 3-10 shows the voltammogram for an electrode prepared with 1.1 mg cm^{-2} of NiO (urea).

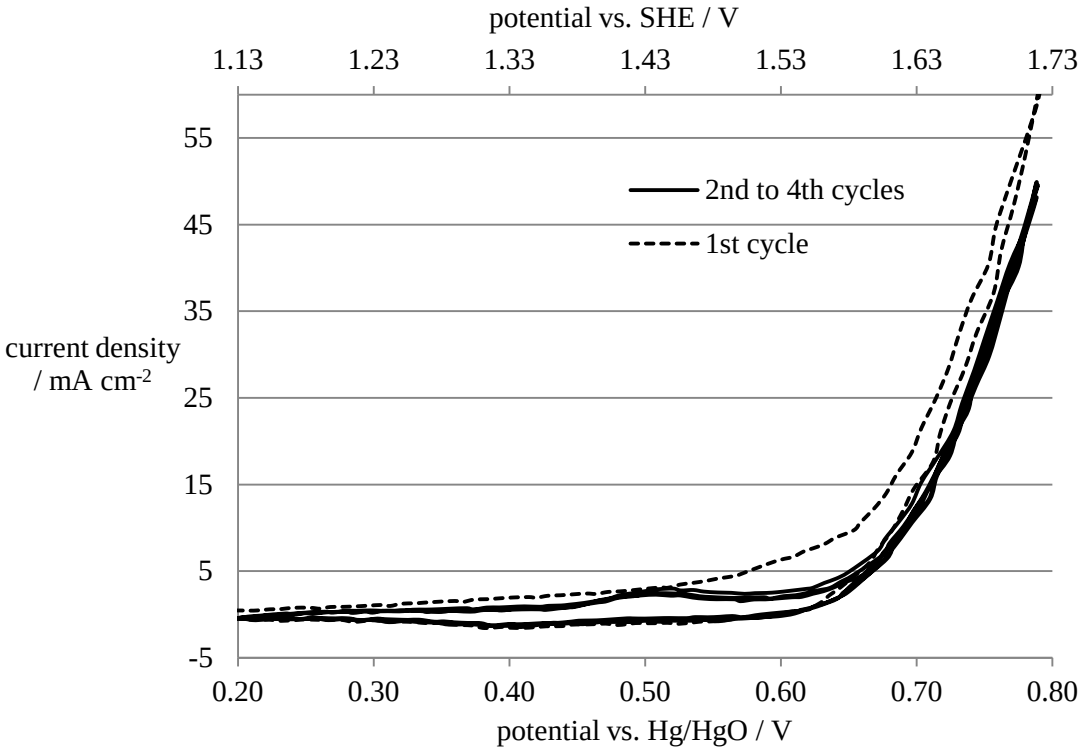

Figure 3-10 Voltammogram for NiO (urea) catalyst film on a gold plated titanium electrode with 25% PVDF, in an electrolyte of 1 M NaOH at a temperature of 25°C, and a scan rate of 30 mV s^{-1}

The polarisation cycles resemble the behaviour of the commercial NiO already reported in Figure 3-5 except the anodic and cathodic peaks are more defined in this case.

The steady state current response of the electrode was made from conducting a CV scan within the same potential range and at a scan rate of 0.5 mV s^{-1}. This was repeated for electrolyte temperatures of 40 and 60°C and the result is shown in Figure 3-11.

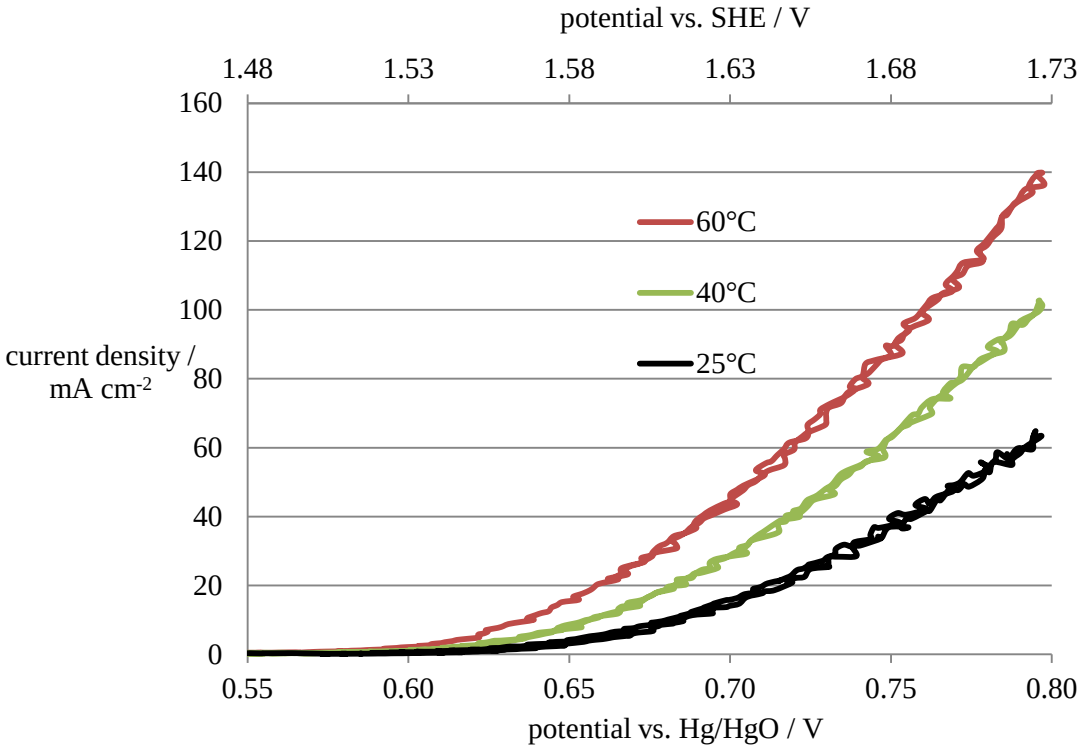

Figure 3-11 Temperature effect of the 1 M NaOH electrolyte on the steady state current response of a NiO (urea) catalyst film, with 25% PVDF on a gold plated titanium electrode, with a catalyst loading of 1.1 mg cm^{-2} and scan rate of 0.5 mV s^{-1}

The chart shows that increasing the temperature of the 1 M NaOH electrolyte caused a decrease in ohmic resistance in the catalyst layer and thus the current density has increased. The onset potential for electrodes containing the NiO (urea) catalyst is 0.60 V vs. Hg/HgO.

Figure 3-12 shows the relationship between the catalyst loading and the steady state current density values at 0.8 V vs. Hg/HgO.

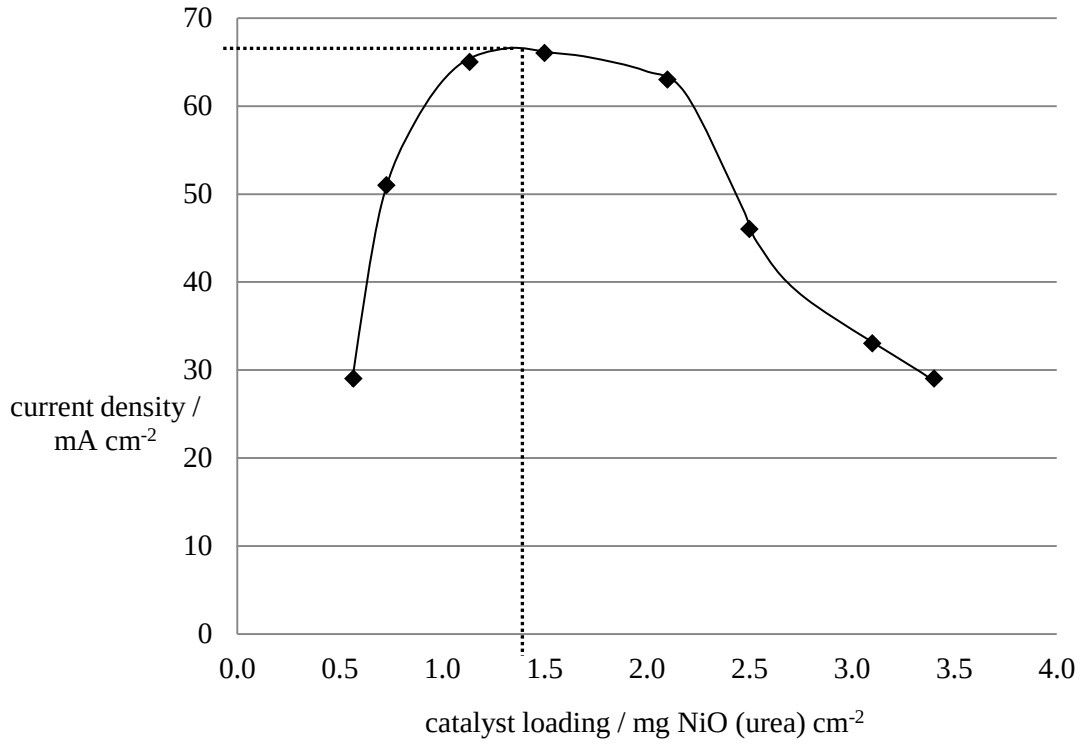

Figure 3-12 Effect of NiO (urea) catalyst film loading on the current density values of the electrodes taken at a potential of 0.8 V vs. Hg/HgO, in an electrolyte of 1 M NaOH at a temperature of 25°C

The relationship shows a sharp increase in the performance (current density) of the electrode in relation to the loading of NiO (urea) catalyst. An optimum value of 66 mA cm^{-2} is reached with a corresponding catalyst loading of 1.4 mg cm^{-2}.

Figure 3-13 compares the current densities reported in Figure 3-12 against the current densities produced by electrodes containing a catalyst film of NiO synthesized by the decomposition methods shown in section 2.4.1 and section 2.4.2.

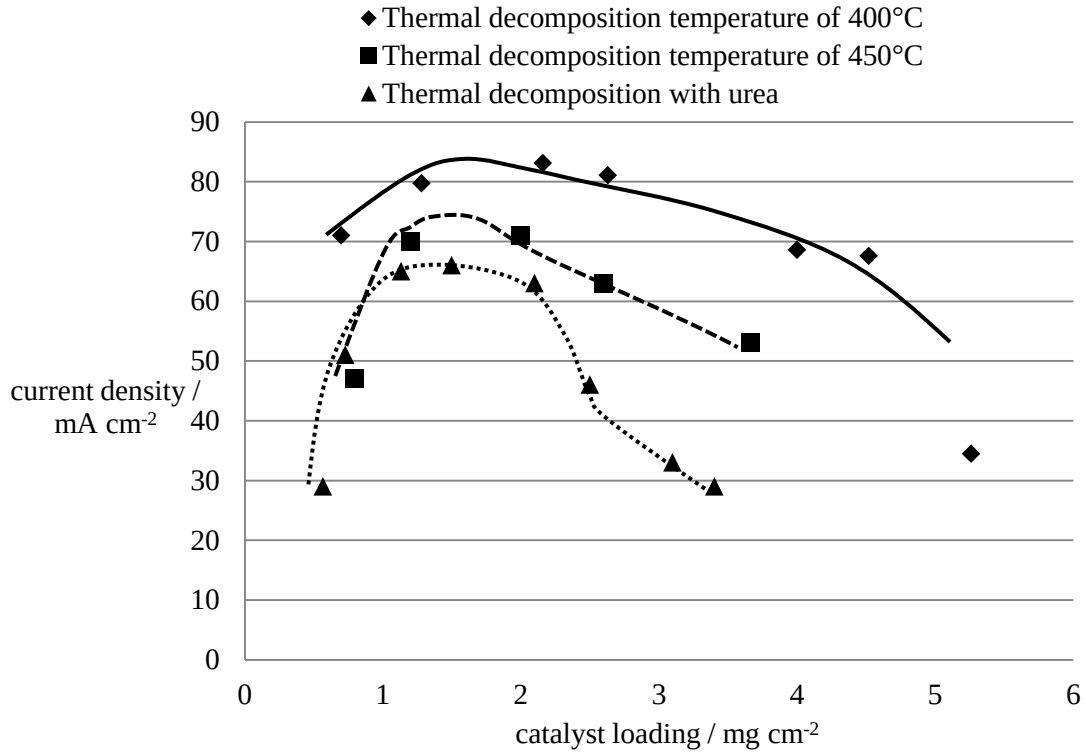

Figure 3-13 Effect of the synthesis procedure and loading of catalyst on the current density values taken at a potential of 0.8 V vs. Hg/HgO in an electrolyte of 1 M NaOH at a temperature of 25°C

The difference in the three best fit lines show that the maximum current density produced is clearly dependent on the preparation procedure of the NiO catalyst films. Table 3-1 shows the maximum current density for the catalysts reported so far in section 3.3 and section 3.4 in 1 M NaOH at 25°C.

Table 3-1 Maximum current densities achieved by NiO (commercial), NiO (400°C), NiO (450°C) and NiO (urea) catalyst films in the glass half cell electrolyser at a cell potential of 0.8 V vs. Hg/HgO, and an electrolyte of 1 M NaOH at a temperature of 25°C

Catalyst name	Current density / mA cm^{-2}
NiO (commercial)	36
NiO (400°C)	84
NiO (450°C)	75
NiO (urea)	66

Interestingly, the optimum loading for all the catalysts in Table 3-1 is approximately 1.5 mg cm^{-2}. The mass of catalyst deposited will influence the thickness of the catalyst film. Consequently, and due to the similarity in the particles, a restriction of the catalyst's current density is the conductivity of the catalyst film.

Higher catalyst loadings were achieved in electrodes prepared by the thermal decomposition of nickel nitrate salts (section 3.4.1) than compared to electrodes prepared with catalyst inks that contained the commercial NiO (section 3.3) and NiO synthesized by solution growth with urea (section 3.4.2). This is because the method for thermal decomposition of nickel nitrate salts required the use of mesh structured electrodes (for reasons discussed in 2.4.1) that the catalyst film has a greater ability to adhere to than to the flat foil substrate.

This difference in electrode geometry makes it difficult to accurately compare the performance of catalyst films tested on the mesh to those tested on the foil. It can be suggested that a more appropriate form of comparison would have been to prepare the NiO (400) and NiO (450) catalyst films firstly as a nanopowder, then deposit them onto gold plated titanium electrodes with the same binder that the other catalysts, NiO (urea) and NiO (commercial), experienced. Nevertheless the NiO (urea) particles were tested under same conditions as NiO (commercial) and their performance was superior.

The range of improvement of the activity of NiO through thermal decomposition methods appears to be limited. The results from an alternative synthesis method called chemical bath deposition will now be shown.

3.5 Synthesis of catalysts by chemical bath deposition

Titanium foil electrodes were pretreated according to the procedure in section 2.3.5 and the catalyst deposition method according to section 2.4.3 immediately followed. The relationship between the time the electrode spent in the chemical bath, and the change in mass of the electrode, is shown in Figure 3-14. The change in mass of the electrode directly corresponds to the mass of film deposited onto the surface of the electrode. Due to the resolution of the microbalance, experimental error makes it difficult to ascertain the exact change in mass of the electrode at low measurements (< 1.0 mg), thus error bars have been added accordingly.

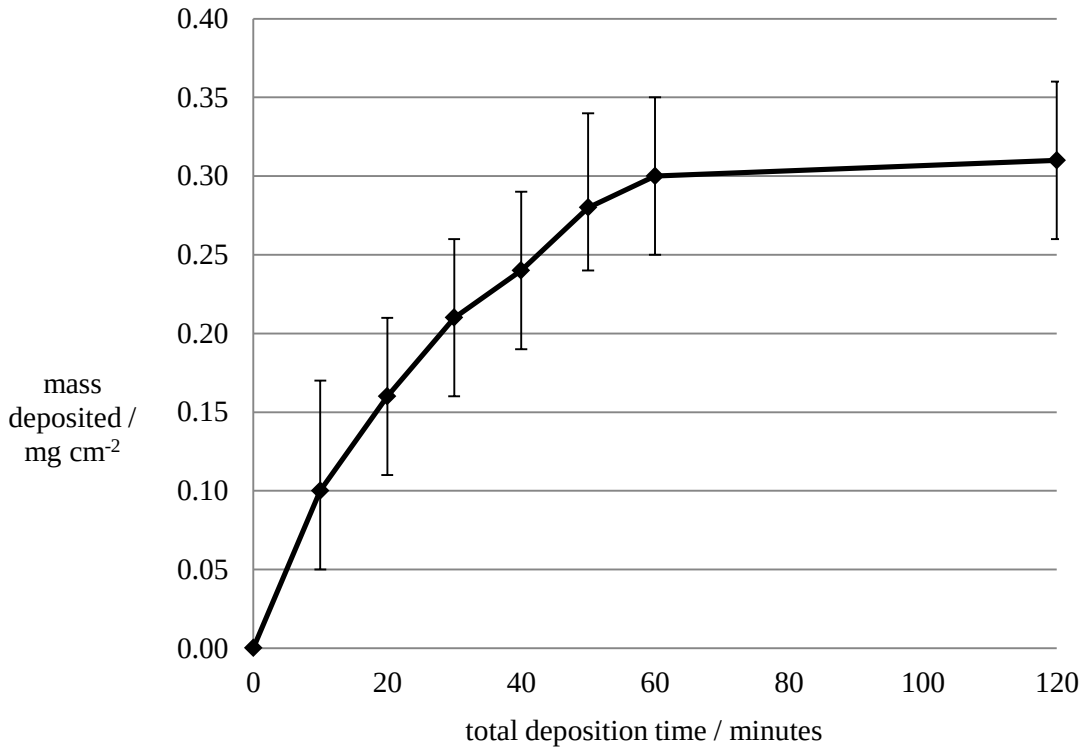

Figure 3-14 Effect of time the titanium substrate spends in the chemical bath and the resulting mass of film deposited

The growth follows that of previous work indicated in Figure 1-11. There is initially a linear growth regime as the growth increases proportionately with deposition time. After 30 minutes the film enters a depletion growth regime as the film growth rate drops quickly and approaches a limited film thickness.

There appears to be discrepancies as to the composition of the film within research literature. In 1990, Pramanik [44] originally suggested the following reaction mechanism for the film formation of NiO.

$$NiSO_4 + xK_2S_2O_8 + 2(1+x)OH^- \rightarrow NiO_{1+x} + xK_2SO_4 + (1+x)SO_4^{2-} + (1+x)H_2O$$ **Equation 3-2**

$$NiO_{1+x} + \frac{2x}{3}NH_3 \rightarrow NiO + \frac{x}{3}N_2 + H_2O$$ **Equation 3-3**

Pramanik explains that the first stage (in Equation 3-2) involves the deposition of higher valency nickel oxide (mixed valency 2 and 3). In Equation 3-3 the higher valent compound is reduced by ammonia to the normal oxidation state. However later work by Bukovec [87] in 1993 identified the deposited material as $4Ni(OH)_2 \bullet NiOOH \bullet 5.78H_2O$ through XRD analysis. They ascertained that there are also unidentified peaks in the XRD pattern which were ascribed to as then unknown nickel oxides. Their samples dried at 85°C showed main peaks corresponding to $Ni_3O_2(OH)_4 \bullet 1.53\ H_2O$ as well as unidentified compounds. In 2006 Han et al. [64] reported through XRD analysis that the deposited material contained α-$Ni(OH)_2$ and $4Ni(OH)_2 \cdot NiOOH \cdot xH_2O$. Other work by Xia et al. [63] [97] in 2008 reports the as-deposited film to contain β-$Ni(OH)_2$ (JCPDS 14-0117) and γ-NiOOH (JCPDS 06-0075).

The divergence in the nickel hydroxides formed could be due to the slight difference in operating parameters employed for their procedures. These operating parameters could include variations in volume and shape of the vessel, which would influence any stirring conditions or natural mixing from convection of the heated particles. Differences in the source of heating supply, e.g. a hot plate or heating jacket, would influence the heat distribution of the chemical bath and thermal hot-spots may exist.

Furthermore, any variations in the separation and/or purification of the particles, formed after they have been removed from the bath, could alter the structures and composition of the compounds.

The literature suggests that the particulates formed contain nickel hydroxides, which according to the literature review in section 1.6 are known to be catalytically active towards the oxygen evolution reaction. Literature concentrates its efforts towards the production of NiO via thermal treatment of these nickel hydroxides into NiO. There is no evidence of a study into the oxygen evolution reaction activity of the particles produced by CBD and not thermally treated at high temperatures so the particles synthesized through section 2.4.3 will be studied further.

To confirm the composition of the deposited particles and their particle size, the particulates were retained from bath, air dried and analysed by XRD and previous SEM studies from literature.

3.5.1 Analysis of particulates formed in the chemical bath

Particulates formed from the chemical bath deposition procedure (section 2.4.3) had their XRD data collected using an Xpert-Pro diffractometer and analysed with Xpert Data Viewer and OriginPro. Data was cross referenced against Joint Committee on Powder Diffraction Standards (JCPDS). A chart of the diffraction patterns that were produced from the particulates is shown in Figure 3-15.

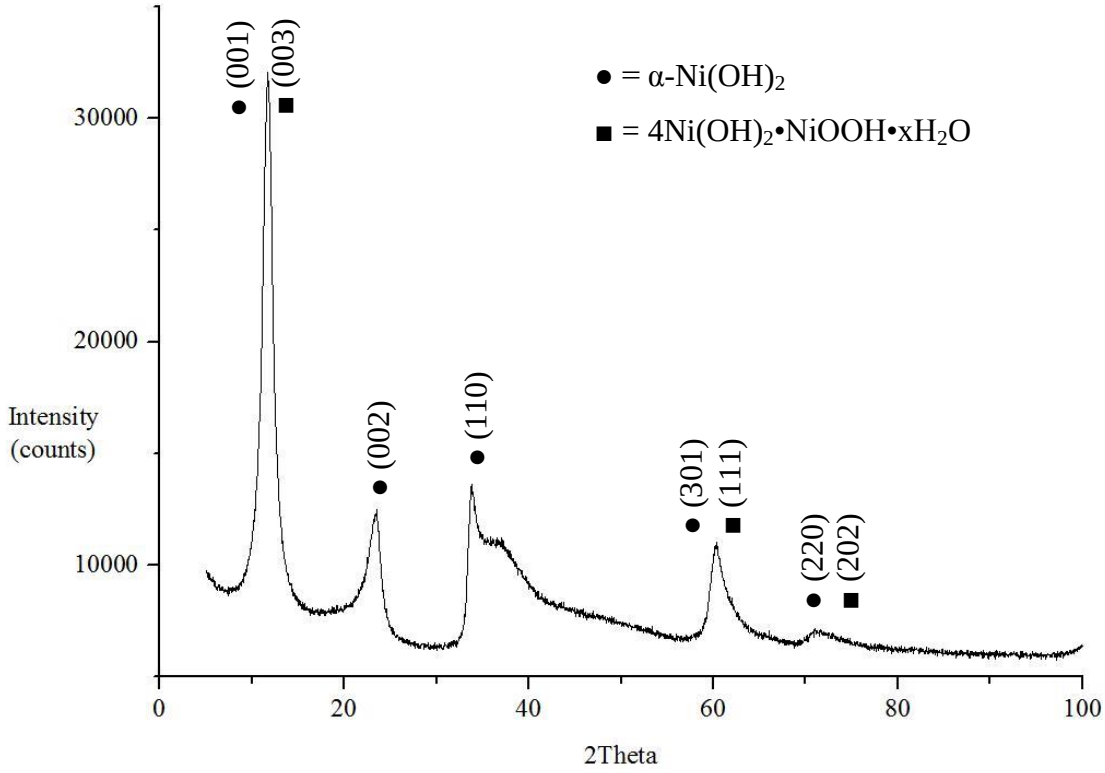

Figure 3-15 X-ray diffraction patterns of the particles formed from the chemical bath deposition method

The diffraction patterns of the particulates show main peaks at 2θ values of 11.6, 23.5, 33.8, 36.8, 60.3 and 71.5, which correspond to α-$Ni(OH)_2$ (JCPDS 00-022-0444 [$3Ni(OH)_2•2H_2O$]) and $4Ni(OH)_2•NiOOH•xH_2O$ (JCPDS 00-006-0044). The XRD data also shows traces of additional complex nickel hydroxide compounds, which are shown in Table 3-2.

Table 3-2 Trace nickel hydroxide compounds formed from the chemical bath deposition method

Compound name	Compound formula	Corresponding peaks, 2θ	Source (JCPDS)
Nickel hydroxide hydrate	$Ni(OH)_2 \bullet 0.75H_2O$	11.4, 22.7, 38.7	00-038-0715
Nickel hydroxide	$Ni(OH)_2$	19.2, 38.6, 52.1	01-073-1520
Oxonium nickel hydroxide	$(H_3O)_2NiO_2$	13.3, 37.9, 43.4	01-073-2408
Nickel hydroxide methoxide	$Ni[(OH)_{0.66}(OCH_3)_{0.33}]_2$	11.8, 34.1, 38.9	00-030-1835
Jamborite	Ni_3O_6	11.4, 22.9, 39.0	96-901-2317

These compounds are in very small amounts but exemplify the divergence of the reaction mechanisms taking place in the bath. The carbon containing compound, nickel hydroxide methoxide, is most likely present due to the chemical bath solution absorbing carbon dioxide from the air during the process, or forming due to any organic impurities present in the starting compounds. The XRD results from this research most agrees with Han [64], who also reported the particles to contain α-$Ni(OH)_2$ and $4Ni(OH_2) \bullet NiOOH \bullet xH_2O$.

Using the peak at a 2θ value of 11.6 the particle size was calculated from the Scherrer formula in Appendix H to be 58 nm.

There is an absence of peaks corresponding to NiO and this proves that some sources, included a book by Hodes [98], incorrectly reference the reaction mechanism reported by Pramanik [44] that refers to the deposited film to contain NiO. The research by Han [64], includes an SEM image of the deposited film and this is shown in Figure 3-16.

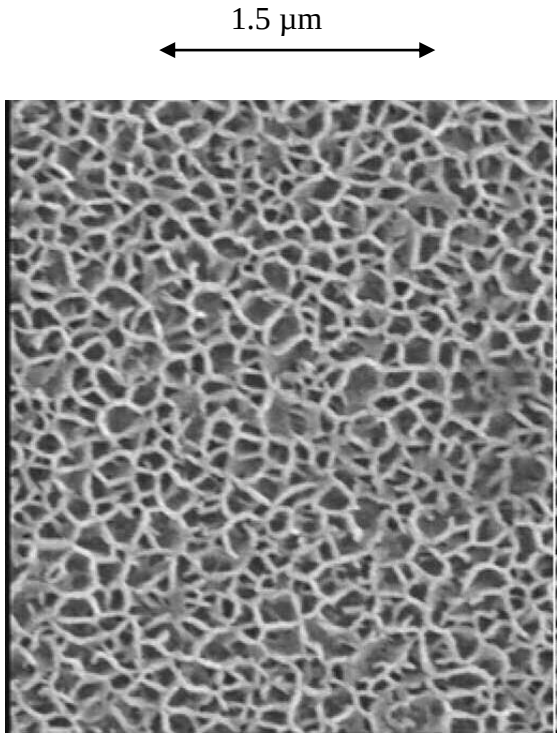

Figure 3-16 SEM image produced by Han [64] showing the structure of the deposited film from the chemical bath deposition procedure

Figure 3-17.shows an SEM images produced by Xia [97] (who reported the film to contain the different nickel hydroxides of β-$Ni(OH)_2$ and γ-NiOOH) both before and after thermal treatment (see section 3.5.2 for further analysis of particulates after further treatment).

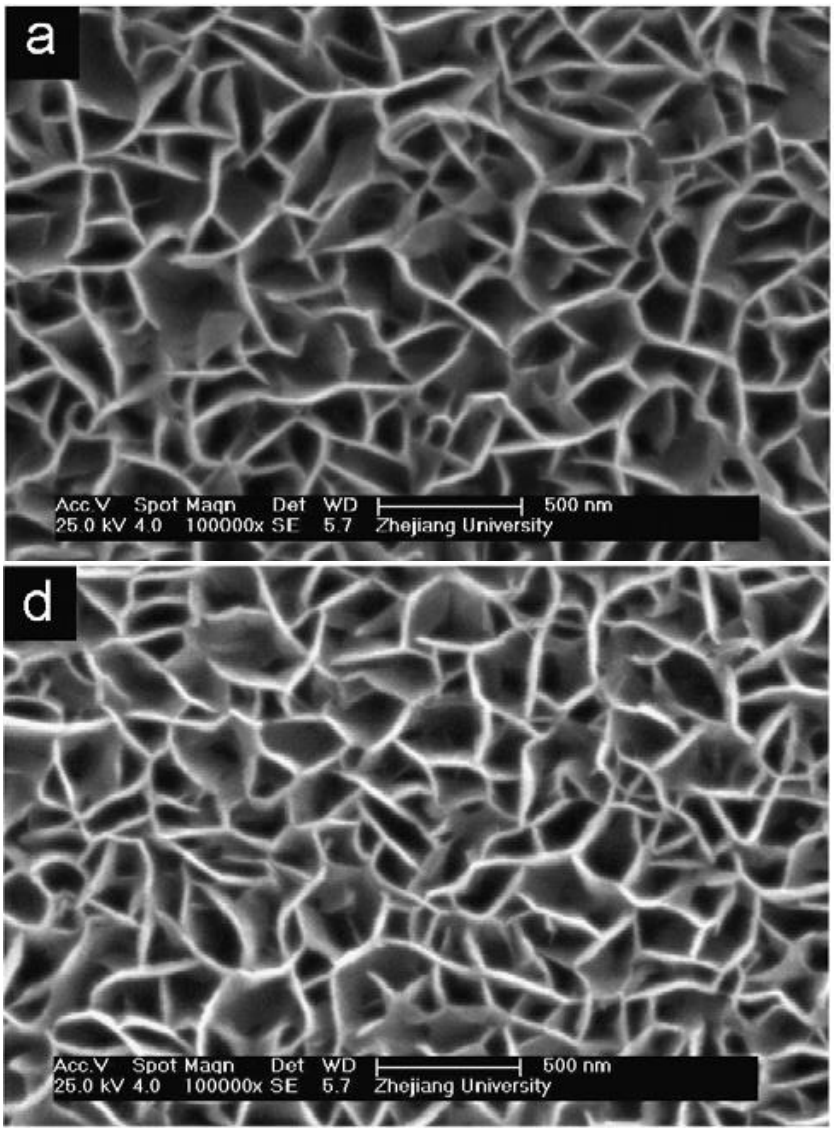

Figure 3-17 Top view SEM images produced by Xia [97] of the catalyst film as deposited (a) and after annealment at 400°C for 1 hour (d)

Regardless of the slight differences in nickel hydroxides detected by researchers in the deposited film, it is clear that the CBD procedure is synonymous with producing a highly porous film of interconnecting flakes. According to the SEM images in Figure 3-16 and Figure 3-17 the pore sizes appear to have diameters in the range of 20 – 300 nm. The thickness of these flakes is approximately 20 nm – 50 nm.

This analysis has identified the particulates to contain a blend of nickel hydroxide material. Yet previous literature does not seem to investigate performance of this film with regards to the oxygen evolution reaction. Particulates collected from the

chemical bath deposition procedure, and not thermally treated, were tested for activity towards the oxygen evolution reaction in section 3.6.3.

3.5.2 Analysis of particulates after thermal treatment

The particulates formed from the CBD procedure were placed in a furnace and calcined at 400°C for one hour. The resulting powder was analysed by XRD in the same manner as section 3.5.1. The result of this calcination procedure is shown in the XRD chart in Figure 3-18.

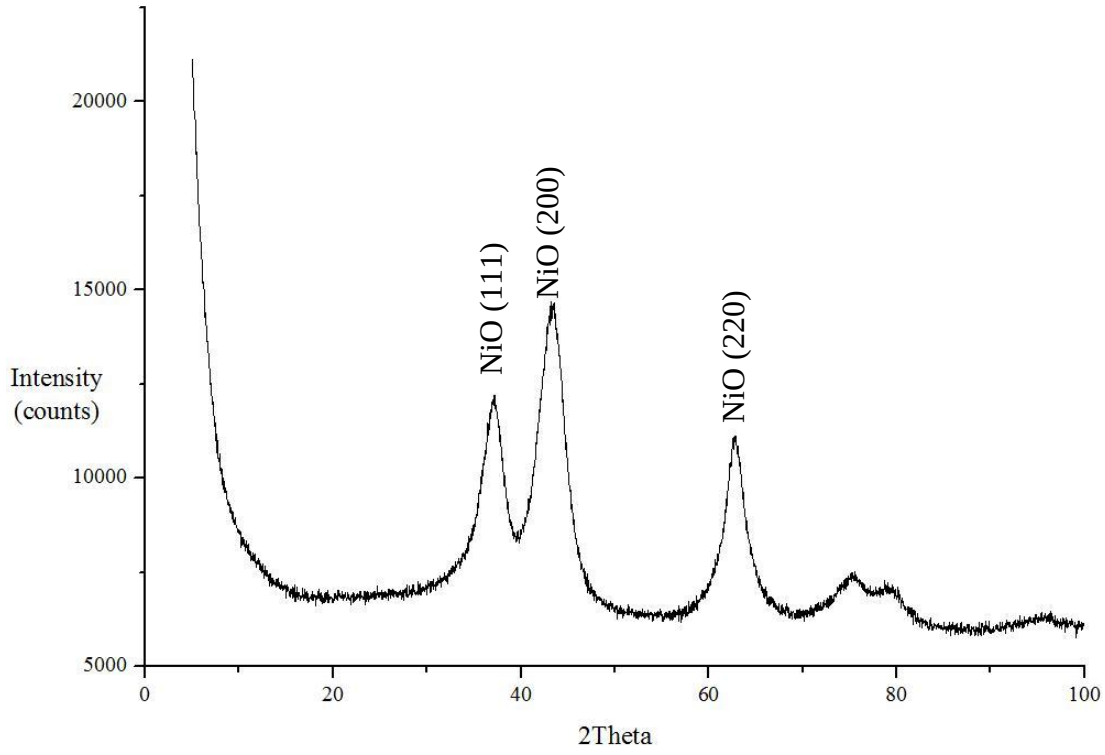

Figure 3-18 XRD patterns of NiO particles synthesized through chemical bath deposition followed by thermal treatment at 400°C

There is a stark contrast between the peaks in Figure 3-15 and the peaks in Figure 3-18. This contrast indicates that particles have been transformed. The major peaks in Figure 3-18 are at 2θ values of 37.0 (111), 43.2 (200) and 62.8 (220), which corresponds to cubic NiO (JCPDS 00-047-1049). The peaks correspond to previous

work by Han [64] (37.3 and 43.3), Xia [62] (37.2, 43.3 and 62.8) and Huang [99] (37.3, 43.3, and 62.9) and Cai [100] 37.2, 43.3 and 62.9. The particle size was calculated according to the Scherrer formula in Appendix H as 30 nm.

The XRD analysis has identified two catalyst materials:

1. α-$Ni(OH)_2$ / $4Ni(OH)_2 \bullet NiOOH \bullet xH_2O$ – particles which were formed in the initial film formation
2. NiO – particles which were formed after thermal treatment of the film at 400°C for 1 hour

The electrochemical performances of these two catalyst materials will now be reported.

3.6 Electrochemical studies on catalysts synthesized by the chemical bath deposition method

3.6.1 Oxygen evolution reaction on NiO catalyst film prepared by chemical bath deposition method

Cyclic voltammetry was performed on electrodes prepared in the chemical bath for 10, 20 30, 40, 50, 60 and 120 minutes. Figure 3-19 shows the current density response between 0 and 0.8 V vs. Hg/HgO from a NiO film formed after remaining in the bath for 30 minutes.

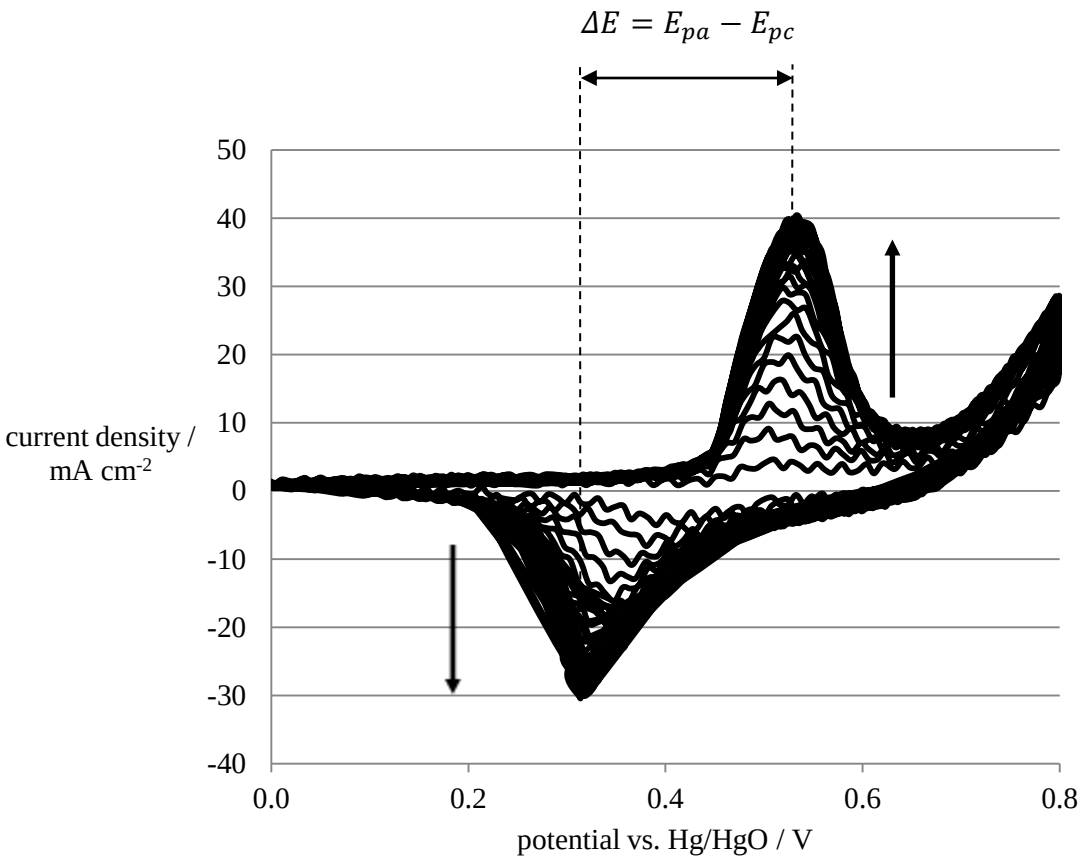

Figure 3-19 Growth in anodic and cathodic peaks of a NiO (CBD) catalyst film formed after 30 minutes in the chemical bath on a titanium electrode; in an electrolyte of 1 M NaOH at a temperature of 25°C and a scan rate of 50 mV s^{-1}

The voltammogram indicates an anodic peak appearing before the oxygen evolution reaction takes place. The potential for the anodic peak, E_{pa}, shifts from 0.51 V vs. Hg/HgO from the first cycle to 0.53 V vs. Hg/HgO for the 29th cycle. The cathodic peak, E_{pc}, shifts from 0.40 to 0.32 V. Xia [97] wrongly attributes the anodic, or oxidation, peak to the following electrochemical reactions described in Equation 3-4 and Equation 3-5:

$$NiO + OH^- \leftrightarrow NiOOH + e^- \quad \textbf{Equation 3-4}$$

$$NiO + H_2O \leftrightarrow NiOOH + H_2 + e^- \quad \textbf{Equation 3-5}$$

The cathodic peak is attributed to the following reactions described in Equation 3-6 and Equation 3-7:

$$Ni(OH)_2 \leftrightarrow NiOOH + H_2 + e^- \quad \textbf{Equation 3-6}$$

$$Ni(OH)_2 + OH^- \leftrightarrow NiOOH + H_2O + e^- \quad \textbf{Equation 3-7}$$

It is highly unlikely that the hydrogen gas is being produced in Equation 3-5 and Equation 3-6 in these positive potentials. Alternatively, it can be said that the reactions taking place follow the Bode scheme described previously in Figure 1-9. Thus the anodic peak can be attributed to the oxidation of Ni(II) to Ni(III), whilst the cathodic peak is attributed to reduction of Ni(III) to Ni(II), meaning that Equation 3-4 and Equation 3-7 are valid.

The potential difference between the anodic and cathode peaks is 0.1 V in the first cycle and 0.2 V in the final cycle. The shift is small and the data is noisy but the extra potential required shows the surface redox reactions are becoming more difficult and less reversible. There is also an increase in anodic and cathodic peak current with each cycle, indicating an increase in electrochemical activity from the NiO film.

The surface area underneath these peaks corresponds to capacitance of the material, or charge, and it is directly proportional to the number of electrochemically reactive surface sites. Integration of the voltammetric curve gives the peak area, which is directly proportional to the voltammetric charge. The relationship between the peak areas, $|j|$, and the voltammetric charge, q*, is shown in Equation 3-8.

$$q^* = \int_E^E \frac{|j|}{\upsilon} dE \qquad \textbf{Equation 3-8}$$

Table 3-3 shows the potential values for E_{pa}, E_{pc} and ΔE, along with the integral areas of the peaks (taken from the final cyclic voltammogram) of the electrodes prepared for different length of times in the chemical bath.

Table 3-3 Anodic and cathodic peak potentials, and the resulting peak areas in relation to electrode preparation time in the chemical bath

preparation time of electrode in the chemical bath / minutes	E_{pa} / V	E_{pc} / V	ΔE / V	Integral area under the curve
10	0.52	0.33	0.19	1.69944
20	0.54	0.32	0.20	2.81088
30	0.53	0.32	0.21	4.76537
40	0.52	0.31	0.21	4.44833
50	0.51	0.32	0.19	4.89166
60	0.53	0.30	0.23	5.73622
120	0.59	0.25	0.24	7.39439

For catalyst film preparation time periods up to 50 minutes, the anodic and cathodic peak potentials appear to remain at 0.524 V +/- 0.014 V. The difference in peak potentials, ΔE, for the same time period up to 50 minutes also remain constant at 0.205 V +/- 0.015 V. This proves that the ratio of oxidised species to reduced species was stable. Peak current densities, and the resulting integral area under the peak's curve, increase with longer film formation times. This shows that increasing the preparation time of the catalyst film affected the amount of electrochemically active material in the film.

At preparation times of 60 minutes and more it appears as though the anodic peak potential shifts to more positive potentials, whilst the cathodic peak potentials shifts to more negative potentials and peak surface areas continue to rise. The effect of the length of preparation time in the chemical bath on the resulting steady state current density of the electrodes is shown in Figure 3-20.

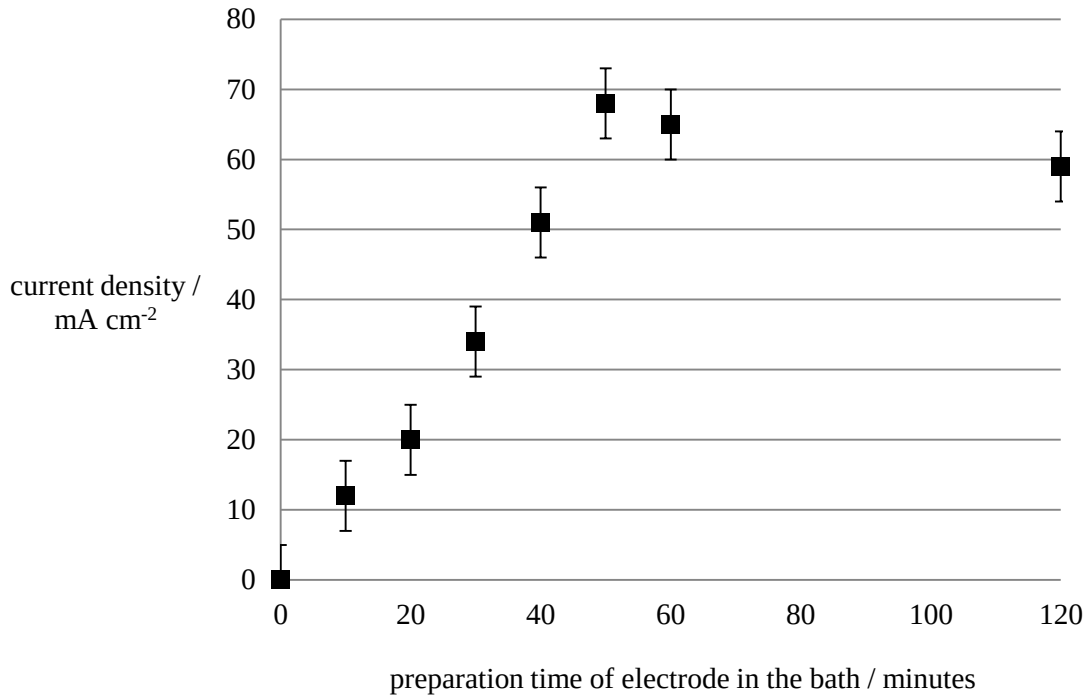

Figure 3-20 Relationship between the steady state current density of a titanium electrode with a NiO (CBD film) catalyst film taken at a potential of 0.8 V vs. Hg/HgO, and the preparation time the electrode spent in the chemical bath, with an electrolyte of 1 M NaOH at a temperature of 25°C

The highest current density was achieved from NiO films that had formed in the bath for 50 minutes. The current density reduced slightly for catalyst films formed for deposition times of 60 minutes or longer. This drop is only slight, and could be within experimental error; however, the evidence points towards an optimum film thickness being attained after 50 minutes in the bath. Longer deposition times could be reducing the porosity of the film. This would increase the mass of the film but decrease the active surface area exposed to the electrolyte. Pore reduction could affect the mass transport as gas bubbles being formed at high current densities may become trapped on the surface of the film. The relationship between the steady state current density values and the area under the anodic peak is shown in Figure 3-21.

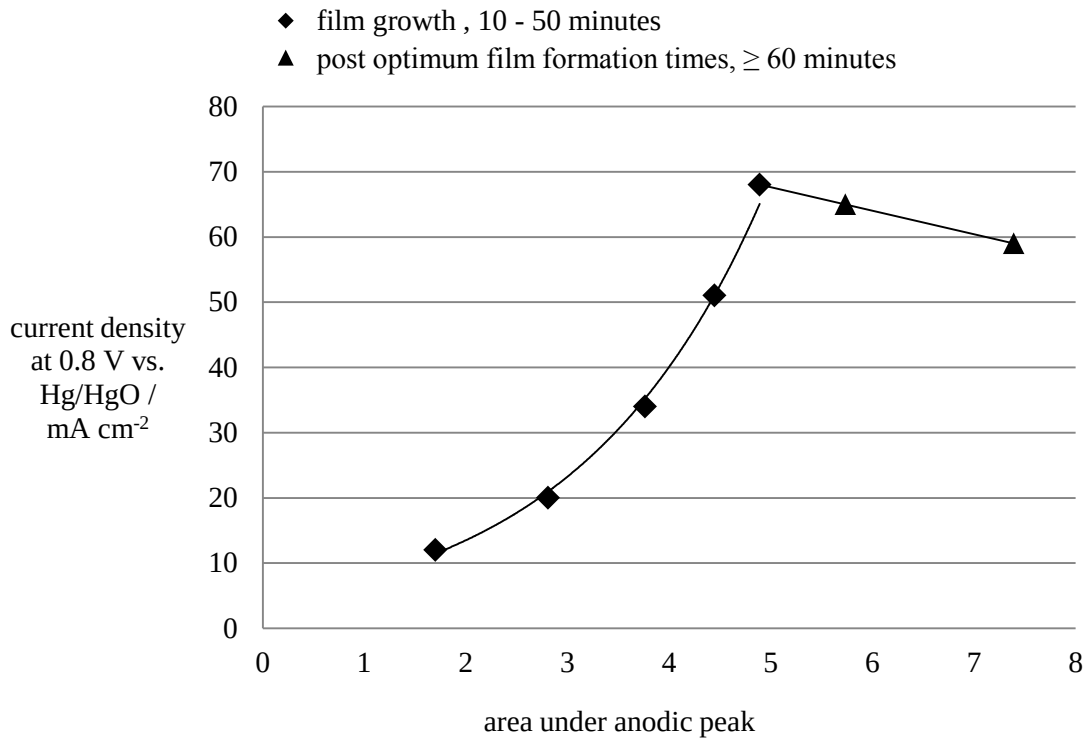

Figure 3-21 Relationship between peak area and current density of a NiO film produced by chemical bath deposition

The relationship is exponential up to the optimum deposition time of 50 minutes, after which the current density values begin to drop, despite the increase in peak area. The decrease in current density occurs at the same time as the shift in peak potentials experienced earlier in Table 3-3. The evidence points towards a transformation on the surface of the electrocatalyst film to a species which is less electrocatalytically active. Looking at the bode scheme in Figure 1-9 this is most likely a shift from the $\beta - Ni(OH)_2 \leftrightarrow \beta - NiOOH$ redox couple to the $\gamma - NiOOH \leftrightarrow \alpha - \mathrm{Ni(OH)_2}$ redox couple.

The potential for the onset for the OER was found according to section 2.2.2 and compared against the onset potential for the OER of the titanium support and IrO_2 benchmark electrodes in Figure 3-22.

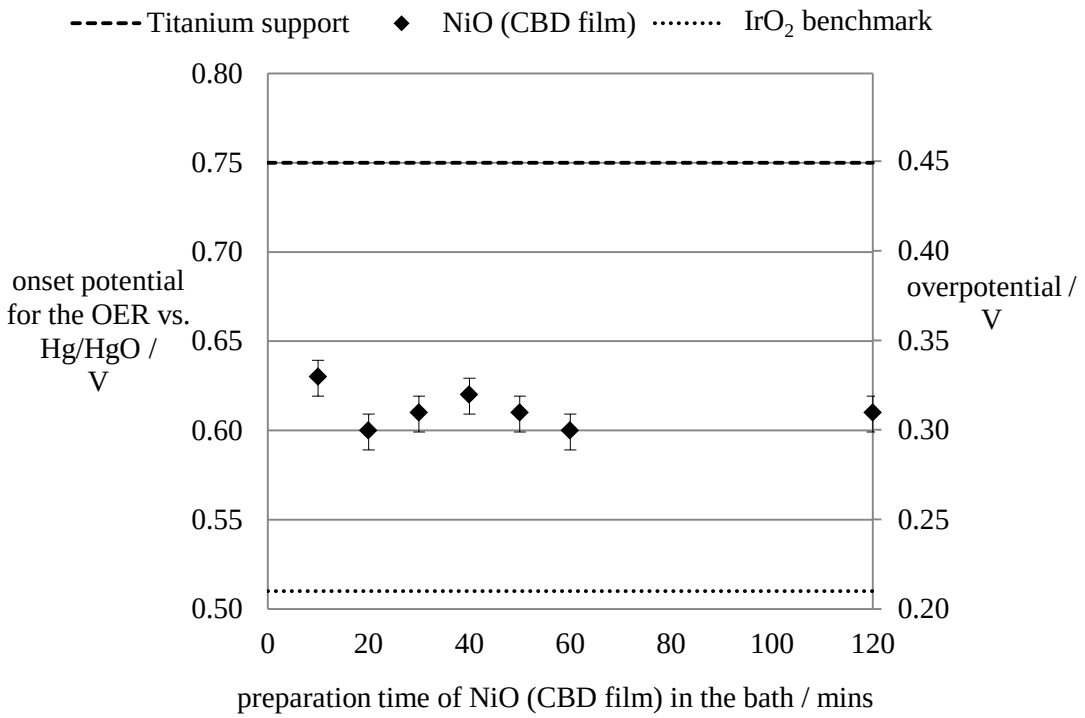

Figure 3-22 Onset potentials for the oxygen evolution reaction of NiO (CBD film) catalyst films deposited onto titanium electrodes through the chemical bath deposition procedure

The onset potential of 0.6 V does not seem to be affected by the transformation of the films redox couples. Even so the evidence shows that one of the limitations of this catalyst film is the limited formation maximum loading of catalyst (0.3 mg NiO cm^{-2}) which the method allows. In an effort to increase the activity of the NiO catalyst, particles were removed from the chemical bath after 50 minutes and deposited at higher loadings through catalysts inks and the results of this will now be discussed.

3.6.2 Oxygen evolution reaction on NiO (CBD) catalyst nanoparticles and 25 wt% PVDF

The CBD method from section 2.4.3 resulted in bulk precipitation of electrocatalytically active nano particles which have already been physically characterised in section 3.5.1. These precipitates were filtered, washed with DI water, dried and thermally treated in a furnace at 400°C for 1 hour to form pure NiO

particles. These particles were deposited to electrodes at higher loadings than those achieved directly through the CBD film method (section 2.4.3), through the use of catalyst ink containing 25 wt% PVDF binder. The steady state current densities are shown in Figure 3-23.

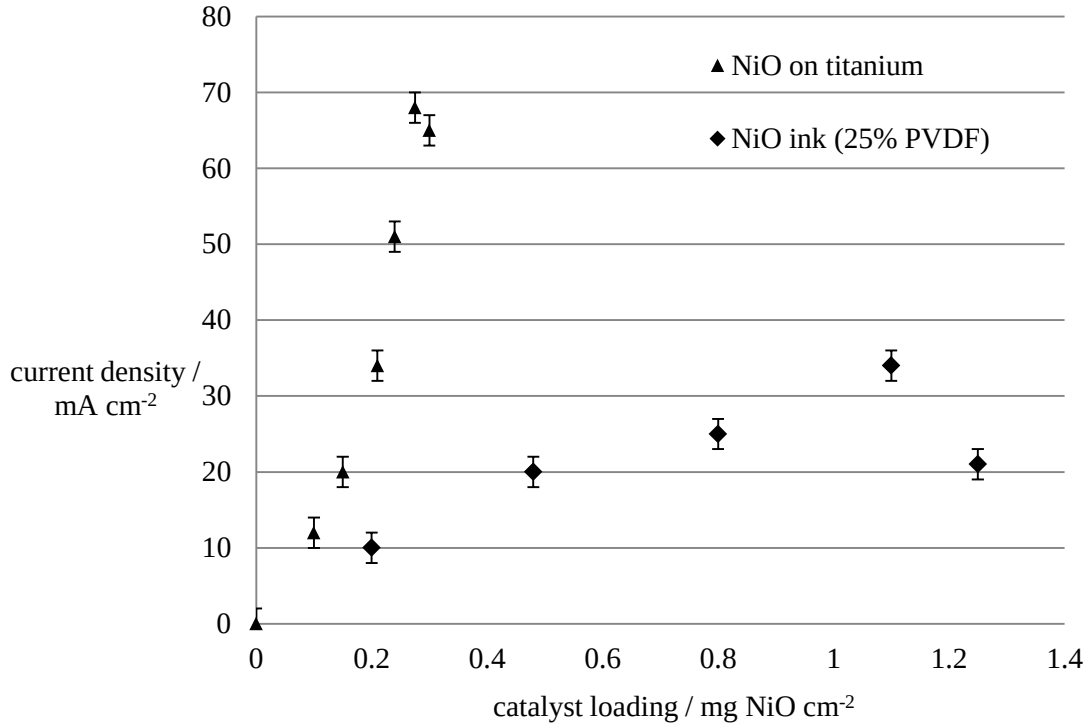

Figure 3-23 Effect of deposition method on current densities produced by NiO (CBD) catalyst films, deposited onto gold plated titanium electrodes with 25 wt% PVDF, at a potential of 0.8 V vs. Hg/HgO, in an electrolyte of 1 M NaOH at a temperature of 25°C

It is clear from Figure 3-23 that depositing the NiO catalyst film onto electrodes through the CBD procedure is superior for producing higher current densities than when the NiO is deposited utilising a catalyst ink. The decrease in performance when the NiO is alternatively deposited through catalyst inks can be attributed to a number of intrinsic factors. The film produced through catalyst inks may have been less porous in nature, reducing the active surface available for the oxygen evolution reaction mechanisms to take place. The performance drop can also be attributed to the PVDF polymer additive that is not electrochemically active and merely acts as a binding agent. The relatively low density of the PVDF (1.78 g cm^{-3}) compared to the NiO (6.67 g cm^{-2}) means that although 25 wt% of PVDF is added to the film, the resulting volume of the catalyst film is estimated to consist of 56% PVDF.

The XRD results from Figure 3-15 showed that the chemical bath deposition process produced a mixture of nickel hydroxide particles, dominated by a blend of α-$Ni(OH)_2$ and $4Ni(OH)_2 \cdot NiOOH \cdot xH_2O$. The electrocatalytic activity of this blend of nickel hydroxides was tested by depositing it onto gold plated titanium electrodes through the catalyst ink procedure detailed in section 2.4.6.

3.6.3 Oxygen evolution reaction of α-$Ni(OH)_2$ / $4Ni(OH)_2 \bullet NiOOH \bullet xH_2O$ catalyst film prepared by chemical bath deposition

The CBD procedure in section 3.5 produced a binary mix of α-$Ni(OH)_2$ / $4Ni(OH)_2 \bullet NiOOH \bullet xH_2O$ catalyst nanoparticles, which were prepared into a catalyst ink containing 25 wt% PVDF binder and THF solvent. The ink was deposited onto gold plated titanium electrodes with loadings between 0.5 and 2 mg cm^{-2}. Cyclic voltammetry was performed on the electrodes in an electrolyte of 1 M NaOH, at a temperature of 25°C, by cycling between 0.2 and 0.8 V vs. Hg/HgO until stability was achieved. As an example, the CVs for an electrode prepared with 0.6 mg will now be shown. The 1^{st} - 10^{th} cycles are shown in Figure 3-24, the 11^{th} – 19^{th} cycles in Figure 3-25 and the 20^{th} – 28^{th} cycles in Figure 3-26.

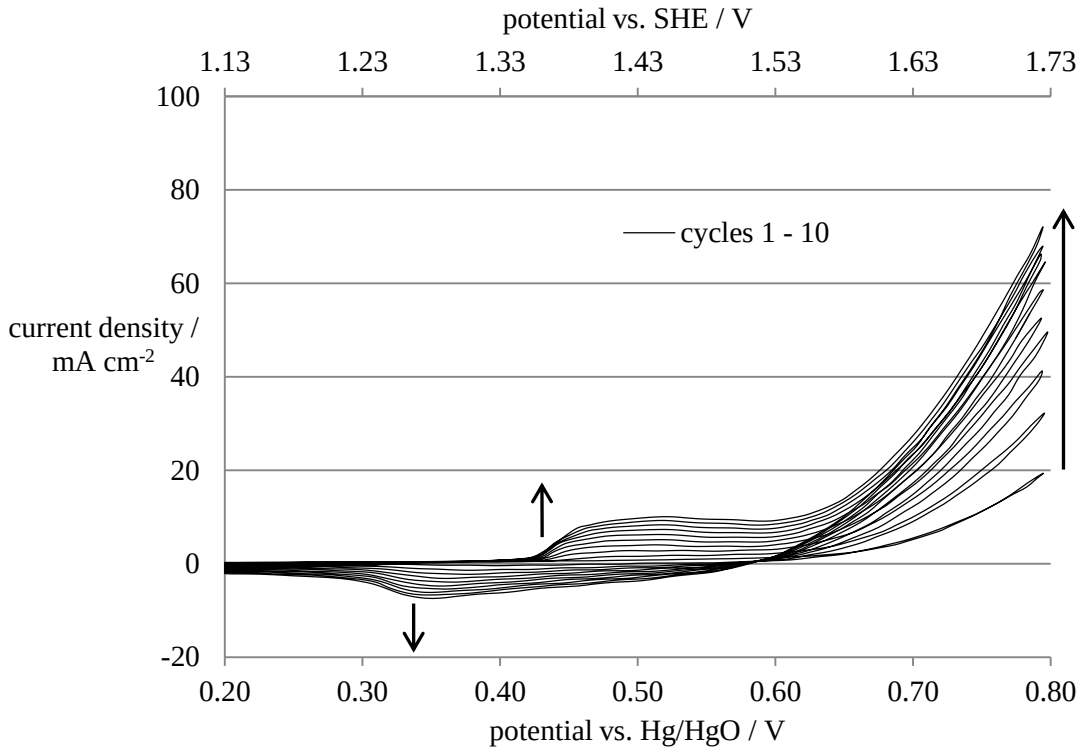

Figure 3-24 Cycles 1 – 10 of a gold plated titanium electrode containing 0.6 mg cm^{-2} of α-Ni(OH)$_2$ / 4Ni(OH)$_2$•NiOOH•xH$_2$O catalyst in an electrolyte of 1 M NaOH at a temperature of 25°C and a scan rate of 30 mV s^{-1}

The 1st cycle in Figure 3-24 shows that shows very little activity; however, there is a progressive development of an anodic ($E_{pa} = 0.52\,V$) and cathodic ($E_{pc} = 0.34\,V$) peak corresponding to the redox reaction of Equation 3-9.

$$Ni(OH)_2 + OH^- \leftrightarrow NiOOH + H_2O + e^- \qquad \textbf{Equation 3-9}$$

Figure 3-24 shows that in conjunction with the increase in peak size there is an increase in current density at the higher potentials ($E > 0.6\,V$ vs. Hg/HgO) associated with oxygen evolution. This is due to a higher amount of catalytically active material becoming available, either through formation on the film's surface or an increased availability of species in the film.

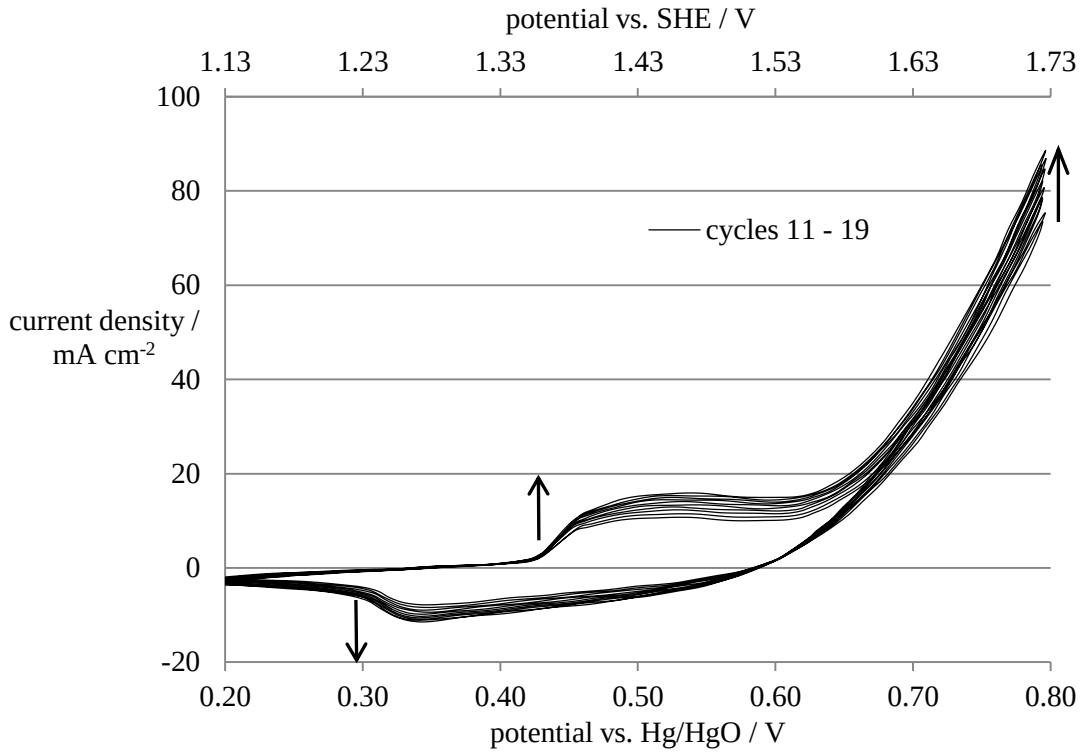

Figure 3-25 Cycles 11 – 19 of a gold plated titanium electrode containing 0.6 mg cm^{-2} of α-Ni(OH)$_2$ / 4Ni(OH)$_2$•NiOOH•xH$_2$O catalyst, in an electrolyte of 1 M NaOH at a temperature of 25°C and at a scan rate of 30 mV s^{-1}

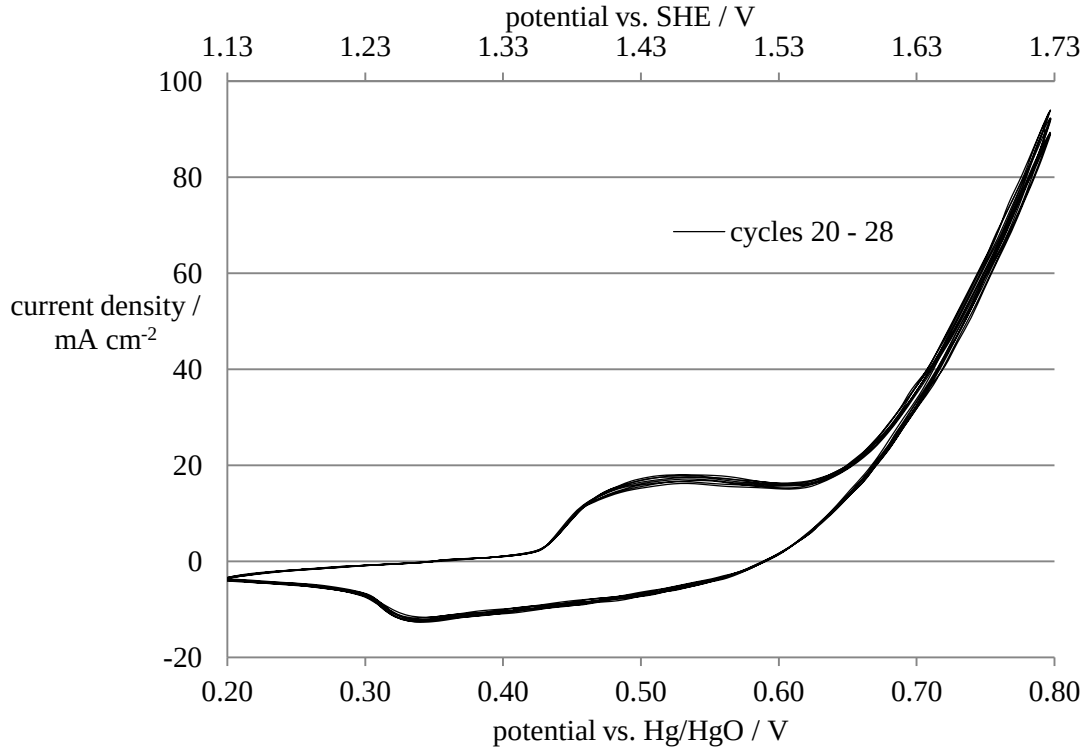

Figure 3-26 Cycles 20 – 28 of a gold plated titanium electrode containing 0.6 mg cm^{-2} of α-Ni(OH)$_2$ / 4Ni(OH)$_2$•NiOOH•xH$_2$O catalyst, in an electrolyte of 1 M NaOH at a temperature of 25°C and at a scan rate of 30 mV s^{-1}

Figure 3-25 and Figure 3-26 show that with continued cycling the rate of increase in the surface area and the peak current density from the material being produced is decreasing and becoming more stable. A similar response has been reported by Snook et al [101] who investigated the activity of nickel hydroxide in 7 M KOH. They attributed the cycling to a conversion of α-$Ni(OH)_2$ to the more catalytically active β-$Ni(OH)_2$, as per the Bode Scheme in Figure 1-9. Between the first and last cycle, the potential for the oxidation, or anodic peak E_{pa}, shifts from approximately 0.50 to 0.53 V, whist the cathodic peak E_{pc} shifts from approximately 0.37 to 0.34 V by the 28th cycle. The ΔE has increased from 0.13 to 0.16 V, which shows a slight increase in the difficulty of oxidising and reducing the species because of the larger potentials required.

Effect of electrolyte temperature

The effect of the electrolyte temperature on the performance is shown in Figure 3-28 for electrolyte temperatures of 25, 40 and 60°C.

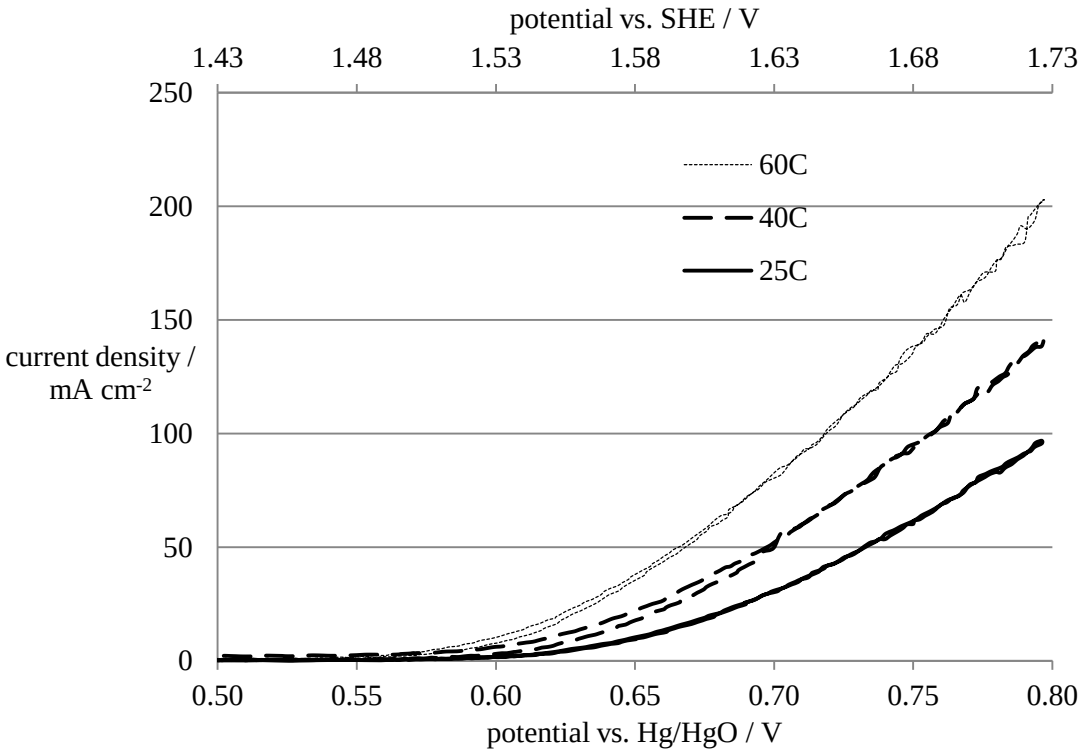

Figure 3-27 Steady state current response of electrochemically treated α-$Ni(OH)_2$ / $4Ni(OH)_2$•NiOOH•xH_2O catalyst films in an electrolyte of 1 M NaOH at 25, 40 and 60°C

The current density values of all electrodes were taken at 0.8 V vs. Hg/HgO from their steady state current response and plotted against the catalyst loading and this is shown in Figure 3-28.

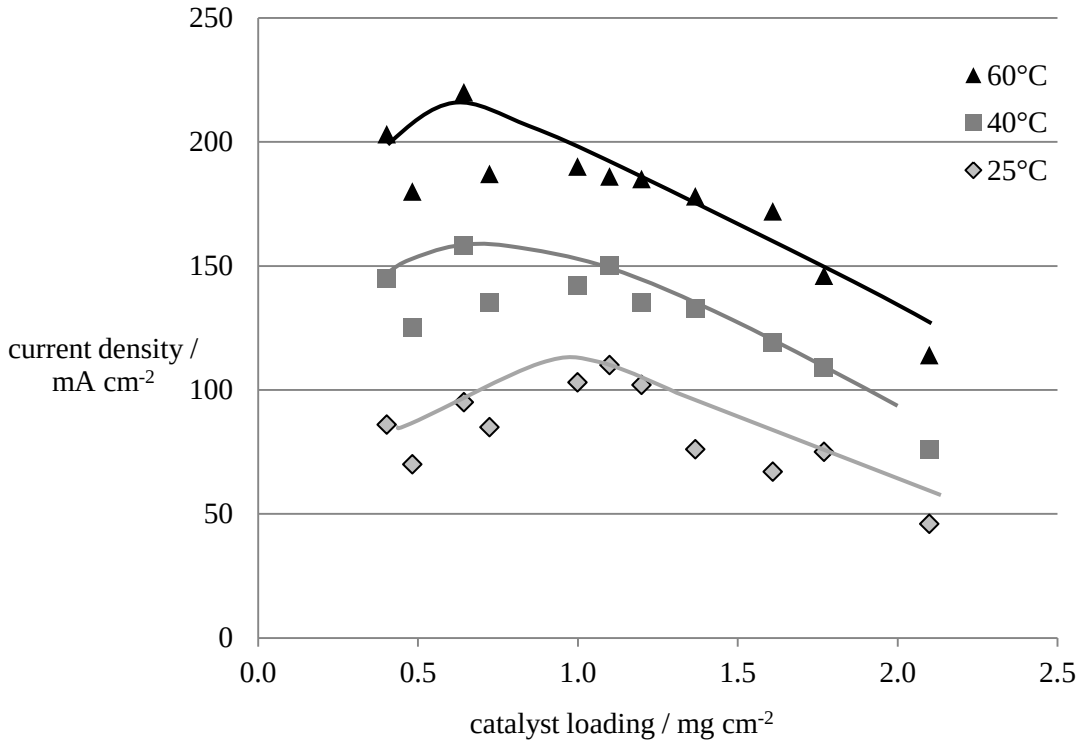

Figure 3-28 Effect of catalyst loading and temperature of the electrolyte on the current density values for the OER on α-$Ni(OH)_2$ / $4Ni(OH)_2$•NiOOH•xH_2O catalyst films taken at a potential of 0.8 V vs. Hg/HgO in an electrolyte of 1 M NaOH

Optimum current density values are taken from the apex of the best fit curves in Figure 3-28. They equate to current densities of 110, 160 and 220 mA cm^{-2} at temperatures of 25, 40 and 60°C respectively. Interestingly, the apex seems to shift towards lower loadings as the temperature is increased. This means that the increase in temperature of the electrolyte has a greater effect on performance of the thinner films. This shift of optimum catalyst loading could be explained by a balance between mass transport (gas evolution) and surface area (electrocatalytic activity). Oxygen gas builds up due to a thick catalyst layer and can block the surface of the catalyst film, an action that will increase at higher temperatures.

The relationship between the peak areas of all the electrodes and the resulting steady state current densities at 25°C is shown in Figure 3-29.

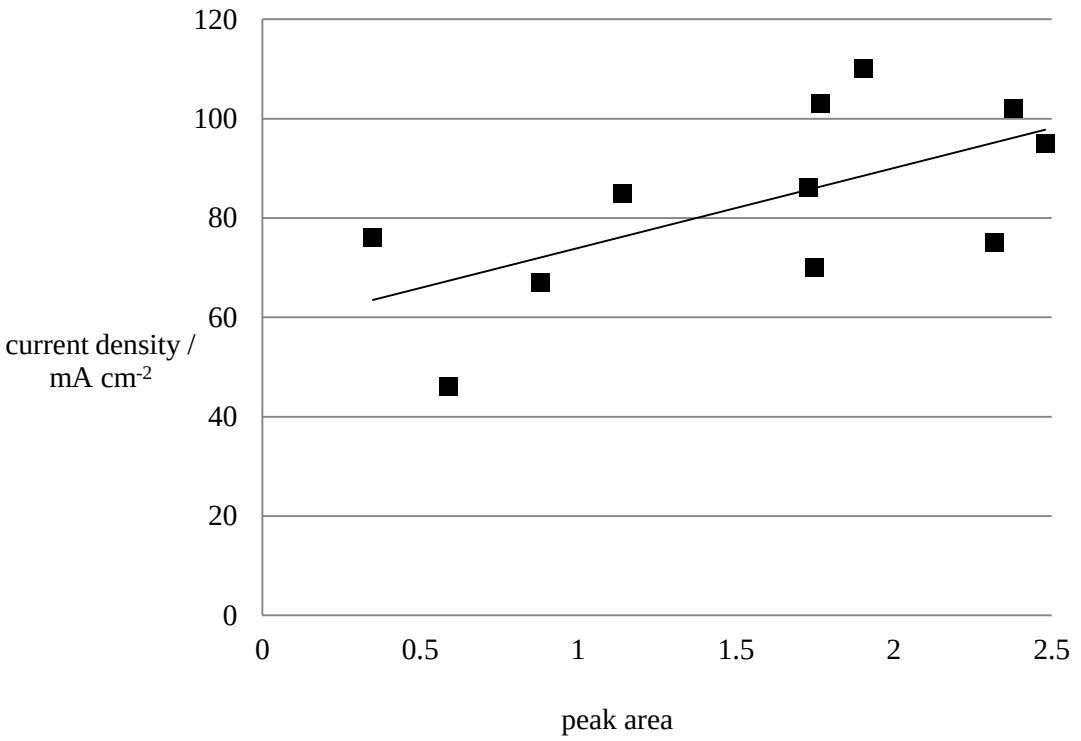

Figure 3-29 Relationship between peak areas of α-$Ni(OH)_2$ / $4Ni(OH)_2$•NiOOH•xH_2O electrodes and the resulting current density performance in a 1 M NaOH electrolyte at a temperature of 25°C

There appears to be a strong positive relationship between the peak area, or voltammetric charge, associated with the catalyst and the resulting OER performance. This shows that the nickel hydroxide responsible for the voltammetric charge has a positive effect on the oxygen evolution reaction. The deviation from the best fit line can be associated with fluctuations in the scan rates, which have been described in section 2.2.8. It can also be suggested that there is a mix of nickel hydroxides responsible for the voltammetric charge but the activity of these hydroxides towards oxygen evolution is variable. This mix of nickel hydroxides could be a consequence of the lack of thermal treatment that has been performed on the particles. The catalytic activity of nickel hydroxides can be improved by combining the nickel with another transition metal oxide (see section 1.7.4), and this study will now look into results of the catalyst $NiCo_2O_4$.

3.7 Characterization of $NiCo_2O_4$

The mixed metal oxide electrocatalyst $NiCo_2O_4$ was synthesized according to the method detailed in section 2.4.4. XRD analysis was performed on the two powders using an Xpert-Pro diffractometer system. The red line represents the powder formed from thermal decomposition at 300°C and the black line represents thermal decomposition at 280°C.

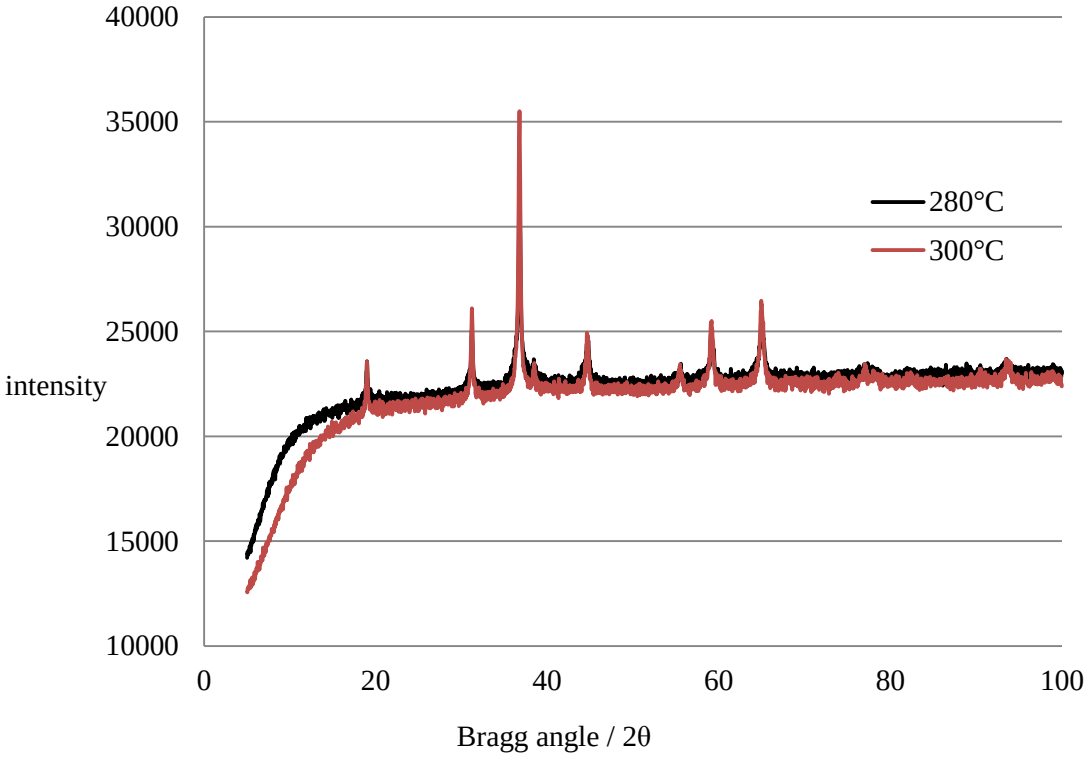

Figure 3-30 XRD patterns of $NiCo_2O_4$ spinels calcined at temperatures of 280°C (black line) and 300°C (red line) for 1 hour

Both samples show major peaks at 2θ values of 31.2, 36.8, 44.6, 59.1 and 64.9, which correspond to a single phase $NiCo_2O_4$ spinel (JCPDS 00-020-0781). This is in agreement with similar work by Guerrini [102] who also decomposed solutions of nickel and cobalt nitrate, with concentrations of 0.2 M, at 300°C.

The particle sizes, calculated from the Scherrer formula from Appendix H, are 163 nm for 280°C and 189 nm for 300°C. The lower decomposition temperature has

slightly decreased the particle size. The particles are much larger than the catalysts produced earlier by chemical bath deposition method (30 nm and 58 nm for NiO and α-$Ni(OH)_2$/$4Ni(OH)_2$•NiOOH•xH_2O respectively) and thermal decomposition, although the synergistic effect of combining the nickel and cobalt towards electrochemical activity will now be studied.

3.8 Electrochemical studies on $NiCo_2O_4$

3.8.1 Cyclic voltammetry

The nickel-cobalt powders prepared from the method described in 2.4.4 were formed into separate catalyst inks, with 25 wt% PVDF binder and NMP as a solvent. The catalyst ink was deposited onto gold plated titanium electrodes at a loading of 1.0 mg cm^{-2} by the pipette method. The electrolyte was prepared from 98% NaOH pellets to a concentration of 1 M with DI water. Cyclic voltammetry was performed at a scan rate of 30 mV s^{-1} between 0.2 and 0.8 V vs. Hg/HgO at 25°C for both $NiCo_2O_4$ (280°C) (Figure 3-31) and $NiCo_2O_4$ (300°C) (Figure 3-32).

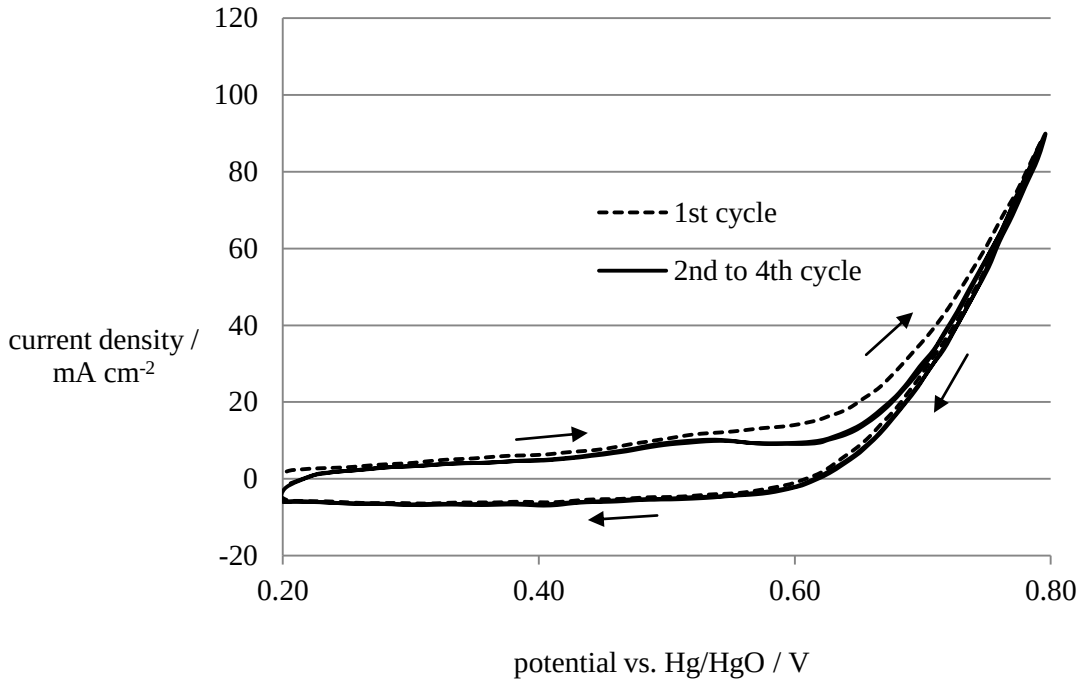

Figure 3-31 Cyclic voltammetry scans at a scan rate of 30 mV s^{-1}, on a gold plated titanium electrode with a catalyst loading of 1 mg $NiCo_2O_4$ cm^{-2} (thermally decomposed at 280°C), in an electrolyte of 1 M NaOH and at a temperature of 25°C

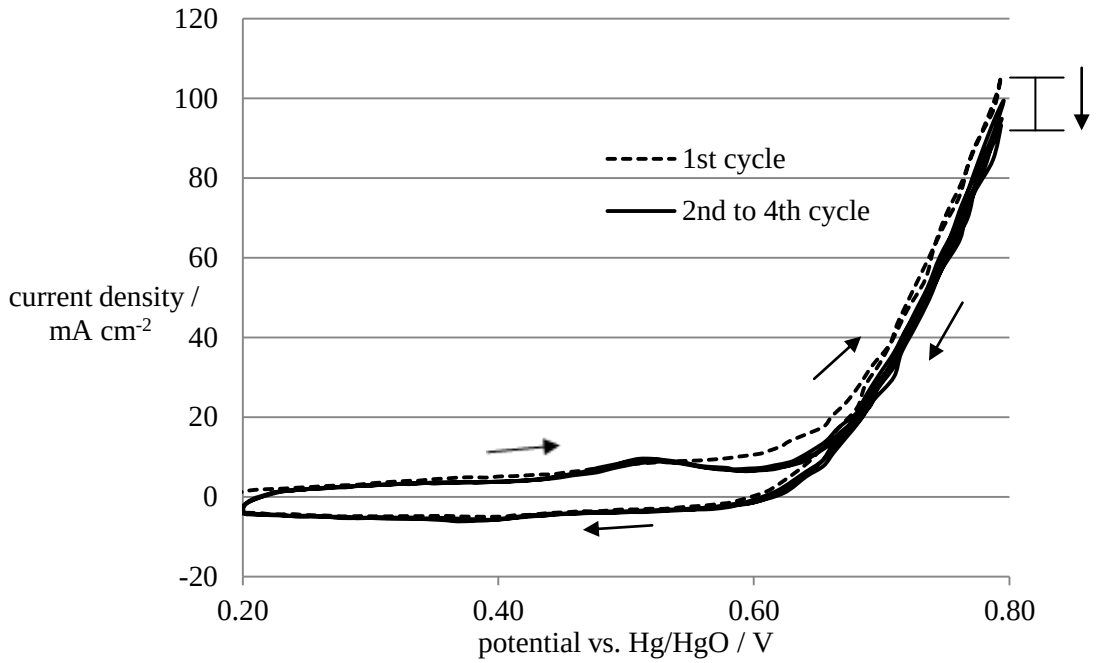

Figure 3-32 Cyclic voltammetry scans at a scan rate of 30 mV s^{-1}, on a gold plated titanium electrode with a catalyst loading of 1 mg $NiCo_2O_4$ cm^{-2} (thermally decomposed at 300°C), in an electrolyte of 1 M NaOH and at a temperature of 25°C

For the positive going potential-sweep between 0.2 and approximately 0.6 V vs. Hg/HgO, both $NiCo_2O_4$ (280) and $NiCo_2O_4$ (300) show charging of the double layer and transformation of the oxidation states of the catalyst (see section 3.8.2). Beyond approximately 0.6 V vs. Hg/HgO the sharp rise in current density relates to oxygen evolution. There is very little hysteresis for the region beyond 0.7 V, which indicates that the species has not changed from the anodic sweep at the same potentials. The current densities reach negative values which indicated that there was discharge from the catalyst film.

The voltammetric scans for $NiCo_2O_4$ thermally decomposed at 300°C show slightly more hysteresis at the higher potential ranges than the scans produced by $NiCo_2O_4$ thermally decomposed at 280°C. For each cycle, the current density values for $NiCo_2O_4$ (280°C) at 0.8 V vs. Hg/HgO remains consistent at 90 mA cm^{-2}, whilst the current density values for $NiCo_2O_4$ (300°C) at the same potential decrease from 106 to 93 mA cm^{-2}. Due to the high scan rate it is difficult to ascertain the difference in electrochemical activity of these catalysts based on these figures, but this can be more easily achieved in the study in section 3.8.3 when lower scan rates are utilised.

3.8.2 Peak analysis

For both decomposition temperatures, the voltammograms are stable after four cycles. Figure 3-33 shows the CV response for the lower potentials prior to the OER for both catalysts.

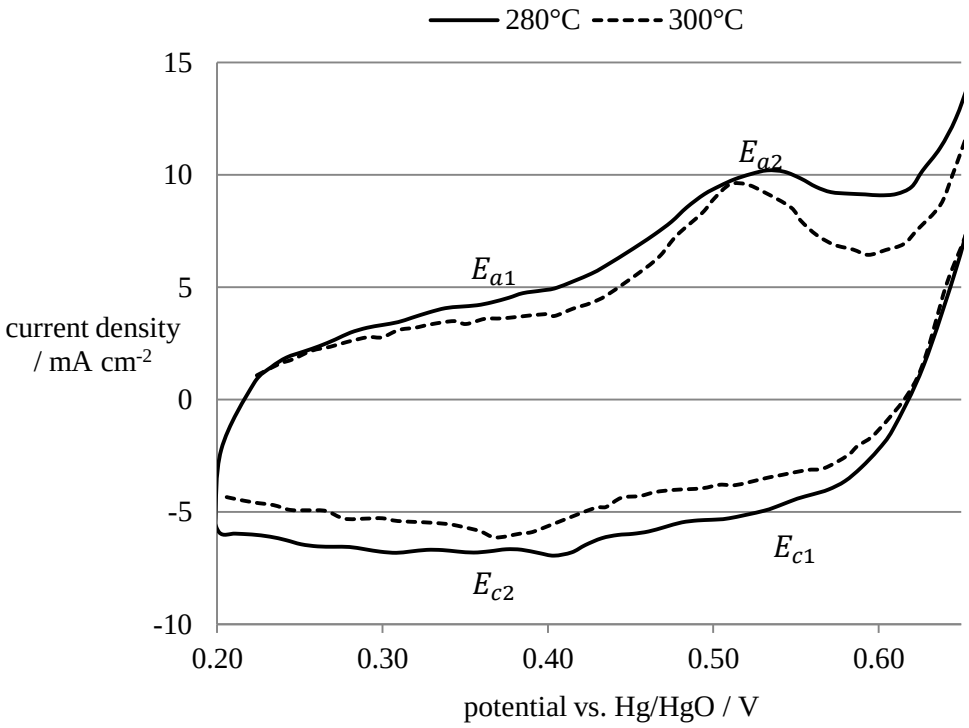

Figure 3-33 Stabilised anodic and cathodic peaks on $NiCo_2O_4$ electrodes in an electrolyte of 1 M NaOH at a temperature of 25°C, a scan rate of 30 mV s^{-1}, and a catalyst loading 1 mg cm^{-2}

Both electrodes exhibit double anodic and cathodic peaks, which correspond to the two redox couples of Ni(II)/Ni(III) and Co(II)/Co(III). Although they are not as well defined as in similar work by Haenen [103], their locations are summarised in Table 3-4. There reduced definition could be attributed to a less homogenous catalyst layer as a result of the ink deposition method utilised.

Table 3-4 Anodic and cathodic peak locations for $NiCo_2O_4$ catalyst (thermally decomposed at 280°C and 200°C) in an electrolyte of 1 M NaOH at a temperature of 25°C and a scan rate of 30 mV s^{-1}

	V vs. Hg/HgO / V vs. SHE					
Thermal decomposition temperature	E_{a1}	E_{a2}	E_{c1}	E_{c2}	ΔE for Ni(II)/Ni(III)	ΔE for Co(II)/Co(III)
280°C	0.32 / 1.246	0.52 / 1.446	0.51 / 1.436	0.39 / 1.316	0.19	0.13
300°C	0.32 / 1.246	0.51 / 1.436	0.51 / 1.436	0.39 / 1.316	0.19	0.12

The ΔE for the Ni(II)/Ni(III) couple resembles the same values produced by the peaks of NiO (CBD) in section 3.6 and NiOOH (CBD) section 3.6.3. The Co(II)/Co(III) couple has a ΔE value that resembles those reported by Wu et al [69] who prepared $NiCo_2O_4$ using a different procedure, although the catalyst was tested under similar electrolysis operating conditions of a 1 M NaOH electrolyte at 25°C. Haenen et al [103] claims that for thermal decomposition temperatures less than 400°C, the anodic and cathodic peak potentials of $NiCo_2O_4$ do not depend on the temperature of the decomposition, although the slight shift experienced in this research on E_{a2} can also be seen in their research paper.

The area underneath these peaks corresponds to the charge and is proportional to the number of electrochemically reactive surface sites which are in contact with the solution. From Figure 3-33, it is visually apparent that this surface area is connected to the thermal decomposition temperature used to form the catalyst. To confirm, integration of the voltammetric curve gives the peak area, which is directly proportional to the voltammetric charge that is related to the surface redox reactions. The relationship between the peak areas, $|j|$, and the voltammetric charge, q*, is shown in Equation 3-10.

$$q^* = \int_{0.20\,V}^{0.60\,V} \frac{|j|}{\upsilon} dE \qquad \textbf{Equation 3-10}$$

The value of the anodic peak areas are used for comparison and the corresponding peaks of $NiCo_2O_4$ (280) and $NiCo_2O_4$ (300) (from Figure 3-33) are shown in Table 3-5.

Table 3-5 Effect of thermal treatment temperature on the surface properties of $NiCo_2O_4$

Thermal treatment temperature of $NiCo_2O_4$	Particle size / nm	Anodic peak area	Current density at 0.8 V vs. Hg/HgO (25°C) / mA
280°C	163	2.231	97
300°C	189	1.837	96

It is well known that higher thermal decomposition temperatures lead to agglomeration of particles and larger particle sizes [104] [105] [106]. The decrease in thermal treatment temperature of $NiCo_2O_4$ has led to a decrease in particle size, as proved by XRD data in Figure 3-30. This in turn can be said to have a direct effect on the active surface area of the catalyst available per unit mass. This increased area is represented by voltammetric charge depicted by the anodic peak areas in Figure 3-33. This active surface area can be said to be the major contribution towards the increase in catalytic activity towards the oxygen evolution reaction, which is quantified by the current density values and this is more evident at higher electrolyte temperatures as shown in the following section.

3.8.3 Effect of electrolyte temperature

The steady state current density responses of the electrodes containing the $NiCo_2O_4$ (280) and $NiCo_2O_4$ (300) catalyst films, at electrolyte temperatures of 25, 40 and 60°C, are shown in Figure 3-34.

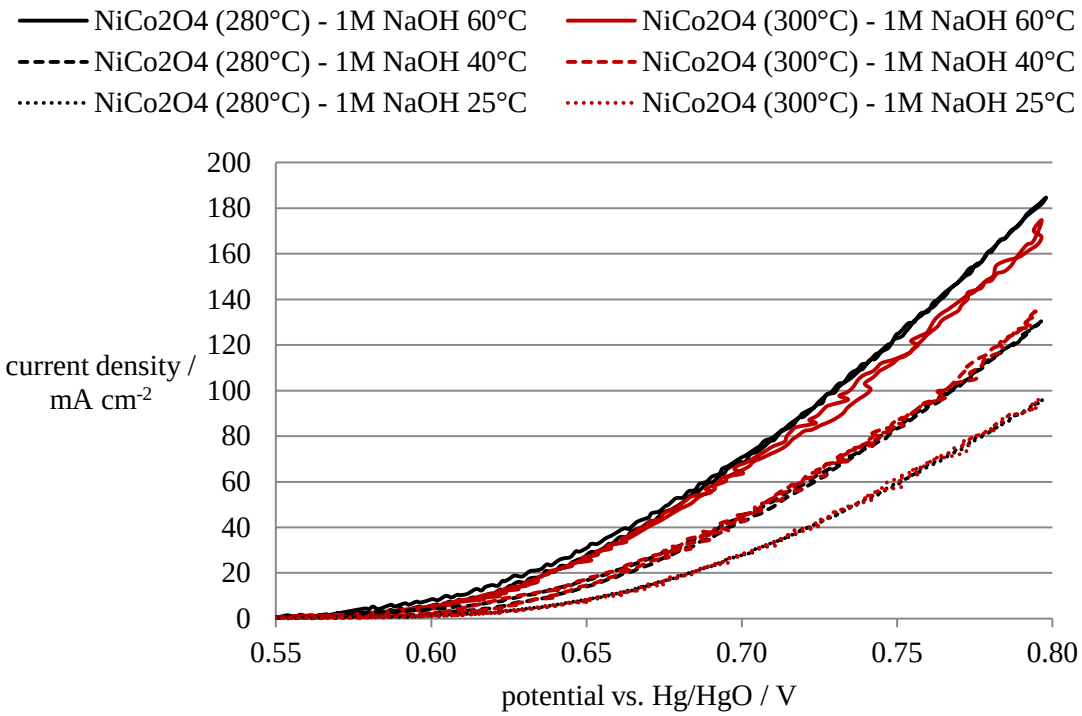

Figure 3-34 Temperature effect on the steady state current responses on $NiCo_2O_4$ electrodes in an electrolyte of 1 M NaOH, with a scan rate of 0.5 mV s^{-1}

Both catalysts appear to show similar electrochemical behaviour at the temperature of 25°C, and it is not until the electrolyte temperature is increased to 40°C and then 60°C that they show distinguished current density performances at fixed potentials. At 40°C the $NiCo_2O_4$ prepared at the lower decomposition temperature of 280°C yields an improved electrochemical performance of 135 mA cm^{-2}, compared to the 127 mA cm^{-2} produced by $NiCo_2O_4$ prepared at 300°C. At 60°C the performances increase to 185 mA cm^{-2} and 171 mA cm^{-2} for thermal decomposition temperatures of 280 and 300°C respectively. This shows that there is a slight relationship between the thermal decomposition temperature used in the preparation of the catalyst and the resulting electrochemical performance in terms of current density. A cause of this could be linked to the smaller particle sizes, previously measured by XRD in section 3.7, which have already shown an increase in active surface area in the anodic and cathodic peaks studied in section 3.8.2.

3.9 Mass activity of the oxygen evolution reaction catalysts

In order to compare catalysts, a common methodology for their analysis is their mass activity which is given by the following relationship:

$$mass\ activity = \frac{current\ density}{catalyst\ loading} \qquad \textbf{Equation 3-11}$$

A summary of the mass activities of the catalysts tested on in this chapter is shown in Table 3-6 and depicted in Figure 3-35.

Table 3-6 Performance summary of catalysts for the oxygen evolution reaction in 1 M NaOH at a temperature of 25°C in a glass half cell electrolyser

Electrocatalyst	Description	Electrode / Additive	Performance per mass / mA cm^{-2} mg^{-1}	Data source
IrO_2	Noble-metal catalyst produced by Adam's Fusion method	Gold (Ti) 25% PVDF	438	Figure 3-2 219 mA / 0.5 mg IrO_2
NiO (commercial)	Commercial NiO particles from Sigma Aldrich	Gold (Ti) 25% PVDF	45	Figure 3-7 90 mA / 2 mg NiO (commercial)
NiO (400)	NiO synthesised through thermal decomposition of nickel nitrate salts at 400°C	Titanium mesh	46.1	Figure 3-9 83 mA / 1.8 mg NiO (400)
NiO (450)	NiO synthesised through thermal decomposition of nickel nitrate salts at 450°C	Titanium mesh	45.6	Figure 3-9 73 mA / 1.6 mg NiO (450)
NiO (urea)	NiO synthesized through solution growth followed by thermal decomposition at 400°C	Gold (Ti) 25% PVDF	43.75	Figure 3-13 70 mA / 1.6 mg NiO (urea)
NiO (CBD film)	NiO film directly deposited onto a titanium foil in the CBD method	Titanium foil	247	Figure 3-20 68 mA / 0.275 mg NiO (CBD)
NiO (CBD)	NiO particles retained from the chemical bath and thermally treated at 400°C	Gold (Ti) 25% PVDF	31	Figure 3-23 34 mA / 1.1 mg NiO (CBD)
α-$Ni(OH)_2$ / $4Ni(OH)_2$•NiOOH•xH_2O, or NiOOH (CBD)	Particles formed in the chemical bath deposition procedure but not thermally treated	Gold (Ti) 25% PVDF	109	Figure 3-28 104 mA / 0.95 mg α-$Ni(OH)_2$ / $4Ni(OH)_2$•NiOOH•xH_2O
$NiCo_2O_4$ (300)	Mixed metal oxide catalyst synthesised through thermal decomposition of nickel nitrate and cobalt nitrate salts at 300°C	Gold (Ti) 25% PVDF	96	Figure 3-34 96 mA / 1 mg $NiCo_2O_4$ (300)
$NiCo_2O_4$ (280)	Mixed metal oxide catalyst synthesised through thermal decomposition of nickel nitrate and cobalt nitrate salts at 280°C	Gold (Ti) 25% PVDF	97	Figure 3-34 97 mg / 1 mg $NiCo_2O_4$ (280)

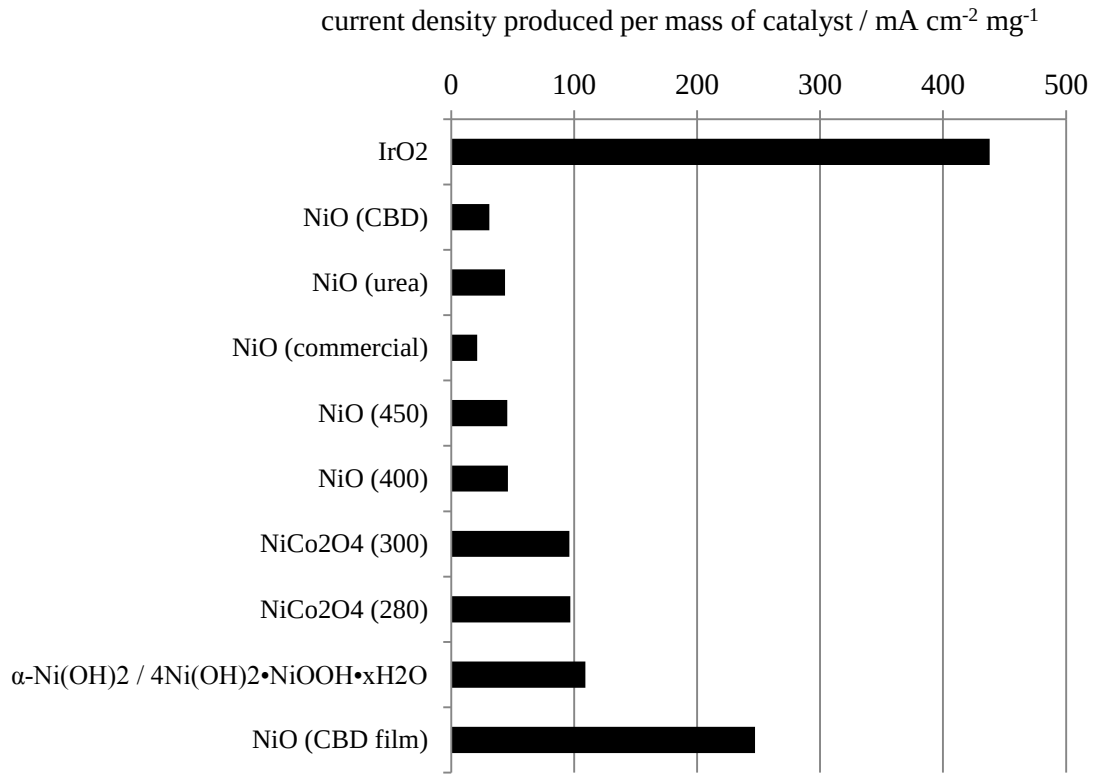

Figure 3-35 Performance of electrocatalysts relative to catalyst mass for the oxygen evolution reaction in an electrolyte of 1 M NaOH at a temperature of 25°C

The benchmark catalyst, IrO_2, shows superior results to all non-noble metal catalysts. The most promising non-noble metal catalyst is NiO (CBD film) which shows over 56% of the mass activity of the noble metal IrO_2 in the same glass half cell electrolyser under the same operating conditions. This is significantly more than all the other catalysts studies in this research project.

3.10 Hydrogen evolution reaction results summary

For all studies on the hydrogen evolution reaction, the three electrode glass half cell electrolyser was prepared as described in section 2.3. The counter electrode was made from a piece of nickel foam. The hydrogen evolution reaction takes place at cathodic potentials in the negative potential region, with similar overpotentials for those used in the previous oxygen evolution reaction studies, thus a potential window of -0.8 to -1.4 V vs. Hg/HgO was utilised. Two molybdenum based electrocatalytically active materials were studied and they are:

1) Molybdenum foil
2) Nickel molybdenum oxide nanopowder

Molybdenum foil was cut to a square 1 cm by 1 cm, with the reverse and edges coated in an acetoxy silicone sealant (RS Components – Silcoset 158). The catalyst nano-powder $NiMoO_4$ was synthesized according to section 2.4.5 and deposited onto a gold plated titanium electrode with a loading of 1 mg cm^{-2} and 25 wt% PVDF binder using the ink method described in section 2.4.6. A summary of tests run on molybdenum foil and nickel molybdenum oxide are shown in Table 3-7 and show strong similarity to results presented in literature regarding similar Ni-Mo composites.

Table 3-7 Summary of kinetic and performance of molybdenum and nickel molybdenum oxide for the hydrogen evolution reaction in an electrolyte of 1 M NaOH at a temperature of 25°C

Catalyst	Electrolyte and temperature	Tafel slope, -b / mV dec^{-1}	Exchange current density, j_0 / A cm^{-2}	E_{cell} / V	-j / mA cm^{-2}
Molybdenum foil	1 M NaOH 25°C	120 to 134	2.5×10^{-4}	-1.4	45
$NiMoO_4$ / 25% PVDF	1 M NaOH 25°C	119 to 150	6.9×10^{-4}	-1.4	160
Ni+44% Mo Panek and Budniok [50]	5 M KOH room temperature	130 to 170	1.6×10^{-3}	$\mu = 0.25$	100
Tasic [51]	6 M KOH 30°C	135	3.2×10^{-3}	-	-

3.11 Conclusions of glass half cell electrolyser results

Several non-noble metal catalysts have been successfully synthesized and tested in an alkaline electrolyte half cell.

The catalyst NiO was synthesized and deposited directly onto titanium mesh through thermal decomposition of nickel nitrate salts with final calcination temperatures of 400°C and 450°C (section 2.4.1). It was found that the lower thermal decomposition temperature resulted in higher current densities (Figure 3-9) due to the presumably smaller particle sizes and thus the increase in available active surface area per mass of catalyst.

The chemical bath deposition method was responsible for the formation of a precipitate that was a blend of nickel hydroxides which were characterised by XRD in section 3.5.1 to be α-$Ni(OH)_2$ and $4Ni(OH)_2$•$NiOOH$•xH_2O nano particles. Initial electrochemical assessment in section 3.6.3 showed relatively little activity towards the oxygen evolution reaction compared to other nickel based compounds tested in this research. However with progressive cycling there was progressive development of anodic ($E_{pa} = 0.52\,V$) and cathodic ($E_{pc} = 0.34\,V$) peaks in conjunction with an increase in current density at the higher potentials. The optimum catalyst loading was approximately 1.2 mg cm^{-2} however at higher temperatures this appeared to shift toward lower loadings of approximately 0.7 mg cm^{-2}. This could be explained by a balance between mass transport (gas evolution) and surface area (electrocatalytic activity). Oxygen gas builds up due to a thick catalyst layer and can block the surface of the catalyst film, an action that will increase at higher temperatures. Performances of the nickel hydroxides were similar to those produced by the binary transition metal oxide, $NiCo_2O_4$, which was synthesized through thermal decomposition at 280 and 300°C (section 2.4.4) and characterized by XRD in section 3.7. The XRD showed that a decrease in particle size was achieved by reducing the final calcination temperature (Figure 3-30). Cyclic voltammetry proved that this decrease in particle size lead to slightly larger active peak areas area of the catalyst (see Table 3-5) which in turn was the cause of higher current densities.

The NiO film produced by CBD produced the highest mass activity, although when the same catalyst was deposited as a nanopowder, it produced lower current densities when compared to other nanopowder catalysts as the highly porous structure of the film produced by CBD was lost. Consequently, it was not tested further in the alkaline polymer electrolyser. The most promising catalysts for the oxygen evolution reactions from the glass half cell electrolyser are:

- α-$Ni(OH)_2$ / $4Ni(OH)_2 \bullet NiOOH \bullet xH_2O$ which was obtained from the chemical bath deposition procedure and produced 104 mA cm^{-2} at a potential of 1.8 V vs. Hg/HgO
- $NiCo_2O_4$ (280) spinel synthesized through thermal decomposition of nitrate salts at 280°C and produced 97 mA cm^{-2} at a potential of 1.8 V vs. Hg/HgO

The results of the experiments conducted on these catalysts in the polymer electrolyser will now be discussed.

4 Alkaline polymer electrolyser results

4.1 Chapter introduction

This chapter gives experimental details that were conducted on an alkaline polymer electrolyte membrane electrolyser. Initial fabrication of the cell required careful selection and preparation of the MEA materials. These materials include gold plated titanium mesh as anode and cathode GDLs. Carbon cloth provided by Freudenberg FCCT was included for the cathode catalyst support. An anion exchange membrane was provided by the University of Surrey.

Section 4.2 of this chapter is primarily concerned with establishing suitable operating conditions for the electrolyser. Details are given of the experiments which aided operating controls to be established on the parameters to which the polymer electrolyte is sensitive to. These were conducted without catalyst layers so that behaviour of the membrane could be established prior to any electrochemical operation of the electrolyser.

Section 4.3 gives results of experiments on the electrocatalyst blend of α-$Ni(OH)_2$ / $4Ni(OH)_2$•NiOOH•xH_2O particles, which were formed from the chemical bath deposition method and had not been thermally treated. The results are compared with those achieved by the same catalyst in the half cell.

Another promising catalyst which produced a similar performance was the binary metal oxide $NiCo_2O_4$, produced through thermal decomposition of a mixture of nickel and cobalt nitrate salts.

The catalysts were deposited through airbrushing catalyst inks into films on the anode side of the Surrey membrane with an ionomer mix of PVBC/PVC. The MEA utilised a commercial platinum black on the cathode and α-$Ni(OH)_2$ /

$4Ni(OH)_2 \cdot NiOOH \cdot xH_2O$ on the anode in section 4.3. The commercial platinum black was substituted for $NiMoO_4$ (synthesized according to section 2.4.5) in later experiments with $NiCo_2O_4$ (280) on the anode. Results are discussed before main conclusions of the research project and recommendations for future work.

4.2 Resistance optimization on the alkaline anion exchange membrane polymer electrolyser

The polymer electrolyser was assembled as depicted in Figure 2-14, excluding the anion exchange membrane and catalyst layers. The anion exchange membrane was substituted for a thin foil of stainless steel which would enable contact to be made between the anode and cathode current collectors of the electrolyser. An EIS measurement showed the resistance of the cell as 0.010 Ω at 25°C.

4.2.1 Effect of torque

To investigate the effect of torque on the system the Surrey JK80L membrane was prepared as described in section 2.5. The MEA was assembled as shown in Figure 2-14 but no catalyst layers were introduced to the system. This enabled identification of any resistances within the cell associated with the membrane. The resistance of the cell was established through EIS at gradually increasing torque levels up to 4 N m. Pure DI water was circulated through the cell which was maintained at a temperature of 25°C. The trend of the cell resistance as this torque increased is shown in Figure 4-1 and the experiment was repeated two more times to give an understanding of the variability of results.

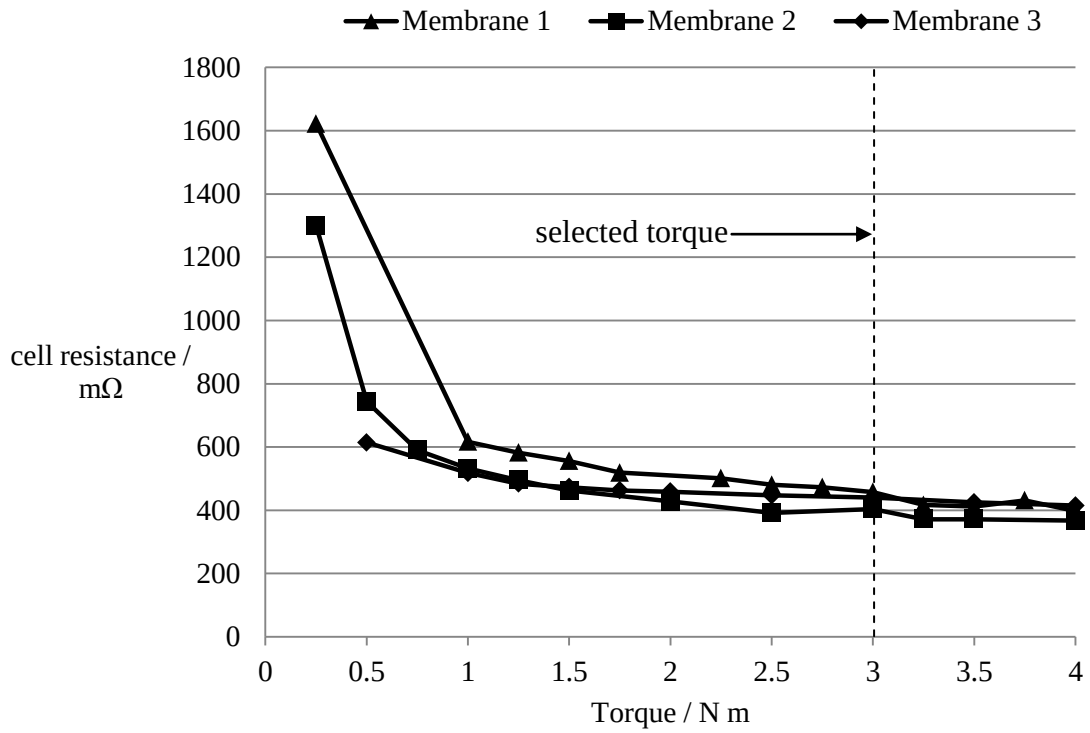

Figure 4-1 Relationship between the torque applied on the alkaline polymer electrolyser cell and the resulting cell resistance, with a Surrey JK80L polymer electrolyte membrane at a temperature of 25°C and with pure DI water circulating

Figure 4-1 shows that as the torque increased there was a reduction in contact resistance, most likely from the increasing number of conductive surface sites that were being pressed against the membrane. Above 1 N m, the decrease in resistance shows a more linear relationship with respect to torque. A higher torque lead to lower ohmic resistance, increased electrical conductivity and improved performance of the electrolyser. Conversely, a higher torque led to problems with short circuiting, as the membrane was occasionally punctured due to the mechanical forces applied to its surface. The difference in resistance between 3 and 4 N m was approximately 15% yet the chances of puncture was significantly increased at 4 N m. Thus all electrochemical operation of the polymer electrolyser cell was conducted at a torque level of 3 N m to provide a balance between performance and reliability.

The variance in measurements was as high as +/-50 mΩ. This could be due to slight differences in the thickness of the membranes or more likely the different exposure times of the membrane to the carbon dioxide in the air prior to cell assembly. This was a factor that was practically challenging to control. It could also be due to the

variation in the quantity of contaminants in the NaOH used for conversion of the membrane's head groups and any inaccuracy of the torque wrench used for cell assembly. The cell resistance was also be affected by the hydration of the membrane that was influenced by the time taken to utilise the torque wrench to compress the components.

4.2.2 Effect of time

Figure 4-2 shows the effect time has on the cell resistance. EIS measurements were taken whilst continuing to circulate fresh DI water, maintaining the cell at 25°C and holding the cell at a torque of 3 N m.

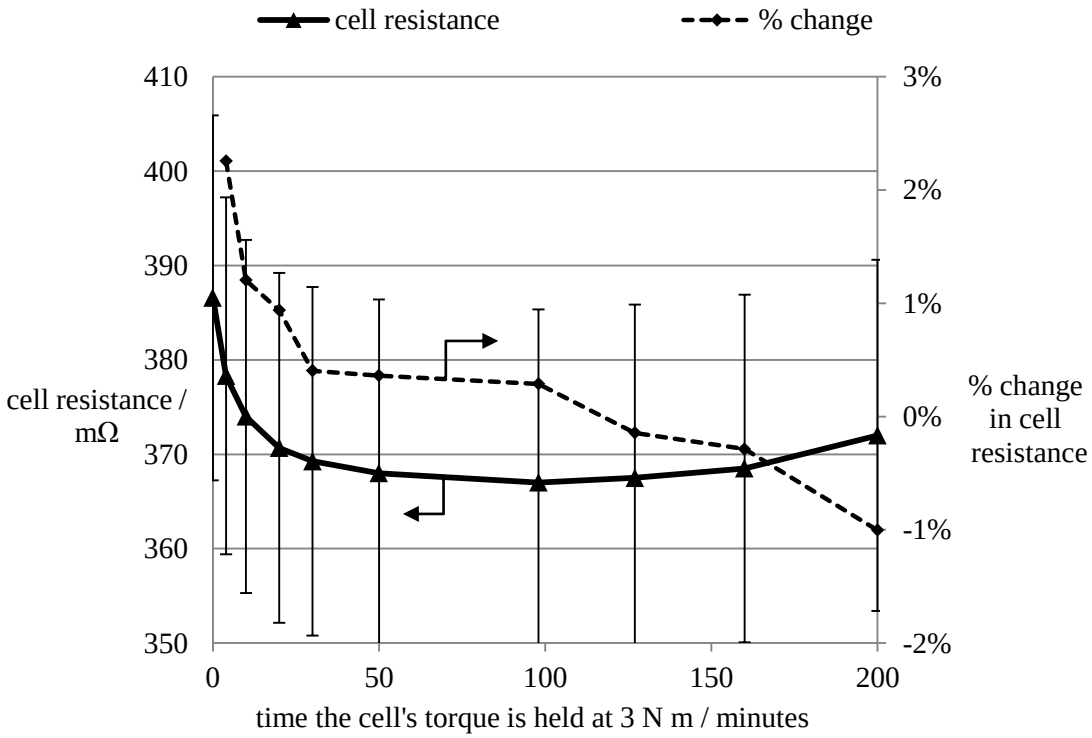

Figure 4-2 Change in polymer electrolyser cell's resistance over time with a Surrey JK80L membrane held at 3 N m and with circulation of pure water at a temperature of 25°C

The chart shows that the cell achieved a steady value of 370 mΩ for its resistance after approximately 25 minutes and changes beyond this time are less than 1%. The bars on the line for cell resistance represent errors of +/- 15 mΩ and this embodies the range of resistances when subsequent membranes were prepared and tested in the same manner. After approximately 150 minutes all membranes showed signs of an increase in the resistance due to a decrease in ionic conductivity across the membrane. This was most likely due to a build up of contaminants in the pores of the membrane. These contaminants could include carbonates that have been formed from any exposure of the membrane to the atmosphere prior to, and during assembly of, the cell. Despite being purified, DI water also contains small quantities of bacteria, and it will pick up further contaminants during transfer of the water to the electrolyser cell from within containers and pipe work.

4.2.3 Effect of the high purity hydroxide conversion

The previous investigation in section 4.2.1 was concerned with preparation of the solid polymer electrolyser with a membrane that had been prepared from 98%+ purity anhydrous NaOH pellets (Sigma-Aldrich). According to the product specification sheet the pellets contain ≤ 1.0% of Na_2CO_3 as an impurity and this value would increase with aging and any exposure of the pellets to the atmosphere.

Due to the carbonation problems discussed in section 1.4.6, an investigation was made into the use of a source of OH^- ions that did not include carbonates. KOH pellets (Sigma-Aldrich), with a composition of > 85% KOH and 15% water, have a purity of > 99.99%. According to the product specification sheet the impurities include trace metals of calcium, copper, iron, titanium, sodium and rubidium < 500 ppm basis. There is no mention of carbonates as an impurity although it can be assumed that trace amounts exist from any exposure to the atmosphere.

Figure 4-3 shows a comparison of cell resistances with the two preparation solutions: one with a Surrey membrane prepared with high purity KOH and another Surrey membrane with impure NaOH. Both conversions take place with 1 molar concentrated solutions for one hour, being replaced with fresh solution every 20 minutes. Immediately after conversion the membranes are thoroughly rinsed with DI water, then assembled in the polymer electrolyser cell with the GDLs shown in Figure 2-14 and torqued to 3 N m. Pure DI water is circulated through the polymer electrolyser at a temperature of 25°C.

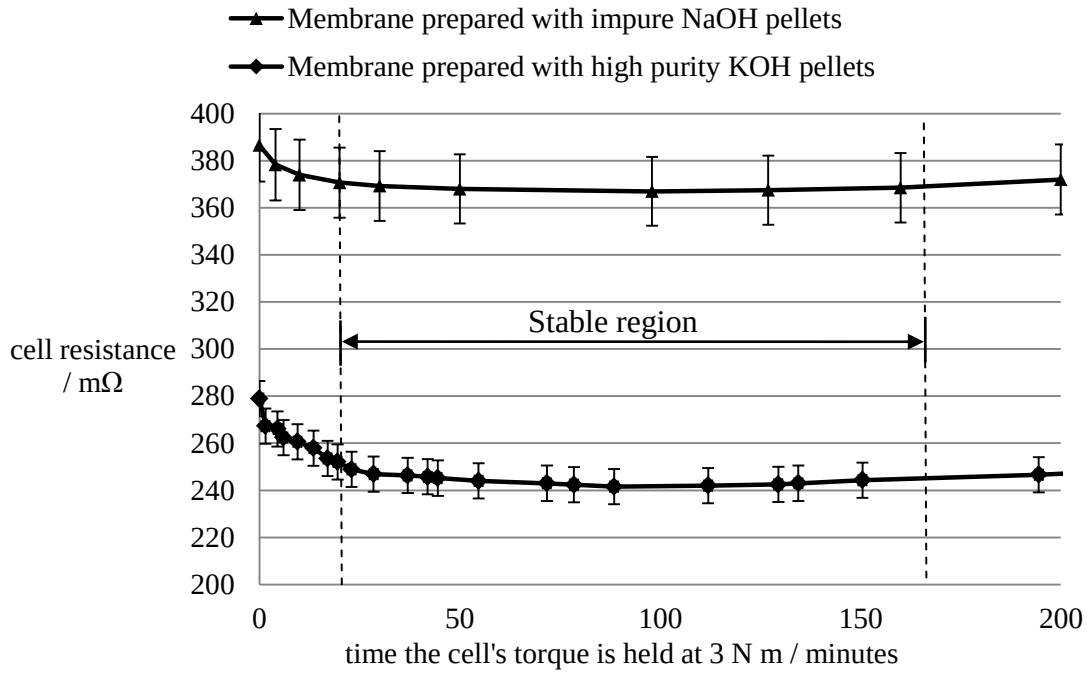

Figure 4-3 Influence of the purity of hydroxide ions on the polymer electrolyser cell's resistance

The chart shows a decrease of approximately 100 mΩ in the cell resistance with a membrane prepared with high purity KOH compared with impure NaOH pellets. The lowest resistance reached is 242 mΩ after 100 minutes on the KOH.

At low concentrations, below 10%, both KOH and NaOH have similar conductivities under standard conditions. The conductivity of 1 M NaOH is approximately 190 mS cm^{-2} and for 1 M KOH it is 215 mS cm^{-2} for KOH. This represents a 13% improvement in conductivity with KOH based on standard conditions, than

compared to NaOH, however the improvement in cell resistance in Figure 4-3 is approximately 50%. The high purity KOH preparation procedure produced a cell resistance of over 100 mΩ less than the procedure which used the impure NaOH. The bars embody the range of resistances in repeated experiments. They advocate that a more consistent cell resistance is achieved with KOH, as variation between resistances produced with membranes prepared with KOH is +/-8 mΩ compared with +/-15 mΩ for membranes prepared with NaOH. This shows that the quality of the hydroxide pellets used for preparation of an anion exchange membrane is important for consistent and reliable results.

It appears as though membranes prepared with either high purity KOH or impure NaOH begin to show sign of increased ionic resistance after approximately 125 minutes. Assuming the hydration state of the membranes was the same, the rate of their increase in resistance is similar and this suggests that any cause of the resistance must arise from impurities accumulating from the circulated DI water. The steady increase in resistance of 3 mΩ, between 150 and 200 minutes of operation and for membranes prepared through both methods, is within error but this may be a concern for long term stability (> 200 minutes).

4.3 α-$Ni(OH)_2$ and $4Ni(OH)_2$•NiOOH•xH_2O catalyst and pure DI water

Nickel hydroxide nanopowder was synthesized through the chemical bath deposition method detailed in section 2.4.3. A catalyst ink, prepared with the α-$Ni(OH)_2$ / $4Ni(OH)_2$•NiOOH•xH_2O particles and 35% PVBC/PVC, was airbrushed with purified nitrogen gas directly onto the Surrey membrane at 60°C with a loading of 0.8 mg cm^{-2}. The cathode layer contained 0.5 mg Pt cm^{-2} and was airbrushed onto Freudenberg H2315 C2 carbon cloth under the same conditions. The anion exchange membrane was converted to OH^- form with high purity KOH solution then assembled in the cell which was torqued to 3 N m. Pure DI water was circulated and the cell was maintained at 25°C. The cell resistance was measured using EIS periodically and this is shown in Figure 4-4.

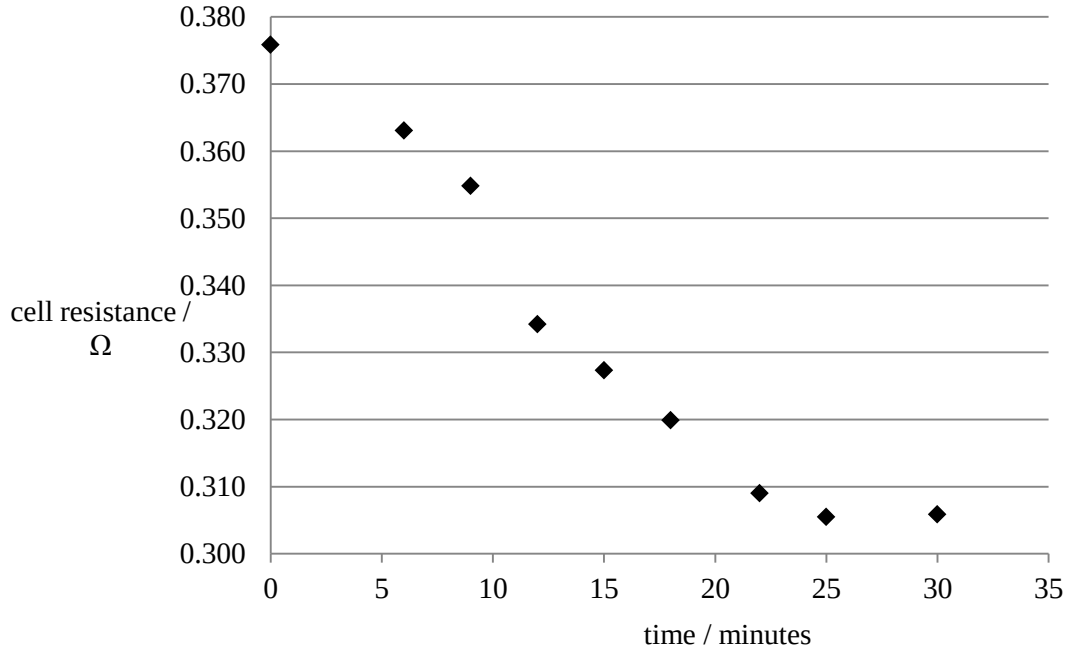

Figure 4-4 Anion exchange membrane polymer electrolyser cell resistance with 0.8 mg α-$Ni(OH)_2$ / $4Ni(OH)_2$•NiOOH•xH_2O cm^{-2} and 35% PVBC/PVC on a Surrey membrane with pure DI water circulated at a temperature of 25°C

Figure 4-4 shows the resistance initially at 0.376 Ω which decreased until after 25 minutes when the resistance stabilised at 0.305 Ω. A final measurement was made after 30 minutes to confirm the resistance had stabilised. The resistance follows the same behaviour as that in Figure 4-3, which proves that the catalyst film is stable in the system under ambient operating conditions.

4.3.1 Cycling

Electrochemical assessment of the MEA began through cyclic voltammetry between 1.2 V (just prior to the theoretical onset for oxygen evolution) and 2.0 V (a typical operation potential for a commercial electrolyser). This is shown in Figure 4-5.

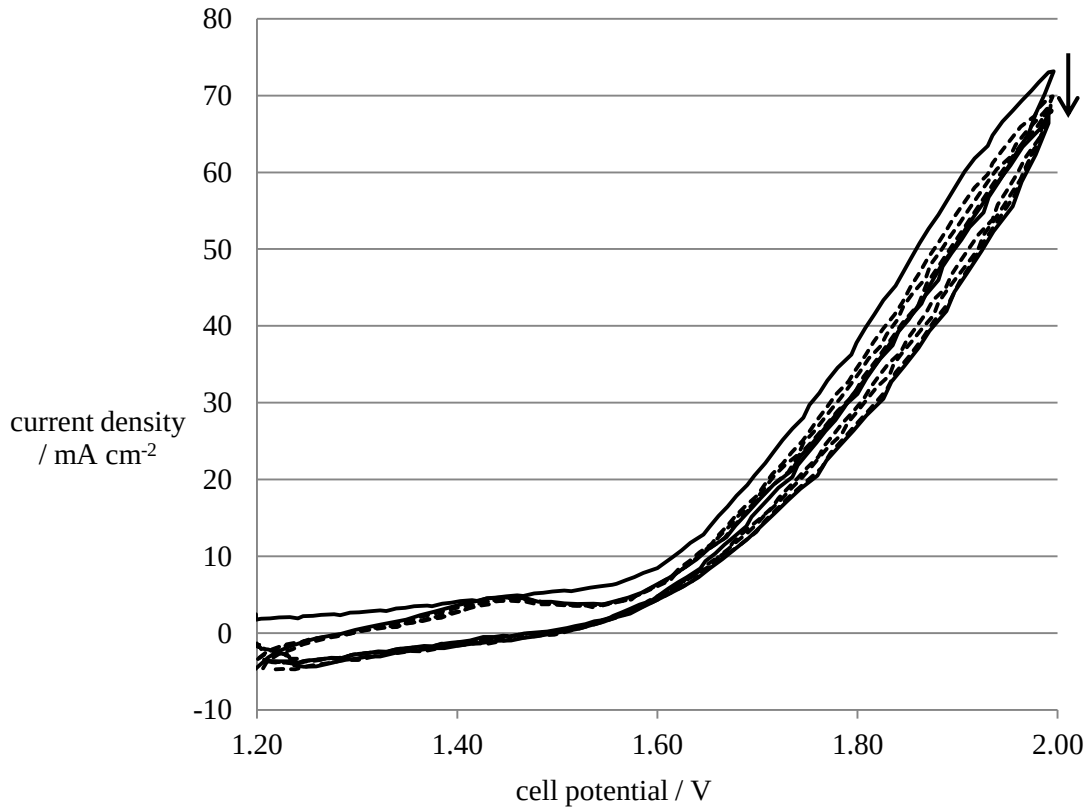

Figure 4-5 Cyclic voltammetry on α-$Ni(OH)_2$ / $4Ni(OH)_2$•NiOOH•xH_2O (35% PVBC/PVC) catalyst on the anode side of a anion exchange membrane polymer electrolyser with pure DI water at a temperature of 25°C and a scan rate of 30 mV s^{-1}

The response of the electrode shows similarities and differences compared to the results produced by the same catalyst in the glass half cell electrolyser, which was shown in Figure 3-24. The average potentials of the peak data for α-$Ni(OH)_2$ / $4Ni(OH)_2$•NiOOH•xH_2O from the glass half cell electrolyser experiments are shown in Table 4-1.

Table 4-1 Anodic peak data for α-$Ni(OH)_2$ / $4Ni(OH)_2$•NiOOH•xH_2O in the polymer electrolyser (DI water) cell and in the glass half cell electrolyser (1 M NaOH) at a temperature of 25°C

Cell (electrolyte)	E_{pa}	E_{pc}	ΔE
Glass half cell electrolyser (1 M NaOH)	1.456	1.266	0.19
Alkaline polymer electrolyser (DI water)	1.44	1.24	0.20

The peak potentials show similarity which implies that the nickel hydroxide couple is present in both systems. However the voltammetric charge associated with the peak area in the polymer electrolyser system is notably smaller, even when taking into consideration the catalyst loading.

The difference in environments that the catalyst films experience in the two systems is primarily the pH of the solution in contact with the catalyst layers and the polymer electrolyte. The reduction in concentration of OH^- ions in the alkaline polymer electrolyser system had an effect on the utilisation of active species in the catalyst film and is directly reducing the number of reactions (described by Equation 1-4) taking place at the electrode's surface.

4.3.2 Steady state response

The steady state current response of the electrode was achieved by performing cyclic voltammetry between 1.2 and 2.0 V at a scan rate of 0.5 mV s^{-1}. This was conducted with the circulation of pure water at 25 and 40°C and the result is shown in Figure 4-6.

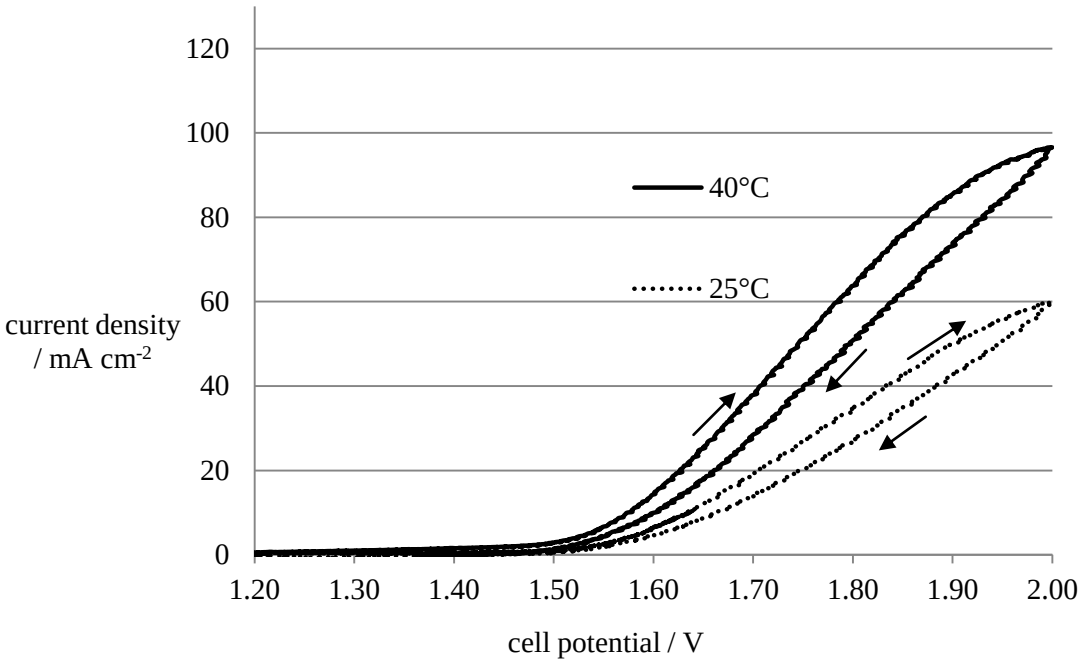

Figure 4-6 Temperature effect on the steady state current response of α-$Ni(OH)_2$ / $4Ni(OH)_2$•NiOOH•xH_2O electrodes in a polymer electrolyser, during electrolysis of pure water at temperatures of 25 and 40°C and a scan rate of 0.5 mV s^{-1}

There is no noticeable activity from the electrode until the onset for oxygen evolution at 1.48 V. The current response curves show deviation from linearity at potentials approaching 1.8 V. Extrapolation from the linear section of the current response indicates current density values of 66 and 116 mA cm^{-2} for temperatures of 25 and 40°C respectively. The actual current densities achieved were 60 and 87 mA cm^{-2}. This deviation from linearity could be an indication of mass transport issues as bubbles may not be efficiently removed from the surface of the electrode after they have been produced. Furthermore, the difference in current densities for the cathodic going sweep indicates that the surface of the catalyst film has changed. Most likely the nickel hydroxides have been transformed to less stable and less electrochemically active forms of nickel hydroxide.

Despite the deposition method of airbrushing the catalyst film onto the surface of the membrane, and the inclusion on an ionomer into the catalyst layer, the current densities produced are much lower than the α-$Ni(OH)_2$ / $4Ni(OH)_2$•NiOOH•xH_2O in 3.6.3, even at higher potentials. The active surfaces of the catalyst particles are not being utilised due to a less effective triple contact between the electrode, electrolyte and catalyst. The primary reason for this must be the lack of OH^- ions in the DI water. The DI water has reduced the number of hydroxide ions in contact with the surfaces of the nickel hydroxides which is reducing the voltammetric charge and the current densities.

4.3.3 Stability of α-$Ni(OH)_2$ and $4Ni(OH)_2$•NiOOH•xH_2O

The stability of α-$Ni(OH)_2$ / $4Ni(OH)_2$•NiOOH•xH_2O in DI water was assessed by holding the potential at an operational value of 1.8 V and the resulting current density is shown in Figure 4-7.

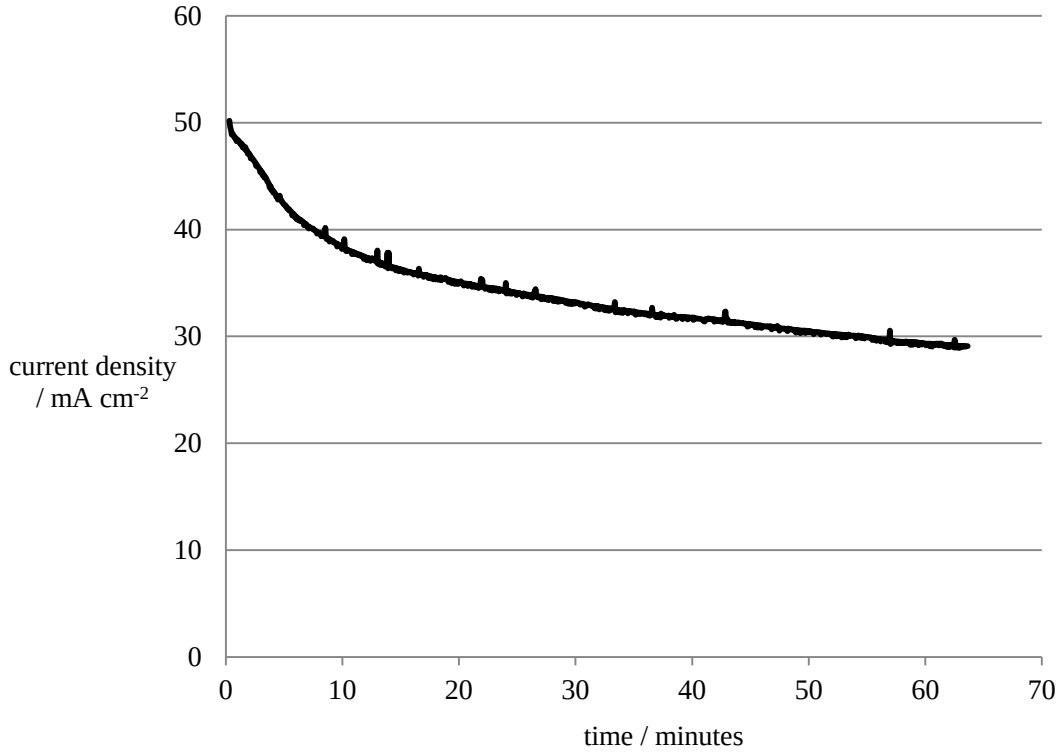

Figure 4-7 Instability of electrode with α-$Ni(OH)_2$ / $4Ni(OH)_2$•$NiOOH$•xH_2O and 35% PVBC/PVC in an alkaline polymer electrolyser with circulation of pure DI water at a temperature 25°C and a potential of 1.8 V

Initially there was a rapid drop in current density, which is followed by a slower rate of 0.1 mA min^{-1}. During the time period for these experiments, the membrane was proven to be stable in terms of its resistance (see Figure 4-3) therefore the reduced current density must be attributed to changes in the catalyst layer. It is unlikely that carbon entered the system and formed carbonates within the catalyst layer or ionic pores of the anion exchange membrane. Investigation followed to see how $NiCo_2O_4$ would behave during electrolysis of pure DI water.

4.4 $NiCo_2O_4$ (280) catalyst and pure DI water

The $NiCo_2O_4$ (280) catalyst synthesized as described in section 2.4.4 was made into a catalyst ink containing an ionomer mixture of PVBC and PVC (35% of catalyst mass and a PVBC:PVC ratio of 5:1) in a THF solvent. This was airbrushed onto a Surrey JK80L membrane at 60°C with a loading of 1.6 mg cm^{-2} to form the anode. For the cathode, platinum black was sprayed onto a carbon GDL (Freudenberg H2315 C2) with the same ionomer mixture as the anode and with a loading of 0.5 mg cm^{-2}. The MEA was mechanically pressed with a torque of 3 N m and DI water was circulated at a temperature of 25°C. The resistance of the system stabilised at 326 mΩ.

4.4.1 Cycling

An electrochemical study was made on the catalyst by cycling the potential in the anodic regions and is shown in Figure 4-8.

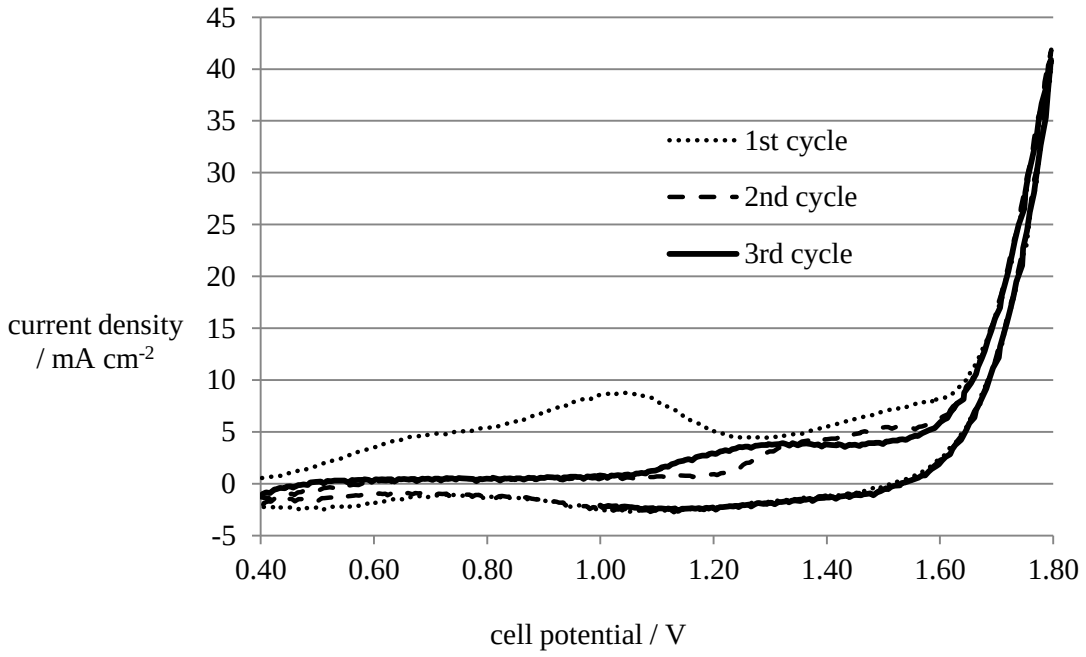

Figure 4-8 Cyclic voltammetry on $NiCo_2O_4$ (280) catalyst deposited on the anode with 35% PVBC/PVC, in the anion exchange membrane polymer electrolyser with DI water at temperature of 25°C and a scan rate of 30 mV s^{-1}

The anodic peaks are associated with charge of the catalyst layer involving the exchange of protons with the solution and phase transition, according to the following reaction [107]:

$$NiOOH + 2CoOOH + 2H^+ + 2e^- \rightarrow Ni(OH)_2 + 2Co(OH)_2 \qquad \textbf{Equation 4-1}$$

According to Guerrini [102] the phrase transition has an effect on the properties of the surface of the electrode. However the cycles in Figure 4-8 suggest that there is a deficiency of hydroxyl ions for the redox reactions to take place, which is pushing the peak potentials higher and reducing the peak areas and voltammetric charge. This is in accordance with the Nernst equation in Appendix B that has been customised for this particular reaction in Equation 4-2.

$$E = 1.229 + 0.013 \times ln\frac{[NiOOH]^a[CoOOH]^b}{[Ni(OH)_2]^c[Co(OH)_2]^d} \qquad \textbf{Equation 4-2}$$

The Nernst equation links an electrodes potential to the bulk species concentrations and shows that at each potential of a working electrode there is a specific value of the ratio between $[Ox]$ and $[Red]$. Literature bases the reaction schemes of nickel cobalt oxide films to include the exchange of protons, hydroxyl ions, alkali metal cations and water [108], which can also explain the shift of the peaks from the CVs in the high pH environment in Section 3.8 to that of a low pH (low OH^- concentration) environment in Figure 4-8. This reduced the activity of the catalyst film towards oxygen evolution at higher potentials as shown in Appendix J. The inclusion of high pH into the polymer electrolyser will now be discussed.

4.5 $NiCo_2O_4$ (280) catalyst and 1 M KOH

This section is concerned with operation of the electrolyser in a high pH (pH = 14) environment followed by a lower pH (pH = 7). The MEA was a Surrey JK80L membrane with catalyst layers prepared by airbrushing 0.7 mg cm^{-2} $NiCo_2O_4$ (that had been thermally treated at 280°C) on the anode and 1.0 mg cm^{-2} $NiMoO_4$ on the cathode. Conversion of the membrane to the OH^- conducting form was done after it had been assembled in the cell and with 1 M KOH prepared high purity KOH pellets. The KOH was circulated through the electrolyser in a sealed environment, which would minimize exposure to atmosphere and reduce the carbonation issues discussed in section 1.4.6.

4.5.1 Resistances of cell during conversion of membrane

Whilst maintaining the cell at a temperature of 25°C the following measurements were recorded by EIS over a period of time and this is shown in Figure 4-9.

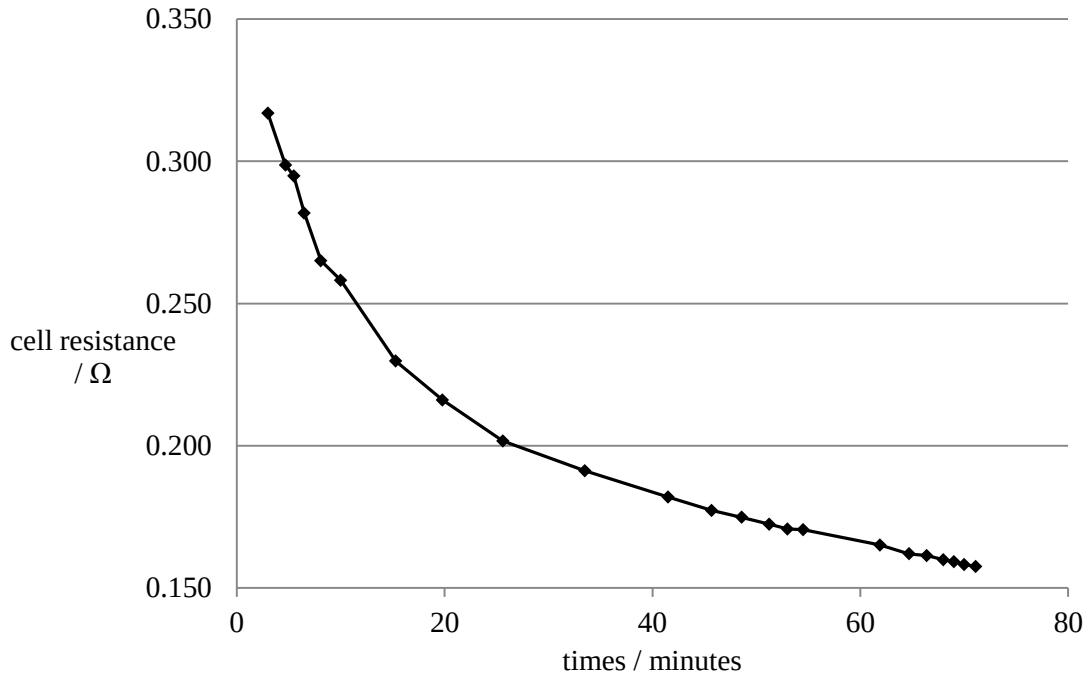

Figure 4-9 Cell resistance during conversion of the Surrey JK80L membrane to hydroxide form with 1 M KOH solution at a temperature of 25°C

Initially the resistance drops sharply at a rate of -10 mΩ min^{-1}. After 10 minutes this rate is at -5 mΩ min^{-1} and gradually reduces until after 60 minutes where the resistance drops at a rate of -0.5 mΩ min^{-1}. The resistance of the electrolyser with 1 M KOH in the polymer electrolyte is approximately 150 mΩ less than resistances experienced with DI water.

4.5.2 Performance of $NiCo_2O_4$ (280) catalyst with 1 M KOH towards the oxygen evolution reaction

After conversion of the membrane, the cell was flushed with fresh 1 M KOH solution whilst being held at a temperature 25°C. The steady state current response of the system is shown in Figure 4-10 and compared to an polymer electrolyte with DI water.

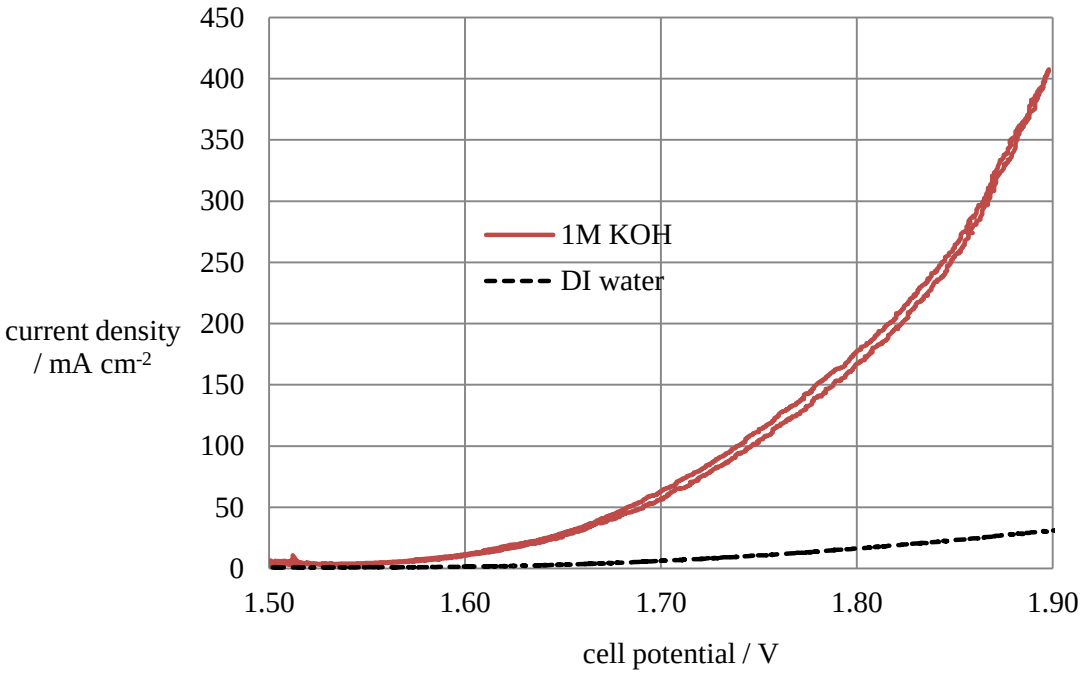

Figure 4-10 Effect of electrolyte on the steady state current density response of $NiCo_2O_4$ (280) in the polymer electrolyser at a temperature of 25°C

The catalyst shows a stable performance of 0.4 A cm^{-2} at 1.9 V (energy efficiency of 54.6%). The short term stability of the MEA was assessed by holding at the operational potential of 1.9 V, whilst continuing to circulate 1 M KOH at 25°C. The current density produced is shown in Figure 4-11.

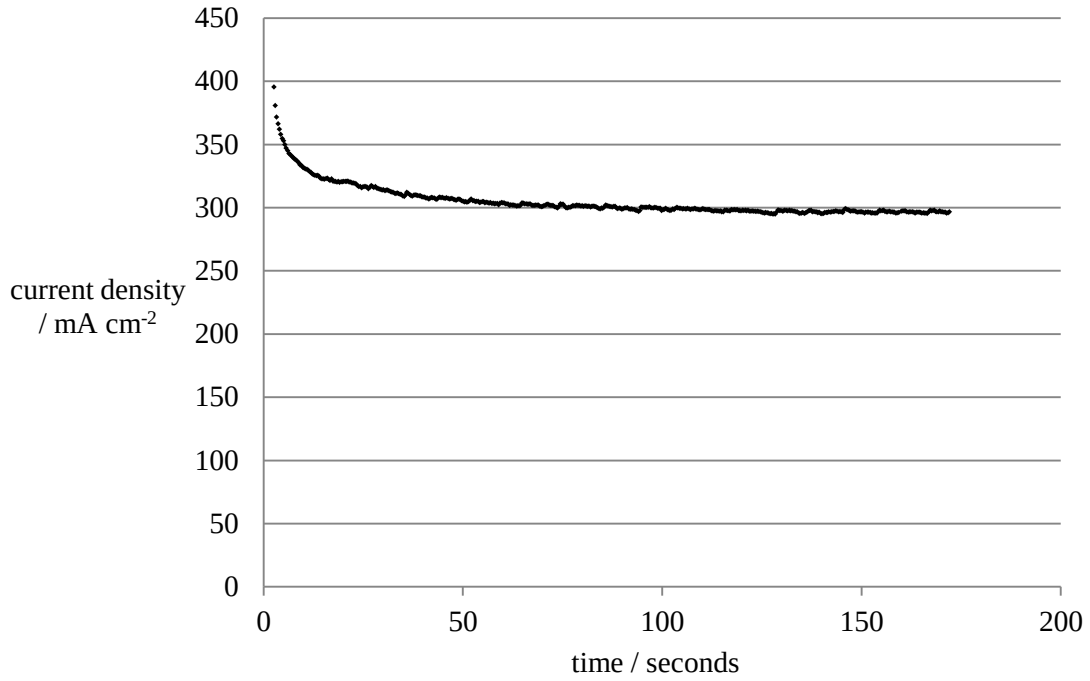

Figure 4-11 Stability of an MEA containing 0.7 mg cm^{-2} $NiCo_2O_4$ (280) with 35% PVBC/PVC at a potential of 1.9 V, with an electrolyte of 1 M KOH at a temperature of 25°C

After one minute of operation the current density was 0.3 A cm^{-2} ±5 mA and remained within this error for a further two minutes of operation.

4.5.3 Performance drop with pure water

Switching the fuel supply from 1 M KOH to DI water is shown in Figure 4-12

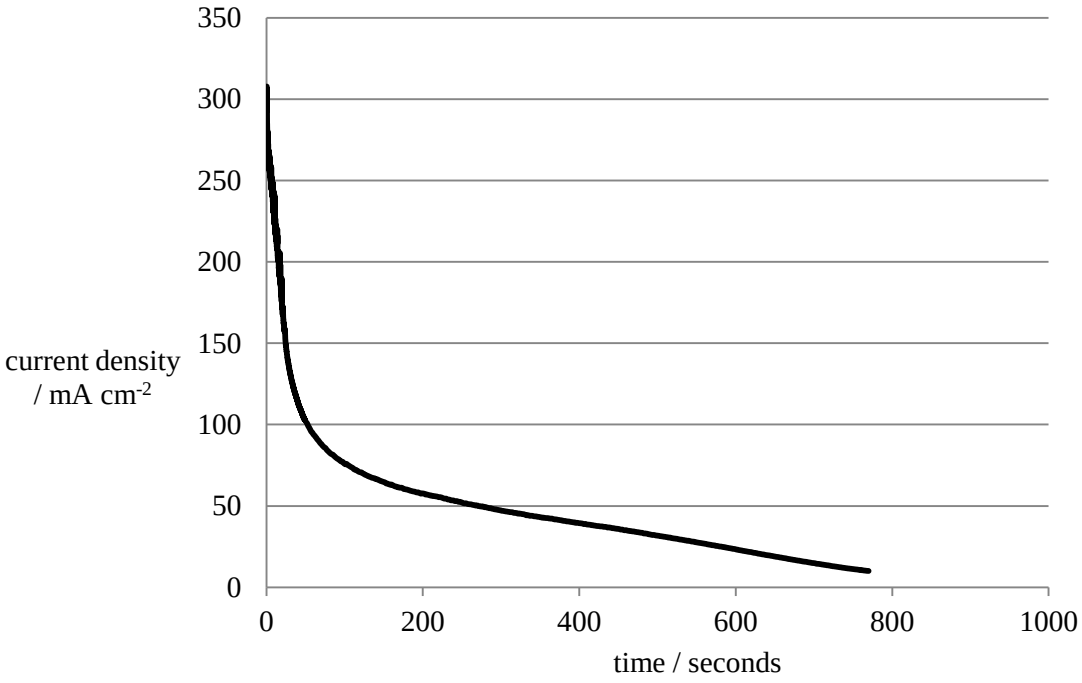

Figure 4-12 Anion exchange membrane electrolyser current density for $NiCo_2O_4$ (280) with the fuel supply switched from 1 M KOH to DI water; temperature of 25°C and E_{cell} = 1.9 V

Immediately after the DI water was introduced to the cell there was a rapid decrease in performance of the electrolyser. After almost 800 seconds of operation the potentiostat was switched off and an EIS measurement gave the resistance of the cell to be 0.785 Ω. This increase in resistance indicates a change to the system associated with the MEA. The study in section 4.2.3 indicates that the membrane shows high stability in the system, therefore resistances must be attributed to changes within the catalyst layer. This could include degradation of the ionomer at the high potential that has been applied although more likely it is oxidation of the catalyst.

The overall reaction for oxygen evolution (see Equation 1-4) at the anode involves OH^- ions as reactants, which are of high abundance in an alkaline electrolyte. It is possible that there is electrochemical migration of OH^- ions to the surfaces of the catalyst and they could be acting as promoting agents. For pure DI water the

concentration of OH^- ions is 10^{-7} M so without these promoting agents the oxygen evolution reactions are not proceeding.

4.6 Conclusions of the alkaline polymer electrolyser results

The research enabled the design, construction and operation of an alkaline polymer electrolyte water electrolyser working with only pure water and non precious metal catalysts.

The resistance of the polymer electrolyte was influenced by the selection of materials employed in the MEA, the method of preparation of these materials and assembly of the anion exchange membrane in the electrolyser. Various configurations of membrane electrode assemblies were investigated. As shown in Figure 2-14 a suitable arrangement for the anode side of the MEA was found to be a gold plated titanium mesh pressed against the catalyst film that was sprayed on the anode side of the anion exchange membrane. On the cathode side a gold plated metal titanium mesh was pressed against a carbon paper gas diffusion layer which had been hydrophobically treated.

It was found that a torque of 3 N m presented sufficient balance between performance and reliability of the membrane. Far greater ionic conductivity and stability of the membrane was achieved when conversion to the hydroxide conducting form took place after assembly of the cell. The use of carbonate-free hydroxide solution also achieved reduced resistances in the polymer electrolyte. Circulation of DI water through the anode and cathode for 25 minutes, prior to electrochemical operation of the electrolyser, aided to hydrate the membrane and decrease the ohmic resistance in the cell prior to operation.

The catalyst α-$Ni(OH)_2$ / $4Ni(OH)_2$•NiOOH•xH_2O, produced through the CBD procedure (section 2.4.3), showed much lower performances with pure DI water than with the 1 M KOH electrolyte in the half cell. The environment of pure DI water has reduced the concentration of OH^- ions in the alkaline polymer electrolyser system and directly affected the utilisation of active species in the catalyst film. This directly reduced the reactions (described by Equation 1-4) taking place at the electrode's surface. The catalyst also showed reduced electrochemical stability in low [OH^-] of

the alkaline polymer electrolyser compared to high $[OH^-]$ in the glass half cell electrolyser as nickel hydroxides were transformed to less stable and less electrochemically active forms of nickel hydroxide (section 4.3.3). Similar catalyst layer instability was shown when the catalyst $NiCo_2O_4$ (280) experienced a low $[OH^-]$ during electrolysis of pure DI water.

5 Main conclusions and recommendations for future work

5.1 Conclusions

An investigation was made into the development of non-noble catalysts for hydrogen and oxygen evolution in alkaline polymer electrolyte membrane electrolysis. The following materials were identified, according to the prerequisites set out by Trassati in section 1.6, as promising electrocatalysts for the oxygen evolution reaction: NiO, nickel hydroxides, and $NiCo_2O_4$.

The catalyst NiO was synthesized through thermal decomposition (section 2.4.1), solution growth method followed by thermal decomposition (section 2.4.2), and a chemical bath deposition procedure (section 2.4.3), whose performances were compared against a commercial form of NiO particles. The nickel hydroxides, α-$Ni(OH)_2$ / $4Ni(OH)_2 \bullet NiOOH \bullet xH_2O$, were synthesized in the chemical bath deposition procedure without any thermal treatment. $NiCo_2O_4$ was synthesized through thermal decomposition of a mixture of nickel and cobalt nitrate salts (section 2.4.4). For the hydrogen evolution reaction, the electrocatalyst $NiMoO_4$ was identified and synthesized through a co-precipitation method (section 2.4.5).

The suitable electrode material for employment in the glass half cell electrolyser was found to be titanium (section 2.3.2). It was found necessary to pretreat the surface of the metal, prior to electrocatalyst deposition, according to the procedure shown in section 2.3.5. Following pretreatment, and for the thermal decomposition and chemical bath deposition methods, catalyst films could be prepared directly onto the electrode surfaces with a strong enough mechanical stability for oxygen evolution to take place. The electrochemical studies on these pure catalyst films (see sections 3.4.1 and 3.6.1) showed they had strong activity towards oxygen evolution. When catalysts were prepared in nano-powder form a formulation of a catalyst ink was required with a PVDF additive to enable the catalyst film to maintain mechanical

strength during operation of the glass half cell electrolyser. Section 2.4.6 shows that a minimum of 25 wt% of the polymer PVDF was required for mechanical stability of the catalyst film during oxygen evolution conditions. Furthermore, the ink deposition method required the titanium electrodes to be first coated in a thin film of gold to enable electrical conduction between the titanium and the catalyst film (section 2.3.2); otherwise an electrically insulating layer of TiO_2 was formed. This enabled further investigation of the catalysts synthesized into nano-particle form.

For the oxygen evolution reaction, the catalyst with the highest mass activity was that of a NiO film formed through the chemical bath deposition, followed by thermal decomposition method in section 3.6. It produced 56.4% of the mass activity of an electrode deposited with an IrO_2 catalyst film in the same system. This can be attributed to its highly porous structure synonymous with the synthesis procedure (Figure 3-16) that also limited the loading of the catalyst to 0.30 ± 0.05 mg NiO cm^{-2} (see Figure 3-14).

Higher loadings of NiO, which had been synthesized from the chemical bath deposition method, were achieved through utilisation of catalyst inks with 25 wt% PVDF binder. However the highest performance achieved (34 ± 2 mA cm^{-2} with 1.1 mg NiO cm^{-2}) was only 50% of the performance achieved from thin films without any PVDF additive (68 ± 2 mA cm^{-2} with 0.3 mg NiO cm^{-2}) (see Figure 3-23). One cause for this performance drop could be due to the low porosity of the catalyst film formed from catalyst inks as opposed to a direct formation of a porous film formed from chemical bath deposition. The performance drop can also be attributed to the PVDF additive that is not electrochemically active and merely acts as a binding agent.

For the oxygen evolution reaction the highest current densities achieved in the glass half cell electrolyser were from a blend of α-$Ni(OH)_2$ / $4Ni(OH)_2$•NiOOH•xH_2O that was synthesized through the chemical bath deposition method and had not been thermally treated (Figure 3-28), and $NiCo_2O_4$ (280) which was thermally treated at 280°C for one hour (Figure 3-34). However under electrolysis of pure DI water in

the alkaline polymer electrolyser, these catalysts produced much lower current densities even when pushed to higher overpotentials.

Utilising pure DI water was the main contributory factor towards degradation in the catalyst layers, due to instability of the nickel based catalysts at the potentials applied. Inclusion of 1 M KOH into the polymer electrolyser aided to reduce resistances and pushed up performances of the $NiCo_2O_4$ (280) catalyst. With $NiCo_2O_4$ (280) on the anode and $NiMoO_4$ on the cathode a current density of 0.4 A cm^{-2} was achieved by the alkaline polymer electrolyser at a potential of 1.9 V and with an electrolyte of 1 M KOH circulating at a temperature of 25°C. The current output is at an acceptable value for the performance of modern electrolysers. Especially since the catalyst layers were free from noble metals although instability is a limitation of the system.

5.2 Recommendations for future work

The high mass activity of electrocatalyst films produced by the chemical bath deposition should be investigated further within alkaline polymer electrolysers and the following recommendations are made for future work:

- Modification of the MEA in the alkaline polymer electrolyser to incorporate porous films produced by CBD
    - This can be achieved through incorporation of nickel foam as the GDL instead of gold plated mesh
- Chemical bath deposition onto nickel foam
- Investigation into the possibility of chemical bath deposition of films directly onto anion exchange membrane surfaces
- Investigate plausibility of mixed metal oxide CBD
- Investigate SILAR (successive ionic layer adsorption and reaction) method
    - theoretically build up a catalyst layer one monolayer at a time
    - eliminate bulk precipitation
- Improve the stability of the nickel based catalysts with the addition of other element such as cobalt, copper or chromium. Recent studies by Jia et al [109] and Wu et al [48] have shown that the catalyst $Cu_{0.3}Co_{3-x}O_4$ exhibits much greater stability than nickel as the copper atoms help prevent the cobalt from being reduced to Co metal or $Co(OH)_2$.
- Investigate operational potentials < 1.8 V with pure DI water

Appendices

A. Market value of transition metals

B. Kinetics of electrode reactions

The Nernst equation links an electrodes potential to the bulk species concentrations.

$$E = E_0 + \frac{RT}{nF} ln \frac{[Ox]}{[Red]} \qquad \textbf{Equation 5-1}$$

The equation shows that at each potential of a working electrode there is a specific value of the ratio between $[Ox]$ and $[Red]$

C. Peak surface areas

The peak surfaces areas were calculated using Origin Pro. The boundaries are identified below in Figure 5-1.

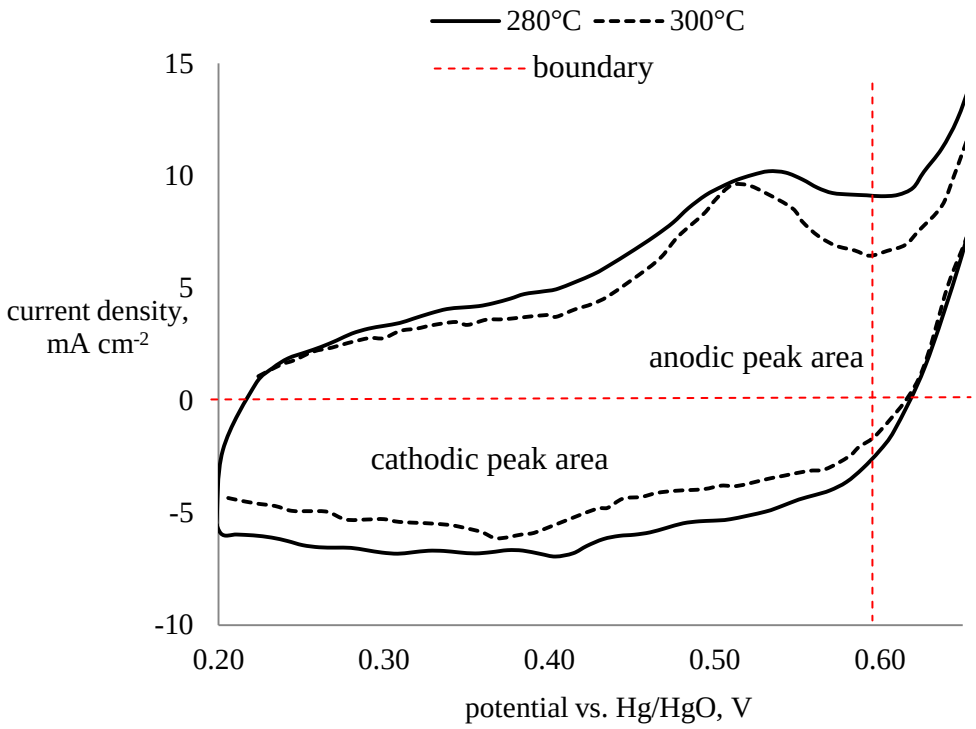

Figure 5-1 Peaks from $NiCo_2O_4$ electrodes, in 1 M NaOH at a temperature of 25°C at a scan rate of 30 mVs^{-1}, identifying the boundaries for the peak area calculations

The anodic peak area was taken at positive current densities up to 0.6 V vs. Hg/HgO. The cathodic peak area was taken at negative current densities up to 0.6 V vs. Hg/HgO. The same method was applied for the peak calculations of NiO in section 3.6.1 and nickel hydroxides in section 3.6.3.

D. Preparation of catalyst layer on membranes

Airbrushing a catalyst film onto a membrane is a practical method of achieving a homogenous film. The airbrush atomises the spray, allowing for a more homogenous film than the ink droplets used in glass half cell electrode preparation. Depositing onto a membrane at an elevated temperature allowed the solvent to evaporate, leaving behind a film of catalyst/ionomer/binder. The preparation of this film requires an excess of catalyst which can be calculated from Equation 5-2.

$$\begin{aligned} &\text{total mass of catalyst required } (mg) \\ &\quad = \text{desired loading}(mg\ cm^{-2}) \times \text{spraying surface area}(cm^2) \\ &\quad \times \text{waste factor} \end{aligned}$$

Equation 5-2

The water factor is employed to compensate for ink losses that are inevitably experienced from the preparation procedure. Primary losses include:

- Retention of ink in the spray gun
- Loss to atmosphere upon spraying
- Film deposited outside of the boundary of the spray area

The waste factor is dependent upon the size and shape of the area intended for the deposition to take place, and also upon the individual's technique. Therefore it can only found though trial and error of spray procedure. If the desired catalyst loading is not achieved then the waste factor must be increased to compensate for the losses experienced. If the loading is too high then the waste factor must be reduced.

E. Hydrogen Production

The decomposition of water is the reverse of the process of hydrogen combustion. Consequently the theoretical amount of energy required, per unit quantity of hydrogen produced, is equal to the heat of combustion. A single hydrogen molecule is formed by the addition of two electrons to two hydrogen ions in solution. The relationship between the rate of electron flow, i.e. the current passed, and the rate of hydrogen produced is given by Faraday's Law.

$$Hydrogen\ production(mols^{-1}) = \frac{I}{nF} \qquad \textbf{Equation 5-3}$$

Where, I is the operational current, n the number of electrons transferred and F is Faraday's constant or charge on a mol of electrons (96,485 Coulombs $mole^{-1}$).

The relationship assumes that all electron flow goes into the desired electrode reaction of hydrogen evolution, i.e. current efficiency is 100%. With pure water there should theoretically be no extraneous electrode reactions. In practice the current efficiencies in most hydrogen generators approach 100%, but do not reach it, because in water electrolysis other reactions are possible, such as oxygen reduction and hydrogen oxidation.

F. Oxygen evolution reaction on uncatalysed titanium foil substrate

Titanium foil electrodes, with a geometric area of 1 cm x 1 cm, were pretreated according to section 2.3.5, and then cycled between 0.6 and 1.2 V vs. Hg/HgO at 20 mV s^{-1} in 1 M NaOH at 25°C. Figure 5-2 shows the instability of the scans at higher potentials due to changes in the surface of the electrode's catalyst layer.

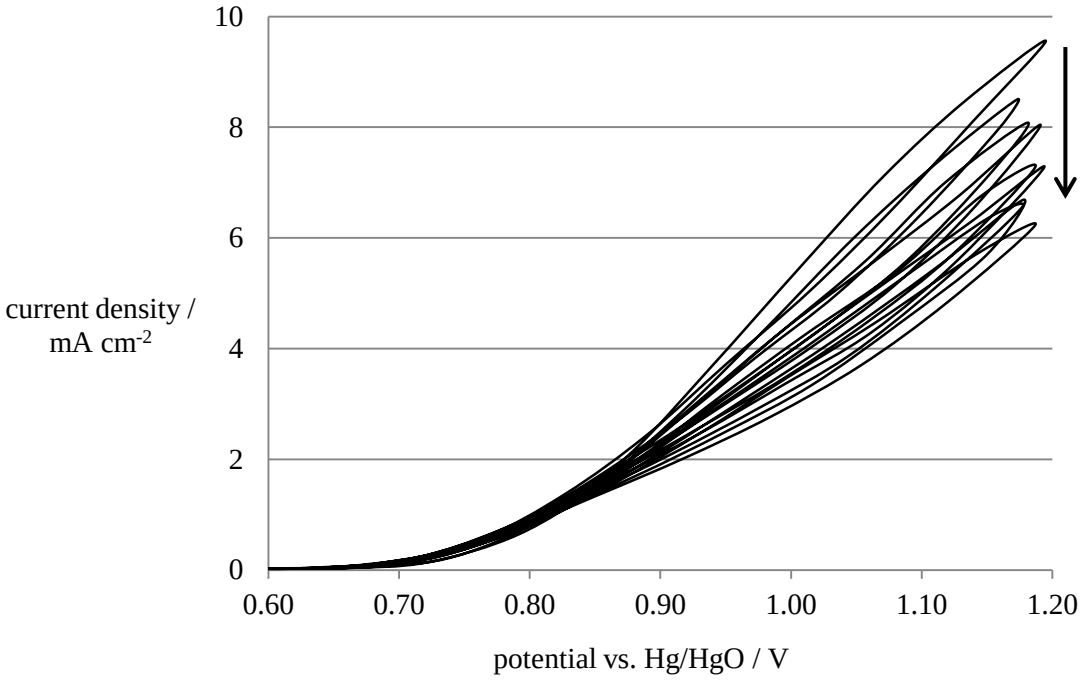

Figure 5-2 Cyclic voltammetry in the oxygen evolution region of pure titanium electrodes in an electrolyte of 1 M NaOH at a temperature of 25°C and a scan rate of 20 mV s^{-1}

The current density values at 1.2 V vs. Hg/HgO decrease almost linearly with each subsequent cycle, with large hysteresis between the anodic and cathodic sweeps at high potentials. This corresponds to a decrease in electrochemical activity that is almost certainly due to the build up of a layer of TiO_2 as discussed in 2.3.2.

Figure 5-3 is a steady state CV scan that shows the overall performance of a titanium electrode at 0.8 V vs. Hg/HgO is approximately 0.5 mA cm^{-2}. By comparison, values of 70 – 80 mA cm^{-2} were achieved with nickel electrodes in the same system (see Figure 2-1). The titanium electrode shows less than 1% of the current density value that a typical nickel electrode produces, and can therefore be seen as negligible back ground activity when used as an electrode material.

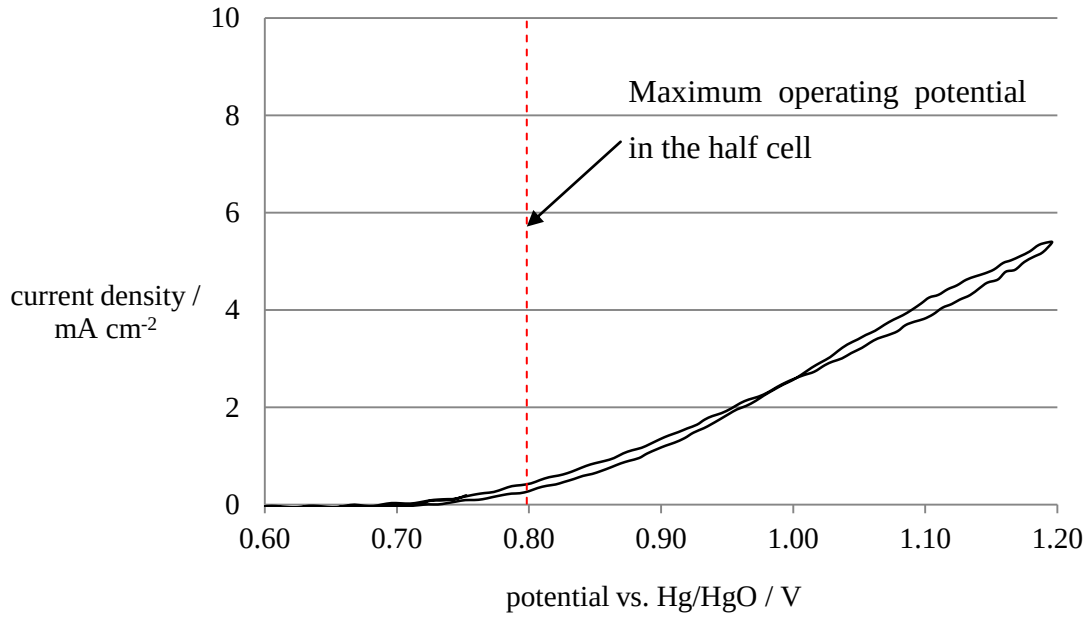

Figure 5-3 Cyclic voltammogram of oxygen evolution on a titanium base electrode in an electrolyte of 1 M NaOH at a temperature of 25°C and a scan rate of 0.5 mV s^{-1}

G. Oxygen evolution reaction on gold plated titanium electrodes with an IrO_2 catalyst film containing 25% PVDF

The linear regions of the Tafel plots from Figure 3-3 are shown below.

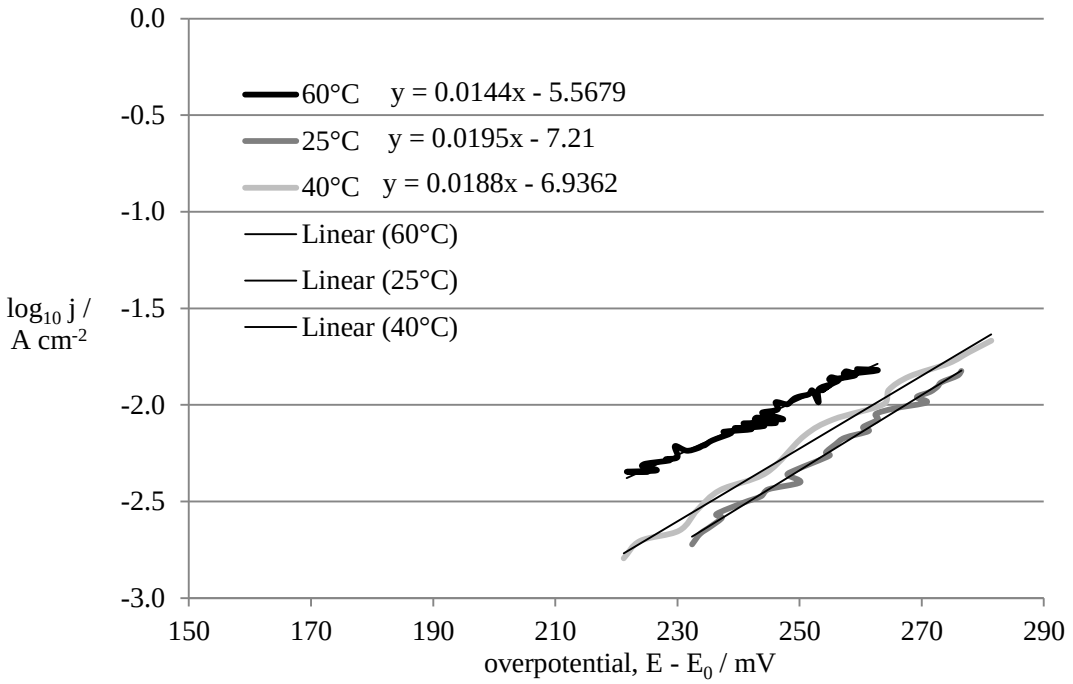

Figure 5-4 Tafel plots for IrO_2 electrodes in an electrolyte of 1 M NaOH at temperatures of 25, 40 and 60°C

The expression for a straight line takes is

$$y = mx + c$$

Or for the case of a Tafel plot

$$logj = b\eta + i_0$$

H. Calculating particle size with Scherrer formula

The particle sizes of catalysts analysed by XRD are calculated according to the Scherrer formula in Equation 5-4 [110].

$$D = \frac{K\,\lambda}{B\cos(\theta)} \qquad \textbf{Equation 5-4}$$

Where D is the average particle size;

B stands for full width at half maximum height (FWHM) of the peaks (radians);

K = 0.89 is used for integral breadth of spherical crystals with cubic symmetry;

λ is the source wavelength (1.514 angstroms);

θ is the Bragg angle (degrees).

Values for the peak angles, B and D are given to an accuracy of three significant figures.

Table 5-1 Particle sizes of particulates formed from the chemical bath deposition method

Peak angle 2θ degrees	B (FWHM) θ radians	D, particle size nm
11.6	1.65	58.2
23.1	2.44	42.7
33.9	1.13	94.3
36.5	5.38	20.0
60.3	2.71	43.5

Table 5-2 Particle sizes of NiO formed from thermal decomposition of particles formed from the chemical bath deposition method

Peak angle 2θ degrees	B (FWHM) θ radians	D, particle size nm
37.0	4.18	25.7
43.2	3.63	30.2
62.8	3.52	33.9

Table 5-3 Particle sizes of $NiCo_2O_4$ heat treated at 280°C for one hour

Peak angle 2θ degrees	FWHM θ radians	Particle size (nm)
31.2	0.919	115
36.8	0.660	163
44.7	1.13	97.4
59.1	1.03	114
64.9	1.20	101

Table 5-4 Particle sizes of $NiCo_2O_4$ heat treated at 300°C for one hour

Peak angle 2θ degrees	FWHM	Particle size (nm)
31.2	0.922	115
36.8	0.569	189
44.7	0.884	125
59.1	1.08	108
64.9	1.09	111

I. Establishing catalyst loadings on catalyst coated membranes

The mass of the catalyst film deposited was established through the difference in mass of the electrode with measurements made before and after the deposition of the catalyst film. Due to the intrinsic properties of anion exchange membranes, when they are exposed to the atmosphere they absorb moisture and their mass increases at a rate that depends on their current moisture content. The first measurement takes place after the membrane has been dehydrated in an oven at 50°C and then placed on a microbalance. The time taken for the mass to increase by 1 mg is recorded. It is assumed the rate of uptake of moisture is directly proportional to the mass of the membrane according to Equation 5-5:

$$\frac{\vartheta mg}{\vartheta t} \qquad \textbf{Equation 5-5}$$

The mass used in the calculation of the catalyst loading is taken when the rates of change of the mass of the membrane, before and after deposition, are equal.

$$catalyst\ loading = \frac{\Delta mg}{geometrical\ surface\ area\ of\ catalyst\ film}$$

$$\Delta mg = \frac{mass\ after\ deposition}{mass\ before\ deposition}$$

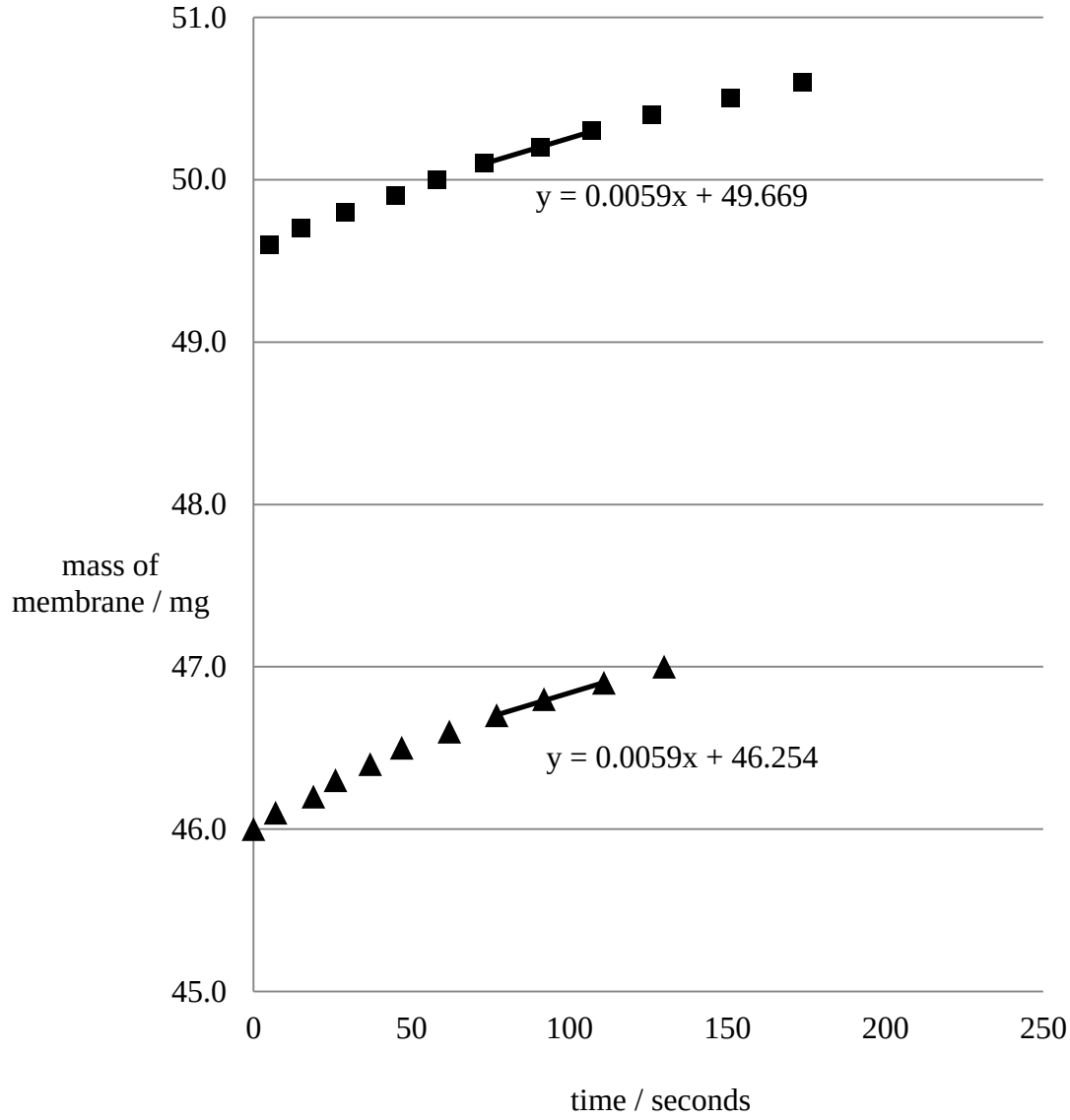

Figure 5-5 Change in mass of an anion exchange membrane before and after airbrushing a catalyst film

The curve shows the rate of uptake of moisture in the membrane decreases slowly with time. The linear relationship of three data points in series gives the equation of a straight line, and the rate can be determined from matching the gradients.

J. Steady state response

The steady state current response of scans performed between 1 and 2 V with a scan rate of 0.5 mV s^{-1} at temperatures of 25, 40 and 60°C

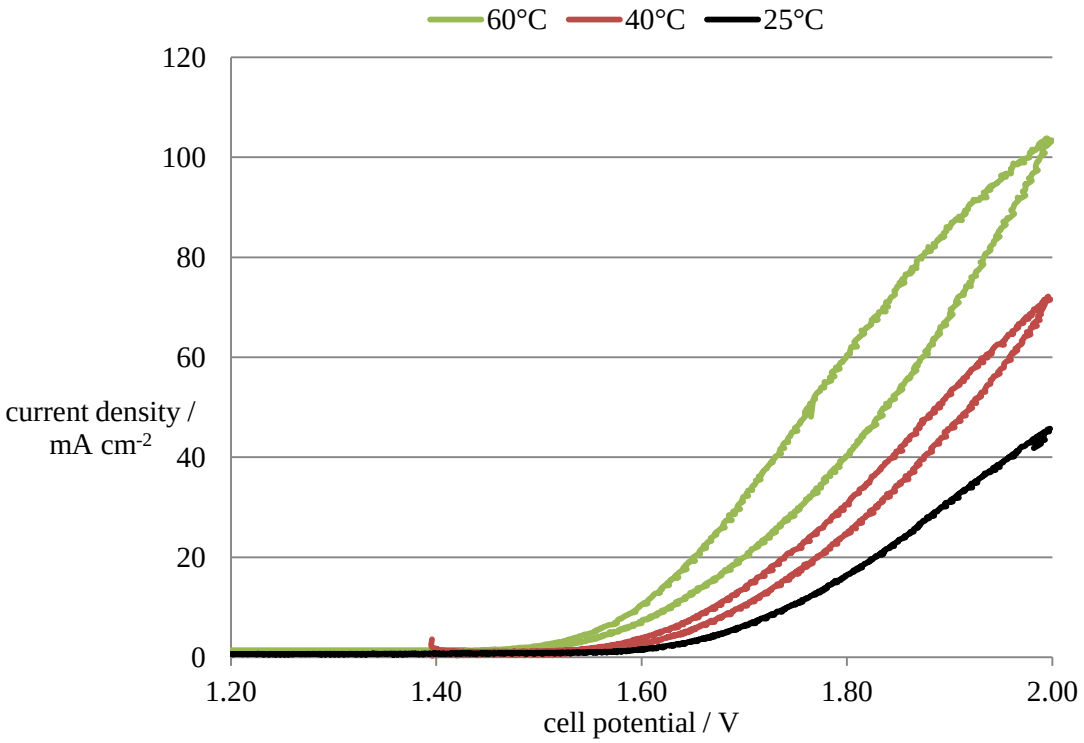

Figure 5-6 Temperature effects on the steady state polarisation curves of $NiCo_2O_4$ in DI water

References

1. World Energy Outlook 2012: In-depth study on energy-efficiency. 2012, International Energy Agency.

2. Department of Energy & Climate Change: UK Energy In Brief 2012. 2012.

3. Administration, E.I. International Energy Outlook 2011. 2011 [cited 2013 April 2013]; Available from: http://www.eia.gov/analysis/projection-data.cfm.

4. OPEC, OPEC Annual Statistical Bulletin 2012. 2012.

5. IPCC Fourth Assessment Report: Climate Change 2007. 2007.

6. Renewable Energy Technology Roadmap: 20% by 2020. 2007, European Renewable Energy Council: Brussels.

7. Li, H., et al., Solar constant values for estimating solar radiation. Energy, 2011. **36**(3): p. 1785-1789.

8. Fischer, M., M. Werber, and P.V. Schwartz, Batteries: Higher energy density than gasoline? Energy Policy, 2009. **37**(7): p. 2639-2641.

9. Appleby, A.J. and F.R. Foulkes, Fuel Cell Handbook. 1993, Malabar, Florida: Krieger Publishing Company.

10. UK H2Mobility: potential for hydrogen fuel cell electric vehicles - phase 1 results. 2013.

11. Deutsche Energie Agentur. 2013 [cited 2013; Available from: http://www.dena.de/en/.

12. Power, I. Participation in French Hydrogen Infrastructure Programme. 2013 [cited 2013; Available from: http://www.itm-power.com/news-item/participation-in-french-hydrogen-infrastructure-programme/.

13. DIRECTIVE OF THE EUROPEAN PARLIAMENT AND OF THE COUNCIL, E. Commission, Editor. 2012, European Commission: Brussels.

14. U.S. Department of Energy Hydrogen and Fuel Cells Program. 2013 [cited 2013; Available from: http://www.hydrogen.energy.gov/.

15. Energy Department Launches Public-Private Partnership to Deploy Hydrogen Infrastructure. 2013 [cited 2013 May]; Available from: http://energy.gov/articles/energy-department-launches-public-private-partnership-deploy-hydrogen-infrastructure.

16. Hydrogen Office Project. 2013 [cited 2013; Available from: http://www.hydrogenoffice.com/index.asp.

17. Savadogo, O., New materials for water electrolysis and photoelectrolysis. Hydrogen Energy Progress Xi, Vols 1-3, 1996: p. 2065-2092.

18. Carlin, N.T., et al., Co-combustion and Gasification of Coal and Cattle Biomass: a Review of Research and Experimentation, in Green Energy: Basic Concepts and Fundamentals, X.G. Li, Editor. 2011, Springer-Verlag London Ltd: Godalming. p. 123-179.

19. Melis, A., Bioengineering of Green Algae to Enhance Photosynthesis and Hydrogen Production. Artificial Photosynthesis: From Basic Biology to Industrial Application, ed. A.F. Collings and C. Critchley. 2005, Oxford: Blackwell Science Publ. 229-240.

20. Murata, K., et al., Hydrogen production from steam reforming of hydrocarbons over alkaline-earth metal-modified Fe- or Ni-based catalysts. Energy & Fuels, 2004. **18**(1): p. 122-126.

21. Trasatti, S., Water electrolysis: who first? Journal of Electroanalytical Chemistry, 1999. **476**(1): p. 90-91.

22. Newborough, M., A report on electrolysers, future markets and the prospects for ITM Power Ltd's electrolyser technology. 2004.

23. Ma, Y., Ceria-based Nanocomposite Electrolyte for Low-Temperature Solid Oxide Fuel cells, in Division of Functional Materials, School of Information and Communication Technology, Royal Institute of Technology. 2009.

24. ITM Power Prospectus. 2012 [cited April 2013; Available from: http://www.itm-power.com/wp-content/uploads/2012/04/ITM-AdmissionDocument.pdf.

25. Lamanauw, D., Hydrogen Bubble Characterization in Alkaline Water Electrolysis, in Graduate Department of Metallurgy and Materials Science. 2000, University of Toronto: Toronto.

26. Bard, A.J. and L.R. Faulkner, Electrochemical Methods: Fundamentals and Applications. 2 ed. 2001: Wiley. 833.

27. Bard, A.J., G. Inzelt, and F. Scholz, Overpotential, in Electrochemical Dictionary. 2008, Springer. p. 536.

28. Ulleberg, O., Modeling of advanced alkaline electrolyzers: a system simulation approach. International Journal of Hydrogen Energy, 2003. **28**(1): p. 21-33.

29. Roy, A., S. Watson, and D. Infield, Comparison of electrical energy efficiency of atmospheric and high-pressure electrolysers. International Journal of Hydrogen Energy, 2006. **31**(14): p. 1964-1979.

30. LeRoy, R.L., C.T. Bowen, and D.J. LeRoy, The Thermodynamics of Aqueous Water Electrolysis. Journal of the Electrochemical Society, 1980. **127**(9): p. 1954-1962.

31. Pletcher, D. and X. Li, Prospects for alkaline zero gap water electrolysers for hydrogen production. International Journal of Hydrogen Energy, 2011. **36**(23): p. 15089-15104.

32. Varcoe, J.R. and R.C.T. Slade, An electron-beam-grafted ETFE alkaline anion-exchange membrane in metal-cation-free solid-state alkaline fuel cells. Electrochemistry Communications, 2006. **8**(5): p. 839-843.

33. Chempath, S., et al., Density Functional Theory Study of Degradation of Tetraalkylammonium Hydroxides. The Journal of Physical Chemistry C, 2010. **114**(27): p. 11977-11983.

34. Dihrab, S.S., et al., Review of the membrane and bipolar plates materials for conventional and unitized regenerative fuel cells. Renewable and Sustainable Energy Reviews, 2009. **13**(6-7): p. 1663-1668.

35. Trasatti, S., Physical electrochemistry of ceramic oxides. Electrochimica Acta, 1991. **36**(2): p. 225-241.

36. InfoMine Mining Intelligence & Technology. 2012 [cited 2012; Available from: http://www.infomine.com/.

37. Kinoshita, K., Electrochemical Oxygen Technology. 1st ed. The Electrochemical Society series, ed. K. Kinoshita. 1992, New York: Wiley.

38. Loučka, T., The reason for the loss of activity of titanium anodes coated with a layer of RuO2 and TiO2. Journal of Applied Electrochemistry, 1977. **7**(3): p. 211-214.

39. Xu, J., et al., The physical-chemical properties and electrocatalytic performance of iridium oxide in oxygen evolution. Electrochimica Acta, 2011. **56**(27): p. 10223-10230.

40. Leng, Y., et al., Solid-State Water Electrolysis with an Alkaline Membrane. Journal of the American Chemical Society, 2012. **134**(22): p. 9054-9057.

41. Seghiouer, A., et al., Electrochemical oxidation of nickel in alkaline solutions: a voltammetric study and modelling. Journal of Electroanalytical Chemistry, 1998. **442**(1-2): p. 113-123.

42. H. Bode, K.D., J. Witte, Zur kenntnis der nickelhydroxidelektrode - I. Über das nickel (II)-hydroxidhydrat. Electrochimica Acta, 1966. **11**(8): p. 1079-1087.

43. Lyons, M.E.G., et al., Redox Switching and Oxygen Evolution at Hydrous Oxyhydroxide Modified Nickel Electrodes in Aqueous Alkaline Solution: Effect of Hydrous Oxide Thickness and Base Concentration. International Journal of Electrochemical Science, 2012. **7**(4): p. 2710-2763.

44. Pramanik, P. and S. Bhattacharya, A chemical method for the deposition of nickel-oxide thin-films. Journal of the Electrochemical Society, 1990. **137**(12): p. 3869-3870.

45. Hamdani, M., R.N. Singh, and P. Chartier, Co(3)O(4) and Co- Based Spinel Oxides Bifunctional Oxygen Electrodes. International Journal of Electrochemical Science, 2010. **5**(4): p. 556-577.

46. Tseung, A.C.C. and S. Jasem, Oxygen evolution on semiconducting oxides. Electrochimica Acta, 1977. **22**(1): p. 31-34.

47. Li, X.H., F.C. Walsh, and D. Pletcher, Nickel based electrocatalysts for oxygen evolution in high current density, alkaline water electrolysers. Physical Chemistry Chemical Physics, 2011. **13**(3): p. 1162-1167.

48. Wu, X. and K. Scott, CuxCo3-xO4 (0 <= x <= 1) nanoparticles for oxygen evolution in high performance alkaline exchange membrane water electrolysers. Journal of Materials Chemistry, 2011. **21**(33): p. 12344-12351.

49. Walsh, F., A First Course in Electrochemical Engineering. 1993, Romsey: The Electrochemical Consultancy.

50. Panek, J. and A. Budniok, Ni + Mo composite coatings for hydrogen evolution reaction. Surface and Interface Analysis, 2008. **40**(3-4): p. 237-241.

51. Tasic, G.S., et al., Characterization of the Ni-Mo catalyst formed in situ during hydrogen generation from alkaline water electrolysis. International Journal of Hydrogen Energy, 2011. **36**(18): p. 11588-11595.

52. Wu, Y., et al., Effect of synthesis method on the physical and catalytic property of nanosized NiO. Materials Letters, 2007. **61**(13): p. 2679-2682.

53. Chen, I., S.Y. Lin, and D.W. Shiue, Calcination of nickel alumina catalysts. Industrial & Engineering Chemistry Research, 1988. **27**(6): p. 926-929.

54. Straszko, J., J. Mozejko, and M. Olszakhumienik, Kinetics of thermal-decomposition of nickel sulfate hexahydrate. Journal of Thermal Analysis, 1995. **45**(5): p. 1109-1116.

55. Brockner, W., C. Ehrhardt, and M. Gjikaj, Thermal decomposition of nickel nitrate hexahydrate, Ni(NO3)2·6H2O, in comparison to Co(NO3)2·6H2O and Ca(NO3)2·4H2O. Thermochimica Acta, 2007. **456**(1): p. 64-68.

56. Elmasry, M.A.A., A. Gaber, and E.M.H. Khater, Thermal decomposition of Ni(II) and Fe(III) nitrates and their mixture. Journal of Thermal Analysis and Calorimetry, 1998. **52**(2): p. 489-495.

57. Jankovic, B., S. Mentus, and D. Jelic, A kinetic study of non-isothermal decomposition process of anhydrous nickel nitrate under air atmosphere. Physica B: Condensed Matter, 2009. **404**(16): p. 2263-2269.

58. Criado, J.M., A. Ortega, and C. Real, Mechanism of the thermal decomposition of anhydrous nickel nitrate. Reactivity of Solids, 1987. **4**(1-2): p. 93-103.

59. Pejova, B., et al., A solution growth route to nanocrystalline nickel oxide thin films. Applied Surface Science, 2000. **165**(4): p. 271-278.

60. Huang, X.H., et al., Nickel Foam-Supported Porous NiO/Ag Film Electrode for Lithium-Ion Batteries. Journal of the Electrochemical Society, 2008. **155**(6): p. A438-A441.

61. Huang, X.H., et al., Nickel foam-supported porous NiO/polyaniline film as anode for lithium ion batteries. Electrochemistry Communications, 2008. **10**(9): p. 1288-1290.

62. Xia, X.-h., et al., Hierarchically porous NiO film grown by chemical bath deposition via a colloidal crystal template as an electrochemical pseudocapacitor material. Journal of Materials Chemistry, 2010. **21**(3): p. 671-679.

63. Xia, X.H., et al., Morphology effect on the electrochromic and electrochemical performances of NiO thin films. Electrochimica Acta, 2008. **53**(18): p. 5721-5724.

64. Han, S.Y., et al., The growth mechanism of nickel oxide thin films by room-temperature chemical bath deposition. Journal of the Electrochemical Society, 2006. **153**(6): p. C382-C386.

65. Pawar, S.M., et al., Recent status of chemical bath deposited metal chalcogenide and metal oxide thin films. Current Applied Physics, 2011. **11**(2): p. 117-161.

66. Patil, U.M., et al., Characterization of honeycomb-like "β-Ni(OH)2" thin films synthesized by chemical bath deposition method and their supercapacitor application. Journal of Power Sources, 2009. **188**(1): p. 338-342.

67. M. Elimelech, J.G., X. Jia, and R. A. Williams, Particle Deposition & Aggregation. 1995: Butterworth-Heinemann.

68. Hu, C.C., Y.S. Lee, and T.C. Wen, The physicochemical/electrochemical properties of binary Ni-Co oxides. Materials Chemistry and Physics, 1997. **48**(3): p. 246-254.

69. Wu, G., et al., Anodically electrodeposited Co plus Ni mixed oxide electrode: preparation and electrocatalytic activity for oxygen evolution in alkaline media. Journal of Solid State Chemistry, 2004. **177**(10): p. 3682-3692.

70. Dechialvo, M.R.G. and A.C. Chialvo, Oxygen evolution reaction on NixCo(3-x)O4 electrodes with spinel structure. Electrochimica Acta, 1993. **38**(15): p. 2247-2252.

71. Haenen, J.G.D., W. Visscher, and E. Barendrecht, Oxygen Evolution on NiCo2O4 Electrodes. Journal of Applied Electrochemistry, 1985. **15**(1): p. 29-38.

72. Klissurski, D. and E. Uzunova, Synthesis and features of binary cobaltite spinels. Journal of Materials Science, 1994. **29**(2): p. 285-293.

73. Kaddouri, A., E. Tempesti, and C. Mazzocchia, Comparative study of beta-nickel molybdate phase obtained by conventional precipitation and the sol-gel method. Materials Research Bulletin, 2004. **39**(4-5): p. 695-706.

74. Mazzocchia, C., et al., On the NiO, MoO3 mixed-oxide correlation between preparative procedures thermal-activation and catalytic properties. Solid State Ionics, 1993. **63-5**: p. 731-735.

75. Varcoe, J.R., R.C.T. Slade, and E. Lam How Yee, An alkaline polymer electrochemical interface: a breakthrough in application of AAEMs in FCs. Chemical Communications, 2006(13): p. 1428-1429.

76. Bard, A.J., G. Inzelt, and F. Scholz, Electrochemical Dictionary. 2010, Springer. p. 194.

77. Dang, X.J., A.M. Massari, and J.T. Hupp, Electrochemically modulated diffraction - A novel strategy for the determination of conduction-band-edge energies for nanocrystalline thin-film semiconductor electrodes. Electrochemical and Solid State Letters, 2000. **3**(12): p. 555-558.

78. Roth, C., et al., Characterization of Differently Synthesized Pt-Ru Fuel Cell Catalysts by Cyclic Voltammetry, FTIR Spectroscopy, and in Single Cells. Journal of the Electrochemical Society, 2002. **149**(11): p. E433-E439.

79. Zhang, X.-W., et al., Composite doped emeraldine polyethylene oxide-bonded lithium-ion nano-tin anodes with electronic ionic mixed conduction. Solid State Ionics, 2002. **150**(3-4): p. 383-389.

80. Trasatti, S., Electrocatalysis in the anodic evolution of oxygen and chlorine. Electrochimica Acta, 1984. **29**(11): p. 1503-1512.

81. Yeo, R.S., et al., Perfluorosulfonic acid (nafion) membrane as a separator for an advanced alkaline water electrolyzer. Journal of Applied Electrochemistry, 1980. **10**(6): p. 741-747.

82. Ponomarev, A., Y. Moskvin, and S. Babenko, Transport properties of separating membranes MF-4SK during alkaline electrolysis of water. Russian Journal of Electrochemistry, 2007. **43**(3): p. 273-278.

83. Sanghi, I. and S. Visvanathan, Electrochemical behaviour of titanium in alkaline solutions. Electrochimica Acta, 1962. **7**(5): p. 567-575.

84. Boggio, R., A. Carugati, and S. Trasatti, Electrochemical surface-properties of Co3O4 electrodes. Journal of Applied Electrochemistry, 1987. **17**(4): p. 828-840.

85. Ives, D.J.G. and G.J. Janz, Reference electrodes, theory and practice. 1961, New York: Academic Press

86. Johnstone, H., A membrane's role in fuel cells. Filtration & Separation, 2001. **38**(4): p. 22-24.

87. Bukovec, P., et al., Thermal analysis of nickel oxide films. Journal of Thermal Analysis and Calorimetry, 1993. **40**(3): p. 1193-1196.

88. Wang, Q., et al., Morphology evolution of urchin-like NiCo2O4 nanostructures and their applications as psuedocapacitors and photoelectrochemical cells. Journal of Materials Chemistry, 2012. **22**: p. 21647-21653.

89. Freudenberg. Freudenberg Fuel Cell Components Manufacturer - H2315 C2 carbon paper. [cited 2013; Available from: http://fuelcellsetc.com/store/F2GDL.

90. Varcoe, J.R., et al., Membrane and Electrode Materials for Alkaline Membrane Fuel Cells, in Proton Exchange Membrane Fuel Cells 8, Pts 1 and 2, T. Fuller, et al., Editors. 2008. p. 1819-1834.

91. Mamlouk, M., et al., Electrochemical and fuel cell evaluation of Co based catalyst for oxygen reduction in anion exchange polymer membrane fuel cells. Journal of Power Sources, 2011. **196**(18): p. 7594-7600.

92. Komkova, E.N., et al., Anion-exchange membranes containing diamines: preparation and stability in alkaline solution. Journal of Membrane Science, 2004. **244**(1-2): p. 25-34.

93. Varcoe, J.R., et al., Poly(ethylene-co-tetrafluoroethylene)-derived radiation-grafted anion-exchange membrane with properties specifically tailored for application in metal-cation-free alkaline polymer electrolyte fuel cells. Chemistry of Materials, 2007. **19**(10): p. 2686-2693.

94. Lyons, M.E.G. and S. Floquet, Mechanism of oxygen reactions at porous oxide electrodes. Part 2-Oxygen evolution at RuO2, IrO2 and IrxRu1-xO2 electrodes in aqueous acid and alkaline solution. Physical Chemistry Chemical Physics, 2011. **13**(12): p. 5314-5335.

95. Rasten, E., G. Hagen, and R. Tunold, Electrocatalysis in water electrolysis with solid polymer electrolyte. Electrochimica Acta, 2003. **48**(25-26): p. 3945-3952.

96. Guerrini, E., H. Chen, and S. Trasatti, Oxygen evolution on aged IrO2x /Ti electrodes in alkaline solutions. Journal of Solid State Electrochemistry, 2007. **11**(7): p. 939-945.

97. Xia, X.H., et al., Electrochromic properties of porous NiO thin films prepared by a chemical bath deposition. Solar Energy Materials and Solar Cells, 2008. **92**(6): p. 628-633.

98. Hodes, G., Chemical Solution Deposition of Semiconductor Films. 2002: CRC Press.

99. Huang, X.H., et al., Morphology effect on the electrochemical performance of NiO films as anodes for lithium ion batteries. Journal of Power Sources, 2009. **188**(2): p. 588-591.

100. Cai, G.-f., et al., An efficient route to a porous NiO/reduced graphene oxide hybrid film with highly improved electrochromic properties. Nanoscale, 2012. **4**(18): p. 5724-5730.

101. Snook, G.A., N.W. Duffy, and A.G. Pandolfo, Evaluation of the effects of oxygen evolution on the capacity and cycle life of nickel hydroxide electrode materials. Journal of Power Sources, 2007. **168**(2): p. 513-521.

102. Guerrini, E., et al., Effect of FeOx on the electrocatalytic properties of NiCo2O4 for O-2 evolution from alkaline solutions. Journal of Solid State Electrochemistry, 2008. **12**(4): p. 363-373.

103. Haenen, J., W. Visscher, and E. Barendrecht, Characterization of NiCo2O4 electrodes for O2 evolution: Part I. Electrochemical characterization of freshly prepared NiCo2O4 electrodes. Journal of Electroanalytical Chemistry and Interfacial Electrochemistry, 1986. **208**(2): p. 273-296.

104. Song, R., H.J. Wang, and S.H. Feng, Solvothermal Preparation of Mn3O4 Nanoparticles and Effect of Temperature on Particle Size. Chemical Research in Chinese Universities, 2012. **28**(4): p. 577-580.

105. Shirsath, S.E., et al., Effect of sintering temperature and the particle size on the structural and magnetic properties of nanocrystalline Li0.5Fe2.5O4. Journal of Magnetism and Magnetic Materials, 2011. **323**(23): p. 3104-3108.

106. Seetawan, U., et al., Effect of annealing temperature on the crystallography, particle size and thermopower of bulk ZnO. Solid State Sciences, 2011. **13**(8): p. 1599-1603.

107. Wieckowski, A., Interfacial electrochemistry - Theory, experiment, and applications, in Interfacial Electrochemistry, A. Wieckowski, Editor. 1999. p. 769-792.

108. Serebrennikova, I. and V.I. Birss, Mass changes accompanying the electrochemical reaction of sol-gel formed 50 : 50 Ni-Co oxide films. Journal of Electroanalytical Chemistry, 2000. **493**(1-2): p. 108-116.

109. Jia, J., X. Li, and G. Chen, Stable spinel type cobalt and copper oxide electrodes for O2 and H2 evolutions in alkaline solution. Electrochimica Acta, 2010. **55**(27): p. 8197-8206.

110. Li, G.-J., et al., Preparation and characteristics of nanocrystalline NiO by organic solvent method. Materials Letters, 2001. **51**(4): p. 325-330.